

ABSTRACT

Buescher, Nathan. Live-Axis Turning. (Under the direction of Thomas A. Dow)

The goal of this research is to develop a new method to create Non-Rotationally Symmetric (NRS) optical surfaces that overcomes the limitations of the current techniques and is fast, accurate and inexpensive. The term Live-Axis turning (LAT) has been coined to describe a lightweight, linear-motor driven, air bearing slide that can be used to fabricate NRS surfaces. The system described was developed at the Precision Engineering Center (PEC) in an effort to create a long-range fast tool servo to fabricate future NASA optics. The slide designed for the system is a triangular cross-section, lightweight (0.6 kg) honeycomb aluminum slide driven by a linear motor (64 N maximum force) resulting in an acceleration capability of 10 g. Additionally, a damper was added to the system to investigate the effects of physical damping on surface quality. The LAT axis was mounted on a Nanoform 600 diamond turning machine and both flat surfaces and tilted flat surfaces were machined to assess the performance of the system, which has a rise time of less than 2 msec. The 12.5 mm diameter flat surfaces had surface finishes of 16 nm without damping and 14 nm with damping, with both having a figure error of less than $\frac{1}{2}$ wave. 25 mm diameter tilted flat surfaces, using a maximum stroke of +/- 1 mm at 5 Hz, had a surface finish of 24 nm without damping and 20 nm with damping. The figure error for the damped and undamped parts was +/- 25 microns.

LIVE-AXIS TURNING

NATHAN P. BUESCHER

A thesis submitted to the Graduate Faculty of
North Carolina State University
In partial fulfillment of the
Requirements for the Degree of
Master of Science

**MECHANICAL ENGINEERING
NORTH CAROLINA STATE UNIVERSITY**

Raleigh, NC
2005

APPROVED BY:

Dr. Ronald O. Scattergood

Dr. Jeffrey W. Eischen

Dr. Thomas A. Dow

Advisory Committee Chair

BIOGRAPHY

Nathan Paul Buescher was born on April 24, 1981 in Raleigh, North Carolina. He graduated from Broughton High School in 1999. He attended NC State University in Raleigh, NC and participated in the University Scholars Program and the engineering organization Tau Beta Pi. Additionally, he was a member of Kappa Alpha fraternity and was active in numerous intramural sports. While at NC State, Nathan worked as an intern at Joel Wittkamp Design and Stantec Consulting. Following his graduation with a Bachelor of Science in Mechanical Engineering and Mathematics Minor, Nathan pursued his Masters degree at NC State in the Fall of 2003, working as a research assistant at the Precision Engineering Center. Upon completion of this degree in the Fall of 2005, Nathan will work for Cummins, Inc. in Whitakers, NC.

ACKNOWLEDGMENTS

I would to thank everyone who helped, supported and guided me during my stay at NC State University. My time at the Precision Engineering Center gave me invaluable hands-on experience in so many areas and helped bridge the gap between the academic world and the real world for me. To the following people I am especially thankful.

- Dr. Thomas Dow, my advisor, for continually challenging me, teaching me how to think critically to solve problems and always asking more questions than I could answer.
- Alex Sohn, for being patient and putting in a lot of time with me on this project. Your practical nature and machining experience really taught me a lot.
- Ken Garrard, for much assistance with all computer-related issues and plenty of other concepts I was struggling to grasp, especially on the UMAC controller.
- Dr. Jeffrey Eischen and Dr. Ronald Scattergood, my committee members.
- Brett and Kara, for struggling through many classes and countless long nights at the PEC with me.
- All the other students at the PEC – Karl, Wittoon, Simon, Dave, Tim, Yanbo, Nadim, Lucas and Rob – for your help and for providing some good laughs.
- Laura Masters, for holding the place together during her time there.
- Stacey, for your love, support and especially patience during a seemingly endless journey.
- My brother William, for always providing laughter and good conversation.
- Especially my parents, Paul and Barbara Buescher, for always encouraging me to learn and grow and for providing me the means to do so.

TABLE OF CONTENTS

LIST OF FIGURES	VI
LIST OF TABLES	XI
1 INTRODUCTION.....	1
1.1 BACKGROUND	1
1.2 PROBLEM STATEMENT	7
2 SYSTEM DESIGN.....	8
2.1 SLIDE MATERIAL SELECTION.....	9
2.2 HONEYCOMB MODELING TECHNIQUE	11
2.2.1 Honeycomb Material Properties.....	12
2.2.2 Material Testing.....	17
2.2.3 Comparison of Model and Experiments.....	22
2.3 SLIDE CROSS-SECTION	26
2.3.1 Box Design.....	27
2.3.2 V-Shape Design.....	27
2.3.3 Triangle Design	28
2.3.4 Shape Comparison.....	29
2.4 SLIDE LENGTH.....	32
2.5 EXPERIMENTAL VERIFICATION OF SLIDE DESIGN.....	37
2.5.1 Bending Test.....	37
2.5.2 Frequency Analysis.....	39
2.6 LINEAR MOTOR	43
2.6.1 Motor Selection.....	43
2.6.2 Motor Analysis.....	44
2.7 MOTOR MOUNT BRACKET.....	46
2.7.1 Bracket Design.....	46
2.7.2 Magnet Track Relief.....	49
2.8 AIR BEARING.....	51
2.9 ADDITIONAL DESIGN CONSIDERATIONS	53
2.9.1 Linear Encoder	53
2.9.2 Tool Holder.....	54
2.9.3 Vertical Tool Adjustment	55
2.10 DYNAMIC TESTING	57
2.11 DESIGN SUMMARY.....	58
3 LAT SYSTEM CHARACTERIZATION.....	60
3.1 DESCRIPTION OF EXPERIMENTAL APPARATUS.....	60
3.1.1 System Components.....	60
3.1.2 Amplifier Configuration.....	63
3.1.3 UMAC Configuration.....	63
3.1.4 Cooling Issues	64
3.2 SYSTEM CHARACTERIZATION.....	65

3.2.1	<i>Undamped System Model</i>	66
3.2.2	<i>Open Loop System Verification</i>	70
3.2.3	<i>Damped System Model</i>	71
3.2.5	<i>Damper Design and Verification</i>	75
4	CONTROLLER DESIGN AND IMPLEMENTATION	80
4.1	CONTROLLER COMPONENTS	80
4.2	ROLE OF DAMPING IN THE LAT SYSTEM	81
4.3	PID CONTROL SCHEME.....	83
4.4	CONTROLLER TUNING	85
4.4.1	<i>Simulink Model Tuning</i>	86
4.4.2	<i>LAT System Tuning</i>	89
5	MACHINING EXPERIMENTS	100
5.1	PMMA FLAT.....	101
5.2	TILTED FLAT PROCEDURE	105
5.2.1	<i>Tool Radius Compensation</i>	105
5.2.2	<i>Cutting Procedure</i>	108
5.3	PMMA TILTED FLAT	111
5.4	SYSTEM MODIFICATIONS.....	114
5.5	COPPER FLATS.....	115
5.5.1	<i>Undamped Copper Flat</i>	116
5.5.2	<i>Damped Copper Flat</i>	119
5.6	ALUMINUM TILTED FLATS	121
6	CONCLUSIONS AND FUTURE WORK	130
	REFERENCES	132
	APPENDIX	135
	APPENDIX A – HONEYCOMB DEFLECTION EQUATIONS	136
	APPENDIX B – BEARING STIFFNESS	141
	APPENDIX C – LINEAR MOTOR THEORY OF OPERATION	142
	APPENDIX D – AIREX P12 – 1 LINEAR MOTOR SPECIFICATIONS	146
	APPENDIX E – TRANSFORMED AREA METHOD FOR COMPOSITES	149
	APPENDIX F – MAGNET TRACK RELIEF ANALYSIS.....	154
	APPENDIX G – FLEXURE PLATE CALCULATIONS	156
	APPENDIX H – AMPLIFIER CONFIGURATION GUIDE.....	157
	APPENDIX I – MOTION PROGRAMS AND PMAC CODE	159
	APPENDIX J – THERMISTOR MANUFACTURER SPECS	167
	APPENDIX K – MOTOR TEMPERATURE CALCULATIONS.....	168
	APPENDIX L – DAMPING FORCE CALCULATIONS.....	169
	APPENDIX M – SIMULINK MODEL OF PMAC CONTROLLER.....	170
	APPENDIX N – TOOL RADIUS COMPENSATION	171

LIST OF FIGURES

Figure 1-1. Raster scan diamond fly-cutting.....	3
Figure 1-2. Diamond Turning Machine (DTM) with tool servo (Z') used to create NRS surfaces. The height of the surface is a function of the location on the face (x,y) or in polar coordinates, r and q.....	4
Figure 1-3. Decomposition of off-axis conic mirror surface (top) into symmetric (bottom left) and non-symmetric (bottom right) components for on-axis fabrication (different Z axis magnitudes should be noted).....	6
Figure 2-1. Front (left) and side views of general LAT design.....	8
Figure 2-2. (a) A composite aluminum beam. (b) A closer look at the cell structure of the honeycomb [12].	9
Figure 2-3. The orthotropic nature of the honeycomb core.....	13
Figure 2-4. Aluminum facing skin, seen at 50X by the Zeiss ICM 405 microscope – approximately 1 mm (0.04 in.) thick.	14
Figure 2-5. Ribbon and Transverse directions in the honeycomb cell structure.	15
Figure 2-6. Top view of honeycomb core at 200X on the Zeiss ICM 405 microscope. The bright section is two strips of aluminum joined at the faces, so the measured width (the thickness of one strip) is only one-half of the total width.	17
Figure 2-7. Instron testing machine.....	18
Figure 2-8. An aluminum specimen in a four-point bending test.....	19
Figure 2-9. Load vs. Displacement for aluminum honeycomb specimen.	20
Figure 2-10. The elastic region of the honeycomb Load vs. Displacement plot (labeled in Figure 2-9).	20
Figure 2-11. Setup for frequency test.	21
Figure 2-12. Frequency response of aluminum honeycomb sample free-free test. Resonance occurs at 2.48 KHz.	22
Figure 2-13. Simulated four-point bending test on a beam of aluminum honeycomb modeled as two thin sheets of aluminum bonded to a honeycomb core. The load shown is 200 lb., and it corresponds to a deflection of 0.0078 in.....	24
Figure 2-14. Load vs. Deflection plot for aluminum honeycomb of fixed geometry. Theoretical refers to the analytical solution, Experimental is from the Instron machine, and Model is the FEA results.	24
Figure 2-15. Free-free vibration of an aluminum honeycomb beam. This first free-body mode occurs at 2800 Hz.....	25
Figure 2-16. The underside of an aluminum facing skin (with some honeycomb attached). The uneven distribution of the glue may have yielded a slightly lower natural frequency than a perfectly bonded specimen.....	26
Figure 2-17. (Left) Simplified box design (darker, outer shell is aluminum; lighter parts are honeycomb). Cutout is needed so motor may be embedded. (Right) Box design shown with housing. The rectangle in the middle represents the slide shown on the left.	27
Figure 2-18. Simplified V-shape design (left) and V-shape slide with housing (right). .	28
Figure 2-19. Simplified view of the triangle design (left) and the housing for this design (right).	29
Figure 2-20. Static loading test simulation setup for the triangle slide	31

Figure 2-21. Vertical bending (left) and horizontal twisting modes of the slide-bracket-coil assembly.....	33
Figure 2-22. Rigid body modes of vibration due to the bearing.....	34
Figure 2-23. Graphical comparison of structural and bearing natural frequencies.....	35
Figure 2-24. Setup for the slide bending test. Force was applied at the vertex of the triangle, and the deflection was measured below.	37
Figure 2-25. Force vs. Deflection plot for the slide bending test. The elastic region is located inside the circle.....	38
Figure 2-26. First (left) and second (right) predicted modes of vibration for the triangle slide. The first mode (twisting) occurs at 3950 Hz and the second (bending) at 5110 Hz (results from COSMOS FEA analysis).....	39
Figure 2-27. Setup for the slide frequency analysis (left). An accelerometer is seen attached to the far right corner of the slide. The accelerometer amplifier is shown on the right.	40
Figure 2-28. Magnitude results from slide frequency test. When the slide was struck in the middle, a spike around 3550 Hz occurred (top plot). When struck at the corner, the dominant frequency was around 4660 Hz (bottom).....	41
Figure 2-29. Layout of the slide grid used in the frequency analysis.....	42
Figure 2-30. Embedded motor coil design (left) and rear-attached motor coil design....	44
Figure 2-31. Cutaway view of a linear motor I-coil. The banded strands of copper wire can be seen.	45
Figure 2-32. Experimental setup for the motor coil bending test.	46
Figure 2-33. Original design of motor mount bracket.	47
Figure 2-34. The first mode of vibration of the system using the original bracket showed significant deflection in the bracket.....	47
Figure 2-35. New bracket with thicker faceplate, horizontal gussets and lightweighting holes.....	48
Figure 2-36. First bending mode with new bracket. Deformation now occurs in the slide and motor coil, indicating a sufficiently stiff bracket.	48
Figure 2-37. 3D drawing of the new rear faceplate of the slide. This view is from inside the slide looking toward the back. A relief (the large box) is provided for the magnet track, and the four small squares are used to hold the bracket screws.....	50
Figure 2-38. Slide-bracket-motor assembly. The magnet track forms a channel around the bottom of the motor I-coil and extends into box-shaped relief area in the slide...	50
Figure 2-39. Final bracket design.	51
Figure 2-40. Photograph of LAT system. The slide and air bearing housing are shown.	51
Figure 2-41. Setup for air bearing stiffness measurements.....	53
Figure 2-42. Renishaw RGH24B linear encoder with scale.....	54
Figure 2-43. Tool holder mounted to the front of the triangular slide.....	55
Figure 2-44. Flexure plate layout on the Nanoform. The box with the knob directly under the slide housing is the micro height adjuster. The notched plate directly above the micro height adjuster is the flexure plate.	56
Figure 2-45. Model of the flexure plate in its natural (left) and deflected (right) positions.	56
Figure 2-46. Z-axis motion during LAT operation at +/- 2mm, 20 Hz.	58

Figure 2-47. Final design drawings for the LAT system. Front and side view shown...	59
Figure 3-1. Main component layout of the LAT system. The arrows show the direction of command.	61
Figure 3-2. Block diagram of the entire system. The signal from the PC is compared to the current tool position, then sent to the UMAC. It is acted on by the controller and sent to the amplifier, which commutates the system based on the position feedback.	62
Figure 3-3. Plot of motor temperature versus time.	65
Figure 3-4. Free-body diagram of the undamped LAT system	66
Figure 3-5. Open-loop block diagram of the undamped system.	67
Figure 3-6. Theoretical open-loop Bode plots of the undamped system.	68
Figure 3-7. Amplifier response to a closed-loop step command.	69
Figure 3-8. Experimental undamped transfer function compared with system model.	71
Figure 3-9. Free-body diagram of the damped system.	72
Figure 3-10. Root Locus plot for the undamped (a) and damped (b) systems. The addition of the damping force pushes the closed loop poles into the left-hand plane, indicating a stable system.	73
Figure 3-11. Step response of the damped and undamped system. While the damped system decays, the response of the undamped system maintains constant amplitude (marginally stable).	74
Figure 3-12. The damper for the LAT system. The rod shown slides through an O-ring sandwiched between the two brackets.	75
Figure 3-13. Diagram of rod (horizontal line) - O-ring (curved line) interface.	76
Figure 3-14. Viscous Damping Force vs. Edge Clearance.	77
Figure 3-15. Bode Plots for varying systems with varying damping forces. The "jagged" dotted line is the experimental data.	79
Figure 3-16. Open loop block diagram of the damped system.	79
Figure 4-1. Control layout for the LAT system.	81
Figure 4-2. Block diagram of UMAC PID control scheme.	84
Figure 4-3. Simulink model of the controller and motor system	85
Figure 4-4. 156 μm step response of the undamped Simulink model.	87
Figure 4-5. Response of the Simulink damped model ($b=10$) to a 156 μm step. The rise time is roughly half that for the undamped system.	88
Figure 4-6. The response of the Simulink models to a 156 mm disturbance input over one servo cycle (442 μsec). The jump seen in the damped system is smaller than that of the undamped system.	89
Figure 4-7. Step response of the undamped system.	90
Figure 4-8. Undamped system response to 1 mm, 5 Hz sine wave. The top plot shows the command and actual motion, and the bottom plot shows the error between the two.	92
Figure 4-9. Phase error sine fit (top) and undamped system sine following error with phase lag removed.	93
Figure 4-10. Step response of damped system.	95
Figure 4-11. Damped system response to 1 mm, 5 Hz sine wave. The top plot shows the command and actual motion. The bottom plot shows the error between the two.	96
Figure 4-12. Phase error sine fit (top) and damped system sine following error with phase lag removed.	96

Figure 4-13. Setup for the disturbance rejection test. A string with a weight attached was tied to the motor bracket and hung over the pulley. The weight was dropped, and the system's motion was recorded.....	98
Figure 4-14. Undamped (top) and damped (bottom) system response to external disturbance, with the modeled/theoretical responses shown as dotted lines. A smaller peak value for the damped system shows it is more resistant to external forces.....	99
Figure 5-1. LAT axis on the Nanoform 600.	100
Figure 5-2. Scanning White Light Interferometer (SWLI) image of the PMMA flat machined at 500 rpm with a 1 mm/min feedrate.	102
Figure 5-3. Error motion (left) of the LAT axis (commanded minus actual position) during machining at 500 rpm. The figure at right is the FFT of the error.	104
Figure 5-4. Tilted flat being measured by the coordinate measuring machine (CMM). The non-tilted part was flat to less than 1 μm – beyond the resolution of the machine.	104
Figure 5-5. Top view of DTM during generation of the tilted flat	105
Figure 5-6. Tool tip contact with a flat surface (top) and a tilted surface (bottom). Tool tip compensation is needed to eliminate the unwanted contact associated with a tilted surface.	106
Figure 5-7. The LAT position (top) and the associated tool radius compensation (bottom) for a 1 mm radius tool and a 2mm peak-to-peak flat at 25 mm radius. The compensation is always subtracted from the commanded position.	107
Figure 5-8. LAT axis error generated with the kinematics routine (position-based).....	109
Figure 5-9. LAT axis error generated by the time-based motion program. The 250 Hz. frequency is no longer present.	110
Figure 5-10. Surface of the 2 mm PMMA tilted flat machined at 500 rpm with a 2.5 mm/min feedrate. The radial direction is approximately along the grooves.	111
Figure 5-11. PMMA tilted flat cutting data. The top plot shows the error during cutting. The bottom plot shows the frequency content of the error.	113
Figure 5-12. The effect of the notch filter in the controller on the system performance.	115
Figure 5-13. 50 X 70 μm area of a flat machined without damping ($R_a = 16 \text{ nm}$). The spindle speed was 400 rpm and the federate was 0.84 mm/min.....	116
Figure 5-14. LAT motion during position holding. The top plot (a.) shows the motion reported by the LAT encoder. The bottom plot (b.) is Lion capacitance gauge data for the same experiment.	117
Figure 5-15. Cap gauge data collection setup.....	118
Figure 5-16. Zygo Laser Interferometry image of the surface of the flat cut without damping. The 12 mm surface is flat to less than $\frac{1}{2}$ wave. The part was cut with a spindle speed of 400 rpm and a federate of 0.84 mm/min.....	119
Figure 5-17. SWLI image of the flat cut with physical damping added to the system. The spindle speed was 400 rpm and the federate was 0.84 mm/min.....	120
Figure 5-18. Laser interferometry image of the flat cut with the damped LAT system. The spindle speed was 400 rpm and the federate was 0.84 mm/min.....	121
Figure 5-19. Surface of the undamped tilted flat. The part was cut at 300 rpm with a federate of 1.8 mm/min.....	122

Figure 5-20. FFT data of the LAT motion during cutting. A frequency of 150 Hz is noticed, as was seen in the controller tuning.	123
Figure 5-21. Surface of the undamped aluminum tilted flat measured by the CMM. The top left plot is an isometric view of the surface. The top right plot shows the surface figure error (best fit plane residual), and the bottom plot is a side view of the error.	124
Figure 5-22. Talysurf trace from the low edge to the high edge of the undamped aluminum tilted flat with the slope taken out. The “hump and valley” shape confirms the CMM data in Figure 5-20.	125
Figure 5-23. Theoretical tilted flat with linearly varying phase lag throughout the cut. Theoretical tilted flat surface (top left), error (top right) and side view of the error (bottom). The shape is the same as that seen in the undamped aluminum flat.	126
Figure 5-24. Surface of the tilted flat cut with damping added to the system. The spindle speed was 300 rpm and the feedrate was 1.8 mm/min.	127
Figure 5-25. (Top) Surface of the damped aluminum tilted flat as measured by the CMM. (Top right) Error in the tilted flat and side view of error (bottom). The error has the same shape as that for the undamped tilted flat and is due to varying phase lag.	128
Figure 5-26. Talysurf trace from the low edge to the high edge of the undamped aluminum tilted flat with the slope taken out.	129
Figure A-0-1. The make-up of a honeycomb composite. In this application, the facing skin material is aluminum.	136
Figure A-0-2. Honeycomb beam deflection due to bending.	137
Figure A-0-3. Honeycomb beam deflection due to shear.	137
Figure A-0-4. The rotor and stator of a basic rotary motor.	142
Figure A-0-5. Pole-switching sequence for rotary motor rotation.	143
Figure A-0-6. Three phase power. The plot shows Current vs. Time.	143
Figure A-0-7. Linear motor 3D view (top). Motor schematic, viewed from above (bottom).	144
Figure A-0-8. Reference dimension drawing for transformed area method.	150

LIST OF TABLES

Table 2-1. A comparison of weight and stiffness between two honeycomb beams and a solid I-beam.....	11
Table 2-2. List of values used to model honeycomb core.....	14
Table 2-3. Comparison between slide shapes.....	30
Table 2-4. Comparison of V-shape and triangle slide designs. The triangle design was chosen because of its high stiffness and relative ease of assembly, shown by the fewer number of parts.....	32
Table 2-5. Comparison of the translational and rotational natural frequencies due to the bearing stiffness and the vertical and horizontal natural frequencies of structural vibration.....	35
Table 2-6. Tool-tip moment stiffness for different slide lengths.....	36
Table 2-7. Comparison of predicted and actual results for a slide frequency analysis....	43
Table 2-8. Natural frequencies of the system for the two bracket designs.....	49
Table 3-1. Mass of LAT system's moving parts.....	67
Table 4-1. Final gains used for the undamped LAT system.....	94
Table 4-2. Final gains used for the damped LAT system.....	97
Table A-1. Summary of beam coefficients.....	138
Table A-2. Magnet track relied and bracket testing summary.....	155

1 Introduction

1.1 Background

The optical designer must address optical performance, space constraints, weight limitations, assembly/alignment issues and cost. The number and placement of optical elements depends on the application and the shape of each element. Based on experience and availability, the optical designer would typically choose spherical surfaces; however, aspheric (rotationally symmetric) elements are becoming common in many new designs. A more powerful alternative is to utilize anamorphic (non-rotationally symmetric) shapes such as off-axis conic or toroidal surfaces that can more efficiently collect and focus light while packaging the optical system into a smaller volume at lower cost. But the procurement of such optics is difficult, time consuming, and expensive. If the design consists of a series of spherical components, there is a large body of information available from a number of different manufacturers regarding fabrication capabilities. For Non-Rotationally Symmetric (NRS) surfaces however, fabrication capabilities are very limited. Hence, most designers tend to avoid anamorphic designs, even if such shapes could simplify the design, reduce the number of components and shorten the assembly time.

Grinding and Polishing A number of different fabrication processes are available to create NRS surfaces depending on the material and the application. The traditional method of making glass optics involves grinding and polishing the surface. This has been optimized for spherical surfaces using cup wheel grinding and polishing pads to rapidly generate tenth-wave surfaces. However, aspheric surfaces are more difficult to

generate and polish. New machines and methods have been developed over the past decade to speed this process and the technical challenges associated with these processes have been addressed [1, 2, 30]. These techniques utilize a small grinding wheel that follows the desired aspheric contour as it is moved along the radius of the rotating part. This same concept has been applied to create NRS parts except that the rotation speed of the part is reduced drastically such that the slide axis can move as a function of radius and angle to produce the desired NRS contour. To polish such a surface, techniques such as small aperture polishing have been used. The disadvantage of these polishing processes is they are exceedingly slow and the form error can deteriorate if several cycles of measure and polish are employed.

Fly-Cutting The use of diamond tools on precision lathes to create optical surfaces on lightweight and single-crystal materials has been a major innovation in optical fabrication. It has become the standard technique [3] to create reflective and refractive optics for military systems because both the optical surface as well as the reference surface used for assembly and alignment can be produced in one setup. First surface reflectors of lightweight aluminum alloys are possible using this technique. One method for fabricating NRS optics is fly-cutting with a multi-axis ultraprecision machine. Figure 1-1 shows the concept of the raster fly-cutting process. A large radius fly-cutter is passed over the surface of a part controlled by a multi-axis machine tool. The start and stop motion of the slides and the periodic features left on the surface require very slow scan speeds to achieve acceptable surface finish [4].

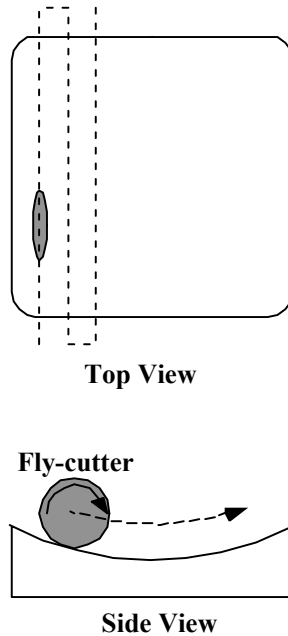


Figure 1-1. Raster scan diamond fly-cutting.

As a result, this process can require large amounts of time – sometimes days for a 100 mm square part. Long machining times will increase three things: the risk of anomalous events causing a defect, the drift in environmental conditions degrading the figure and finish, and the cost.

Diamond Turning with a Tool Servo A second approach is to program the tool to move as a function of both spindle and axis position to create the NRS shape. This can be done with a slow-slide servo or a fast tool servo (FTS). Shorter machining times are possible with diamond turning because the tool is always in contact with the part. An example of a machine with a tool servo is illustrated in Figure 1-2. The workpiece is attached to the spindle mounted on the X slide. The diamond tool is attached to the tool servo (Z') that sits on the Z slide.

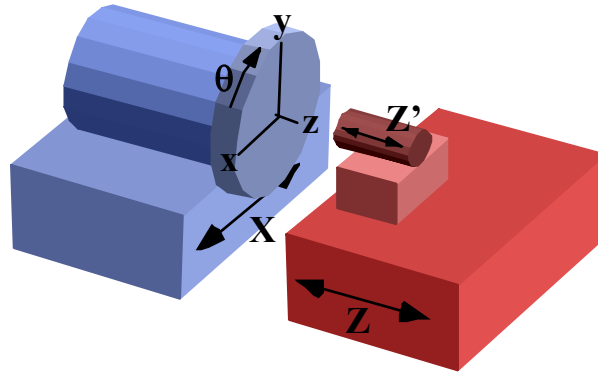


Figure 1-2. Diamond Turning Machine (DTM) with tool servo (Z') used to create NRS surfaces. The height of the surface is a function of the location on the face (x,y) or in polar coordinates, r and q .

The optical shape is specified as a z height for each r, θ location on the face. To create this shape, the tool needs to move in the Z direction (using the Z, Z' or both slides) as a function of the location of the X slide and the angular position of the spindle.

The method of creating the tool motion is what sets the various tool servos apart. The so-called “slow tool servo” uses the Z axis to move the tool and is limited to about 1 Hz for a stroke less than 10 mm [5]. The “fast tool servo” is typically piezoelectrically driven and has a stroke of 10-400 μm with a bandwidth of 200 Hz to 10 KHz. The Precision Engineering Center (PEC) at NC State University has much experience with fast tool servos [6]. Falter designed a piezoelectrically driven fast tool servo capable of 20 μm at 2 KHz (although the usable bandwidth was smaller) [7]. Based on similar concepts, Jared made a piezoelectric FTS capable of 10 μm displacement with a usable bandwidth of 200 Hz [8]. At MIT, Trumper et al created a rotary motor driven fast tool servo capable of a

50 μm stroke at 2 KHz [9], and an electromagnetically driven FTS capable of 30 μm at 2.3 KHz [10].

Live-Axis Turning This research presents a “Live-Axis” stage; a long-range, high-speed system that falls into the mid-range of the systems described above but offers unique advantages. It will make the machine illustrated in Figure 1-2 more versatile and produce a NRS part in a number of different ways.

The shape of the NRS part can typically be divided into rotationally symmetric and NRS components as illustrated in Figure 1-3. This decomposition into two separate components can have a major impact on the fabrication cost, since any rotationally symmetric component may be machined relatively cheaply on a conventional diamond turning lathe. The creation of these two components (not necessarily unique) is a technical challenge that has been addressed at the PEC [11] and will likely be incorporated in future stages of this project. The main axes of the DTM (X and Z) can be used to create any symmetric component (function of radius, r) while the live-axis (Z') adds the non-symmetric component (function of angular location, θ , as well as radius, r).

As the tool feeds from the outside of the part to the center, the linear axes of the lathe move the tool along a median asphere and the Live-Axis simultaneously moves the tool in the Z' direction to include the non-rotationally symmetric component. Together they create the desired optical shape. The range and bandwidth of this auxiliary axis dictate the feed rate and spindle speed and have a direct bearing on the time to fabricate the

surface and the cost. Higher speed and range at the same resolution and accuracy will increase the applicability of this technique to machine NRS surfaces.

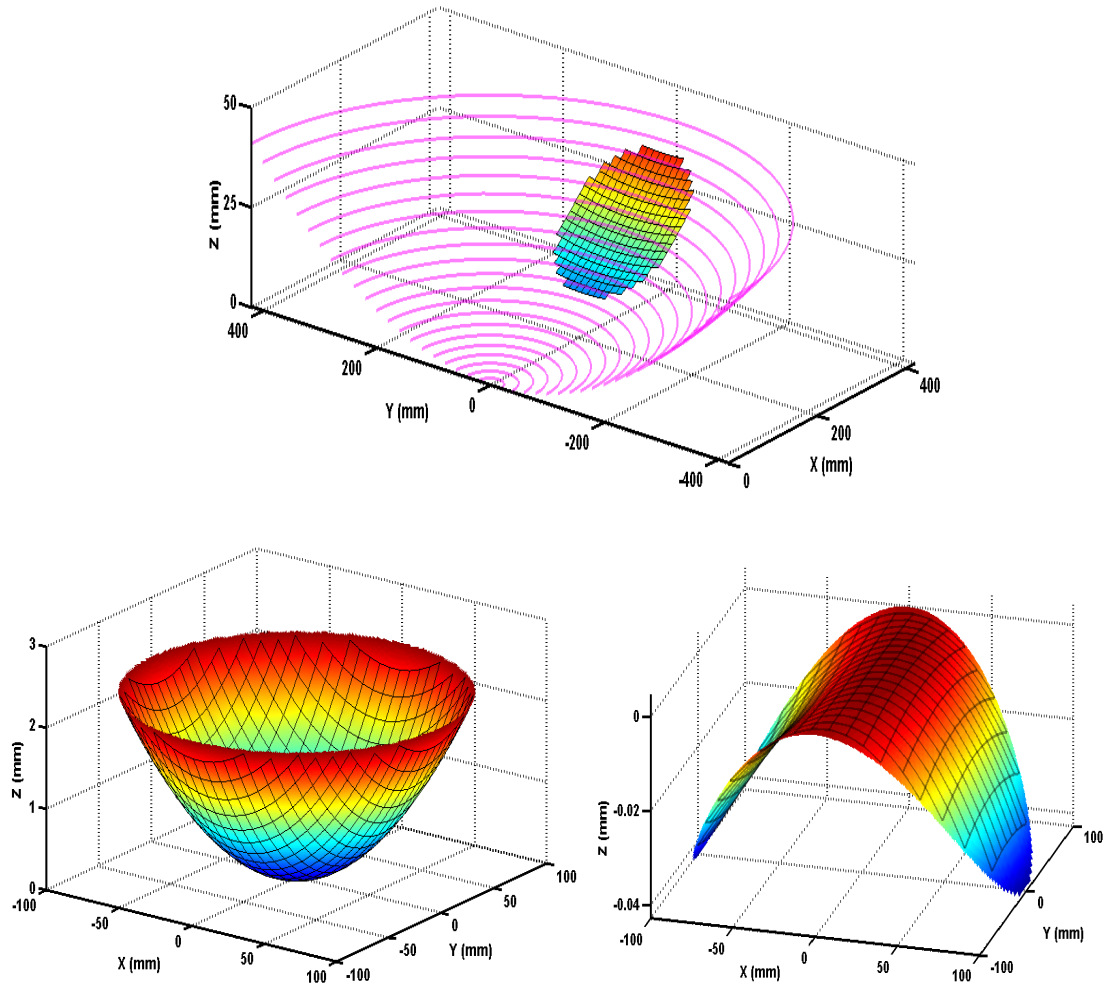


Figure 1-3. Decomposition of off-axis conic mirror surface (top) into symmetric (bottom left) and non-symmetric (bottom right) components for on-axis fabrication (different Z axis magnitudes should be noted).

1.2 Problem Statement

The fundamental innovation of Live-Axis Turning (LAT) is to apply recent advances in precision linear slide design to increase the velocity and range of tool motion and demonstrate a commercially viable device that extends the fabrication capability of NRS surfaces. This technology can be further extended using linear motors, hydrostatic bearings, high-resolution feedback devices and advanced control algorithms. LAT allows NRS surfaces with large departures from rotational symmetry to be machined on a conventional diamond turning lathe at much higher frequencies than are possible with a slow-slide servo. This represents a significant advance in precision machining of free-form optical surfaces over more conventional milling and raster flycutting techniques in that machining times are orders of magnitude shorter, representing both cost advantages as well as avoidance of other problems such as thermal drift associated with very long machining times.

2 System Design

The goal was to develop a high-speed, air bearing, linear motor driven slide with a total stroke of 25 mm. At 20 Hz, the goal is a stroke of 4 mm while maintaining a surface finish of 10 nm. This goal requires the selection of a light but stiff slide material (Section 2.1), choosing an optimal geometry for the slide (cross-section and length, Sections 2.3 and 2.4), specifying a light motor capable of driving the system at the required conditions (Section 2.6) and designing air bearings to guide and support the slide throughout its range of motion (Section 2.8). Also, a damper was added to investigate the effects of physical damping (Section 3.2.3). Figure 2-1 shows how these components fit together in the design. The following sections explain the design process used to select and create these parts.

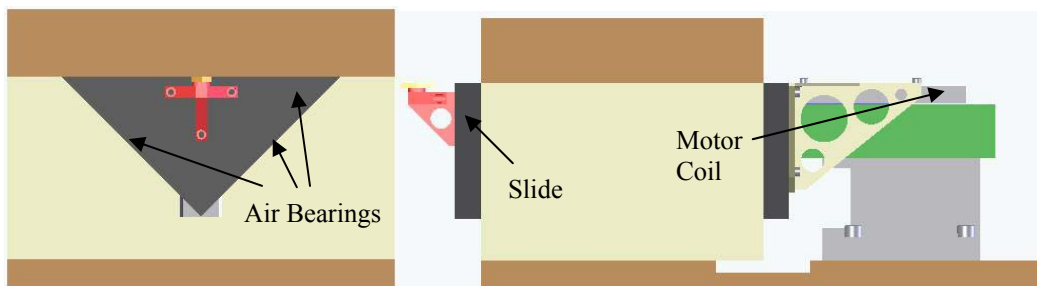


Figure 2-1. Front (left) and side views of general LAT design.

The front view in Figure 2-1 shows the air bearing surfaces that guide the slide, and the side view points out the slide itself and the location of the motor coil, which is the moving part of the motor.

2.1 Slide Material Selection

The system's main moving component- the slide - is aluminum honeycomb. This material was chosen because it provides high stiffness and durability at a fraction of the mass of solid aluminum. It is important to keep the mass low to ensure a high natural frequency for the slide, as the two are inversely related. Additionally, a lower moving mass creates smaller reaction forces on the machine axis, ultimately resulting in a better surface finish.

Aluminum honeycomb has been used in a wide variety of applications, especially in the aerospace industry. Some of these uses include aircraft floors, fuselage components, helicopter rotor blades, and missile wings. Other non-aerospace applications are skis, tennis racquets, ceiling and floor panels and energy absorbers for railway systems (fenders, etc.) [12].

A beam of aluminum honeycomb consists of some volume of honeycomb sandwiched between two thin plates or facing skins of aluminum. The layers are held together by an epoxy joint as shown in Figure 2-2.

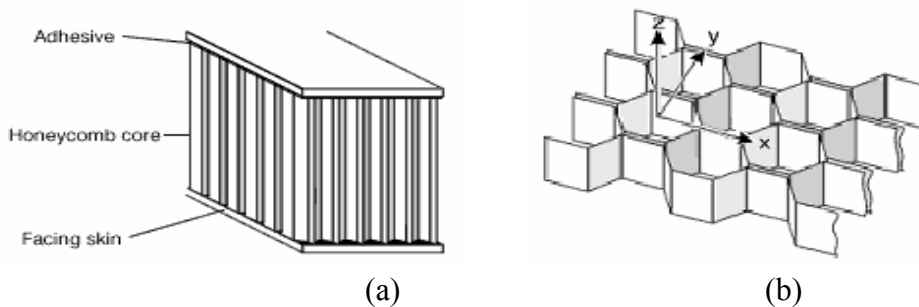


Figure 2-2. (a) A composite aluminum beam. (b) A closer look at the cell structure of the honeycomb [12].

The hexagonal cells are thin strips of aluminum - often only 50 μm thick - and are formed into lines of the honeycomb pattern and joined together along the faces (Figure 2-2(b)).

The facing skins of the composite carry all the bending stresses applied to the beam and act like the flanges of an I-beam. Similarly, the core acts as the web of an I-beam, resisting all shear loads and increasing the stiffness of the beam by keeping the facing skins/flanges away from the centerline. These properties make the aluminum honeycomb a practical choice in lightweight applications, as much stiffness is gained with very little added weight. A comparison between honeycomb beams and a normal I-beam is shown in Table 2-1.

The aluminum honeycomb slide for this project was custom made by Active Precision. The core is three-quarters inch (19.05 mm) thick and the hexagonal cells are one-eighth inch (3.175 mm) on each side. The facing aluminum skin is .04 inches (1 mm) thick. This small cell size will add more stiffness to the structure than a larger cell size would.

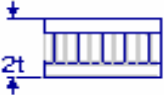
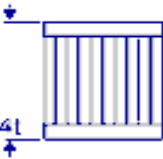
	Solid Material	Core Thickness t	Core Thickness $3t$
			
Stiffness	1.0	7.0	37.0
Flexural Strength	1.0	3.5	9.2
Weight	1.0	1.03	1.06

Table 2-1. A comparison of weight and stiffness between two honeycomb beams and a solid I-beam.

2.2 Honeycomb Modeling Technique

A structural design analysis of the slide based on a finite element model was created through the SolidWorks FEA platform COSMOSWorks. SolidWorks is the 3D modeling software package used to create the slide design. COSMOSWorks is an add-on to SolidWorks that allows models to be imported and analyzed using FEA tools. Modeling is a way for designers to check the design for fit and function and observe how modifications to individual components affect the entire system. This process saves time and allows the designer to convey his/her ideas much more easily and clearly. However, for a model to be considered reliable, it must be accurate on all levels. This means that the structure must be analyzed and tested piece by piece, which may be accomplished by beginning on the most elementary level and working up to the full detail of the model.

Initially, a simple approach was taken in the structural analysis of aluminum honeycomb. Small pieces of the material (with and without the aluminum faces) were subjected to various tests, and the results from these tests were used to create a set of effective material properties for the honeycomb. To minimize uncertainty, each honeycomb beam was modeled as two thin aluminum sheets which sandwich a thicker piece of the honeycomb material. The multi-part approach was used as opposed to modeling each beam as one “effective” material for two main reasons: the properties of aluminum are well known and the thin faces would provide much of the strength of the beam, and the thickness of the faces was not specified, so different sizes were examined.

2.2.1 Honeycomb Material Properties

Most engineering materials are isotropic, meaning they have the same properties in all directions (axial, lateral and in between). However, honeycomb is an anisotropic material, having different properties in different directions. More specifically, honeycomb is orthotropic (a variety of anisotropic). By definition, an orthotropic material has at least two orthogonal planes of symmetry, where material properties are independent of direction within each plane (An anisotropic material has no planes of symmetry and an isotropic material has an infinite number). Some common examples of other orthotropic materials are fiber-reinforced plastics and concrete reinforced with parallel steel bars. It is relatively easy to envision that the core is stiff when loaded in a direction perpendicular to the facing skins, but offers little to no resistance when squeezed from the sides (Figure 2-3).

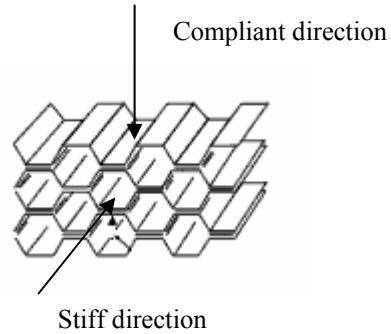


Figure 2-3. The orthotropic nature of the honeycomb core

The orthotropic nature of this material makes it more difficult to model than regular materials because the different material properties for all directions must be specified as inputs for the FEA model. This task becomes even more complex when no material properties are listed by the manufacturer.

To find the honeycomb material properties, a combination of experimental and analytical methods were used. The resulting values were input to the FEA model, and simulations run using these values were compared to experimental data to assess the validity of the model. The following sections describe the analytical methods used to solve for the properties and the experiments performed to gather physical data about the honeycomb. Table 2-2 shows the final values for the honeycomb material properties used in the FEA model.

Property	Description	Value	Units
EX	Elastic modulus in x	55	Psi
EY	Elastic modulus in y	280,000	Psi
EZ	Elastic modulus in z	55	Psi
GXY	Shear modulus in xy	51,000	Psi
GYZ	Shear modulus in yz	51,000	Psi
GXZ	Shear modulus in xz	25,000	Psi
DENS	Density	.00262	Lb/in ³

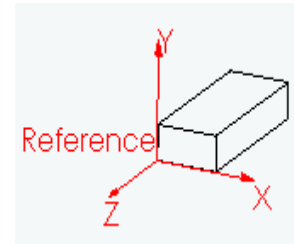


Table 2-2. List of values used to model honeycomb core.

Density

Finding the density of the honeycomb core was a fairly straightforward process. A test beam of aluminum honeycomb provided by the manufacturer was used. The dimensions of the beam gave the volume, and the mass of the beam was found using a balance. By finding the thickness of the aluminum facing skins using a microscope (Figure 2-4), the volume of actual aluminum (skins) could be found. Another useful property was the density of aluminum, known to be 0.0975 lb/in³ (2.7 g/cc).

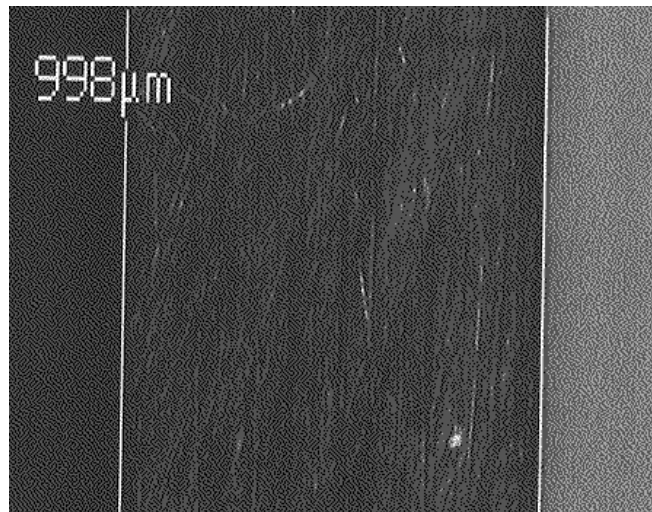


Figure 2-4. Aluminum facing skin, seen at 50X by the Zeiss ICM 405 microscope – approximately 1 mm (0.04 in.) thick.

With the volume and density of aluminum known, the mass of aluminum was found through multiplication. Subtracting the mass of aluminum from the total mass and the volume of aluminum from the total volume leaves the mass of honeycomb and the volume of honeycomb. From this point, simple division gives the density of the honeycomb. This process is summarized in Equation 2-1.

$$\rho_{\text{honeycomb}} = \frac{m_{\text{honeycomb}}}{V_{\text{honeycomb}}} = \frac{m_{\text{total}} - \rho_{\text{aluminum}} V_{\text{aluminum}}}{V_{\text{total}} - V_{\text{aluminum}}} \quad (2-1)$$

$$\rho = \text{density} (\text{lb} / \text{in}^3)$$

$$m = \text{mass} (\text{lb})$$

$$V = \text{volume} (\text{in}^3)$$

The density of the honeycomb was found to be 0.00262 lb/in³ (0.0724 g/cc), and this value was used in the model.

Shear Modulus

The shear modulus in the ribbon direction and the transverse direction (Figure 2-5) were obtained by finding a honeycomb material with published properties [12] that had a very similar density for the 1/8 in. cell size. The shear moduli for the ribbon and shear directions are 51,000 psi and 25,000 psi, respectively.

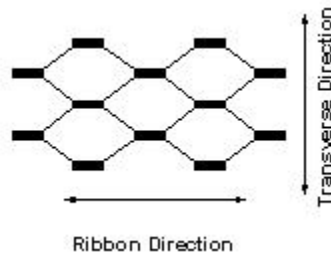


Figure 2-5. Ribbon and Transverse directions in the honeycomb cell structure.

Modulus of Elasticity

While most manufacturers of honeycomb publish values for properties such as compressive strength, crush strength and shear modulus, none list a value for the modulus of elasticity of their products. This is most likely because the type of testing used to find this property would be very difficult to perform on the material. For this reason, a more analytical approach called the equivalent stiffness method was taken to find the modulus.

The underlying principle behind the equivalent stiffness method is that whether the honeycomb is analyzed as a solid area of an equivalent “effective” material or, as in reality, a matrix of very thin aluminum strips, the stiffness must be the same. In other words, no matter how the material is modeled, an applied static force will produce the same deflection (assuming a perfect bond between the materials).

Applying this principle of equal stiffness, the stiffnesses of the effective material and the actual material are set to be equal. Assuming equal length and a one-by-one inch area, solving for the effective modulus of the honeycomb gives

$$E_{effective} = \frac{E_{actual} A_{actual}}{A_{effective}} \quad (2-2)$$

In Equation 2-2, the effective area is one in² and the actual E is the modulus of elasticity for aluminum. The only unknown still needed to find the effective modulus is the actual area. A one-by-one inch area of 1/8” cell size honeycomb contains 18 strips of aluminum roughly one inch long each. To complete the actual area calculation, the thickness of the strips is found by microscope (Figure 2-6) to be 0.001654 in (42 μm). With all

parameters in Equation 2-2 known, the effective modulus (E_y with respect to Table 2-2) was found to be 288,000 psi.

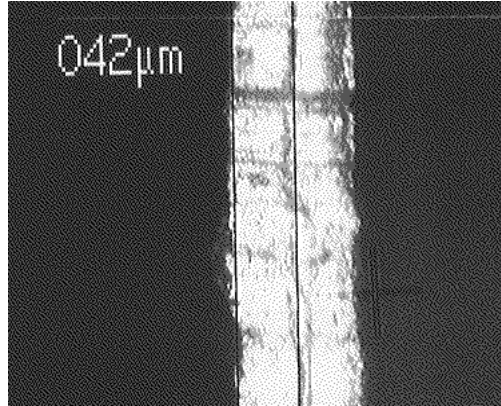


Figure 2-6. Top view of honeycomb core at 200X on the Zeiss ICM 405 microscope. The bright section is two strips of aluminum joined at the faces, so the measured width (the thickness of one strip) is only one-half of the total width.

The moduli in the other directions (E_x , E_z – see Table 2-2) are the same as each other (but different from E_y), and they were obtained through a simple force vs. deflection experiment. A small square of pure honeycomb was removed from a composite beam and one side of the square was fixed. The other side was loaded with a pure compressive force and deflection measurements were made. Then, from Equation 2-2 in the previous analysis, the modulus was found to be 55 psi.

2.2.2 Material Testing

Experimental tests were performed on honeycomb specimens to learn more about how they behave in common loading scenarios. It was important to learn how the facing skins interact with the core, as well as how the entire honeycomb structure acts as a whole.

The tests also provided results with which the model could be compared. Two experiments were conducted to learn more about the composite structure: a four-point bending test and a frequency response analysis.

Four-Point Bending Test A four-point bending test shows how a structural material behaves under static loading. The test is performed on an Instron material testing machine (Figure 2-7).



Figure 2-7. Instron testing machine.

The Instron machine can perform bending tests (the bottom crosshead is fixed and the top crosshead exerts a downward force) as well as tensile tests (top and bottom crossheads pull apart). A beam of aluminum honeycomb was simply supported, and two equal forces were applied on the top at the same distance inward from each support. A general four-point bending setup is shown in Figure 2-8.

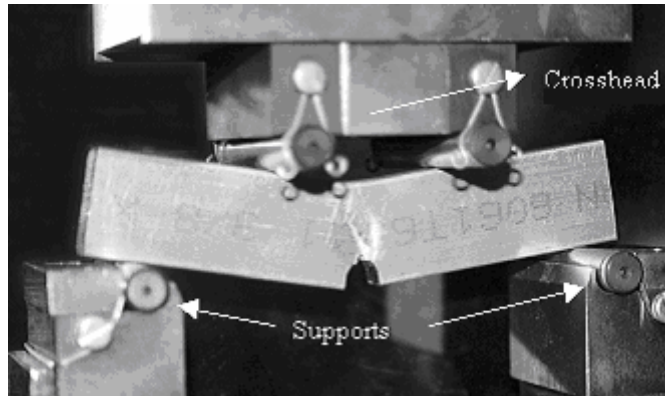


Figure 2-8. An aluminum specimen in a four-point bending test

Prior to testing, the height and width of the specimen were measured, as well as the span between the supports and the distance from each roller to each support. The test began with the rollers of the crosshead lightly touching the specimen, exerting no force. The crosshead then moved down at a constant rate (0.2 in/min) and a load cell under the supports measured the force exerted. The Instron software recorded the force at specified time intervals as measured by the load cell. By knowing speed of the top crosshead, it was possible to plot a load vs. displacement curve for the specimen (Figure 2-9). The elastic region of this curve is shown in Figure 2-10.

The equation shown on the graph is a linear best-fit line for the data. The slope of this line, 20,570 lb/in., represents the static bending stiffness of the aluminum honeycomb. The R^2 value of 0.9989 shows a very strong correlation to a linear relationship, which is expected in the elastic region.

As a check, an equation provided by Hexcel [12] was used to calculate the theoretical stiffness for a beam of the same proportions. The theoretical value was approximately

23,000 lb/in., which supports the findings from the bending test. The theoretical stiffness equations are shown in detail in Appendix A.

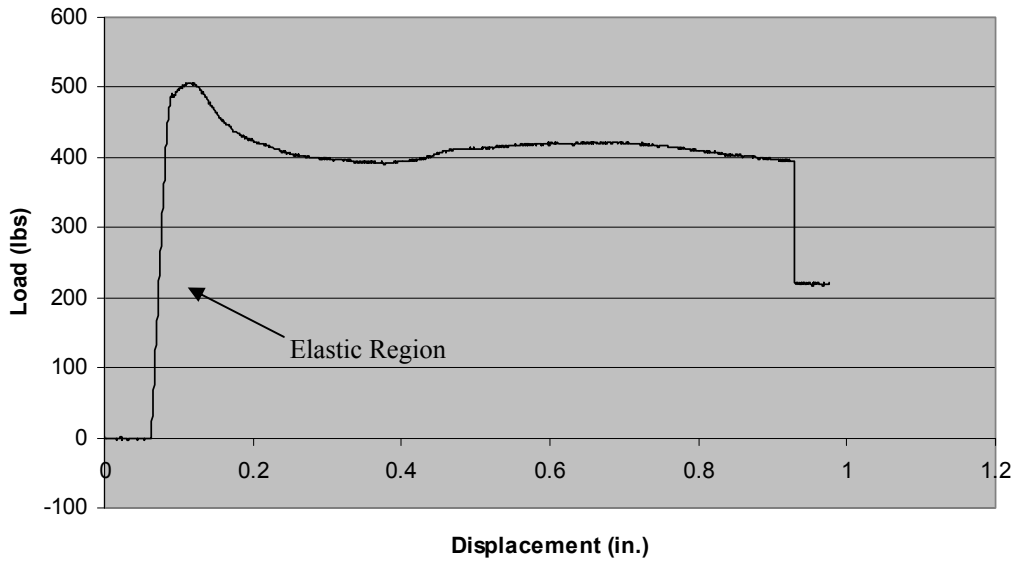


Figure 2-9. Load vs. Displacement for aluminum honeycomb specimen.

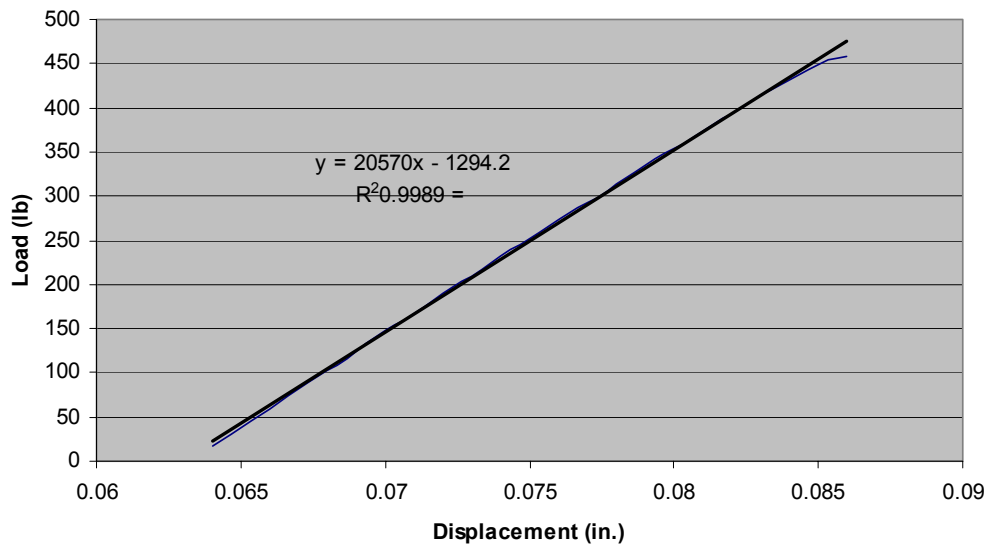


Figure 2-10. The elastic region of the honeycomb Load vs. Displacement plot (labeled in Figure 2-9).

Frequency Response Analysis Frequency analysis is important in any application that involves oscillatory motion. If the system operates at a frequency that resonates the structure, unwanted motion will occur, which can greatly affect following error and, in turn, surface finish.

To test the dynamic properties of the aluminum honeycomb, a free-free test was performed. In this type of test, the test piece of honeycomb is suspended in air by a string. An accelerometer is attached to the piece, and it is struck with an instrumented hammer. The data from the accelerometer is captured using a Stanford signal analyzer, and the resonant frequency of the piece is found. The setup for the free-free experiment is shown in Figure 2-11.

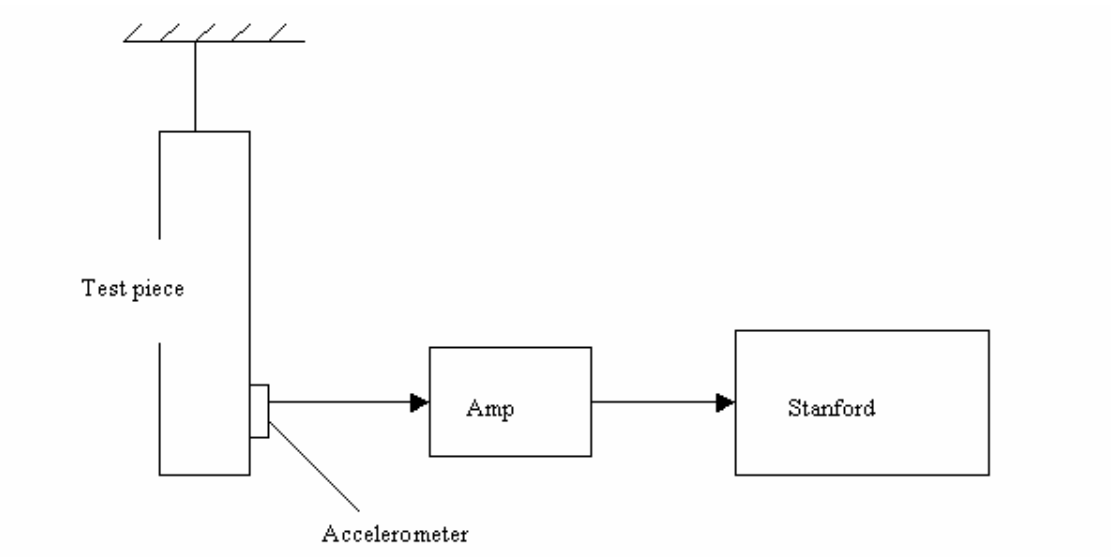


Figure 2-11. Setup for frequency test.

The Fourier Transform of the data collected with the Stanford signal analyzer was taken and plotted along with the magnitude of the motion. A large jump in the magnitude of the signal can be noticed at 2.48 kHz (Figure 2-12), indicating a resonant frequency – the frequency at which the test piece vibrates for an arbitrary input.

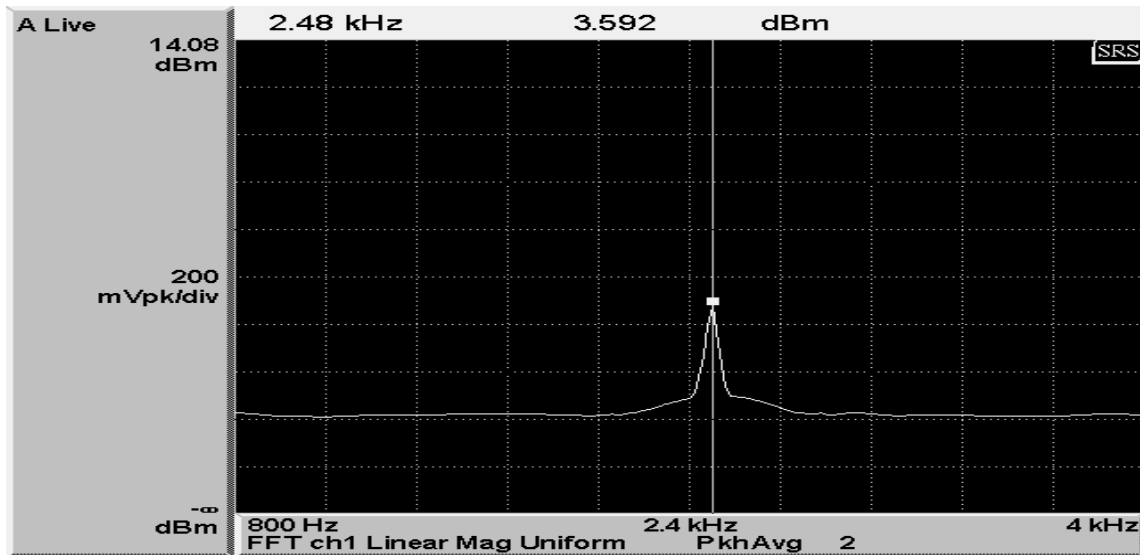


Figure 2-12. Frequency response of aluminum honeycomb sample free-free test.

Resonance occurs at 2.48 KHz.

2.2.3 Comparison of Model and Experiments

To compare the honeycomb model to the measurements of honeycomb's behavior, the material tests discussed earlier were simulated using modeling software. The inputs to the model were the properties detailed in Section 2.2.1. COSMOSWorks, the SolidWorks FEA platform, was used to simulate the tests.

Simulated Bending Test

A simulated bending test was performed by creating a composite beam with a honeycomb core, sandwiched by two aluminum plates (this distinction is not shown in

Figure 2-13 but was taken into account for the analysis). This beam was sized to be the same as the one used in the physical bending experiment. Using the “Constraints” option in COSMOS, the outside edges on the beam were set as immovable (no translation) to simulate the span in the bending test (indicated by the smaller arrows in Figure 2-13). Finally, using the “Force” command, forces were inserted at the proper spots along the beam to simulate the load created by the crosshead of the Instron machine. Static tests were run using different loads, and a force vs. deflection curve was plotted.

These simulated results are compared with the experimental results in Figure 2-14. The graph indicates the simulated model is the stiffest at 25,641 lb/in, followed by the theoretical model at 23,696 (analytical case given by the honeycomb manufacturer’s deflection equations [11]) and the experimental results, 20,602 (lb/in). However, at small loads (up to 100 lb.) the simulation provides very similar results to the experiment. Considering forces higher than a few pounds are not expected in this application, the simulation provides a good approximation for the actual behavior of honeycomb.

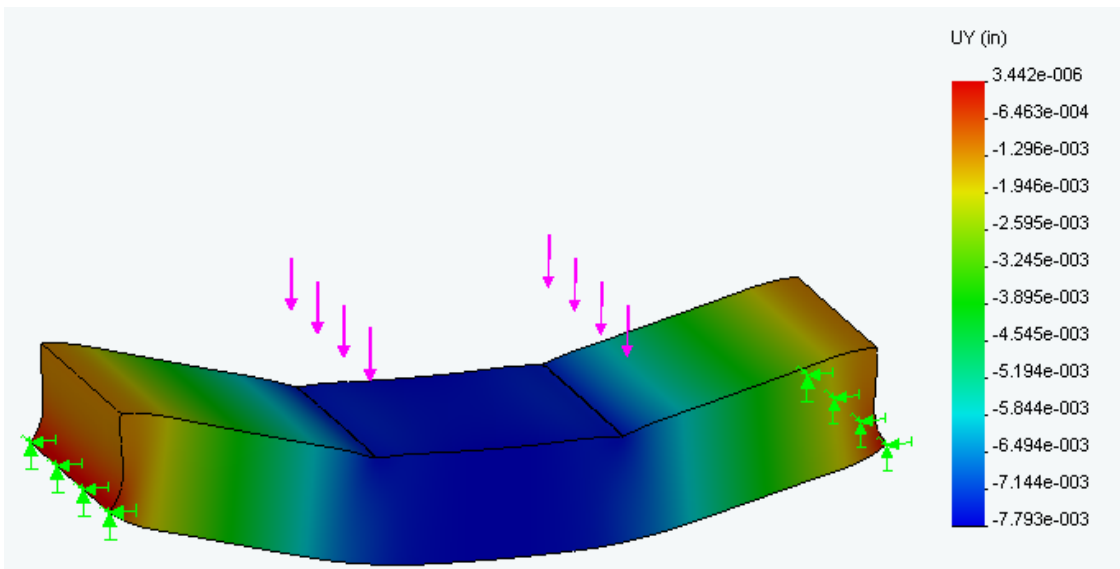


Figure 2-13. Simulated four-point bending test on a beam of aluminum honeycomb modeled as two thin sheets of aluminum bonded to a honeycomb core. The load shown is 200 lb., and it corresponds to a deflection of 0.0078 in.

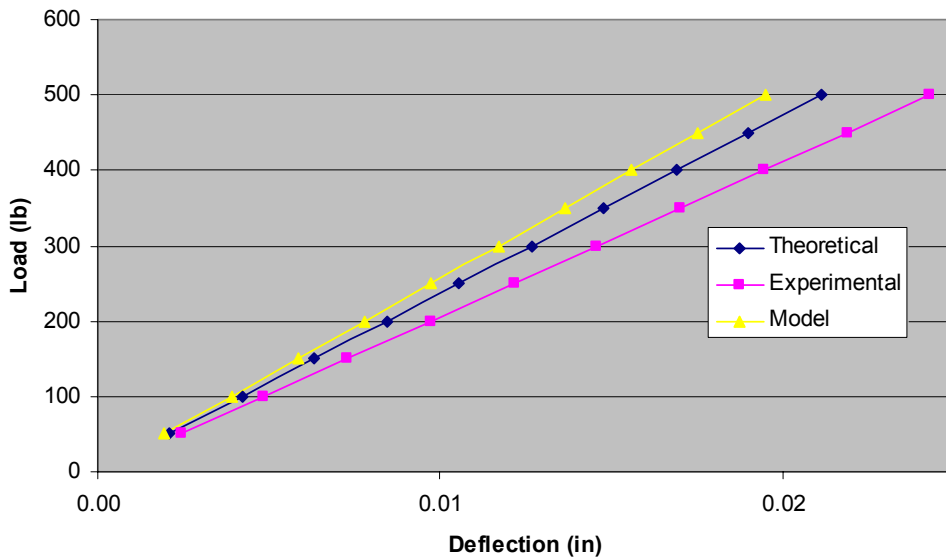


Figure 2-14. Load vs. Deflection plot for aluminum honeycomb of fixed geometry. Theoretical refers to the analytical solution, Experimental is from the Instron machine, and Model is the FEA results.

Simulated Frequency Test

Like a static bending test, a frequency analysis can be performed fairly easily in COSMOSWorks. Creating a model of the same dimensions as the frequency test piece, the assumed properties of honeycomb were input into the composite, which was once again two sheets of aluminum with honeycomb in between. Since the experiment was conducted with free-free conditions, no restraints or forces are needed in the simulation. However, it is important ignore the first six modes (rigid body modes) and observe the seventh mode of vibration. The seventh mode for a plain beam is shown below. The mode shape is shown in Figure 2-15 and the frequency associated with this shape is 2800 Hz.

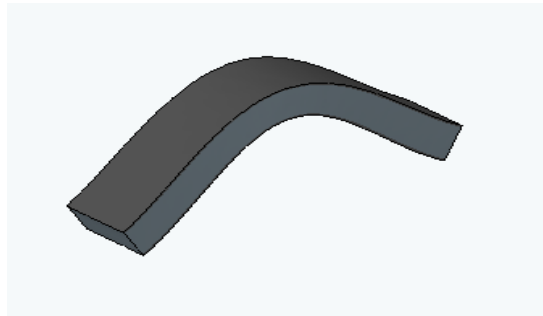


Figure 2-15. Free-free vibration of an aluminum honeycomb beam. This first free-body mode occurs at 2800 Hz.

The frequency simulated for the honeycomb beam is about 10% higher than those obtained through the experimental method. However, non-uniform bonding (Figure 2-16) was noticed on some fractured specimens and may have lowered the natural frequency of the actual test piece. While the simulation assumes a perfect bond everywhere between the honeycomb and aluminum, this may not be the case for the test specimen. Figure 2-16 shows a close-up view of the underside of a facing skin on one of

the honeycomb test pieces. It is clear that the glue used to bond the surfaces is heavy in some areas and virtually absent in others. This inconsistency could have had an adverse affect on the frequency performance. Nonetheless, the 10% difference between model and experiment was considered an acceptable error.

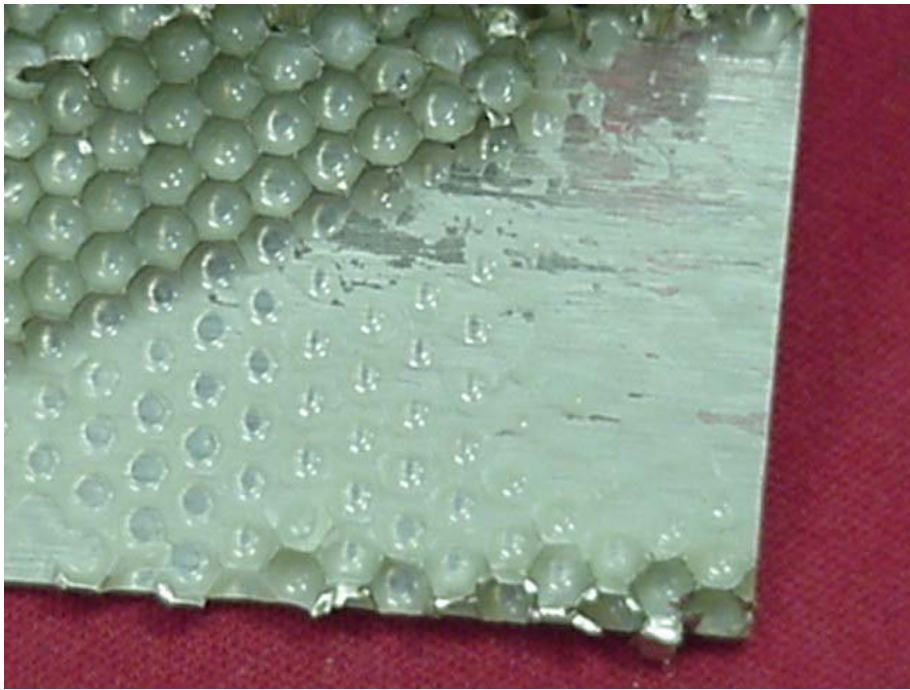


Figure 2-16. The underside of an aluminum facing skin (with some honeycomb attached). The uneven distribution of the glue may have yielded a slightly lower natural frequency than a perfectly bonded specimen.

2.3 Slide Cross-Section

With an appropriate model of the honeycomb, the design process began by examining different types of slide geometries. The shape, or cross-section, was the initial focus. The goal was to select a slide shape that provides high structural stiffness, would be relatively easy to manufacture and reduce force and measurement offsets. Three designs

were originally considered and will be discussed in this section: the box, V-shape, and triangle designs.

2.3.1 Box Design

The box design features a rectangular slide with a cutout from the top to allow a motor coil (the moving component of the motor) to be embedded. The slide housing consists of two “L” shaped parts, as shown in Figure 2-17.

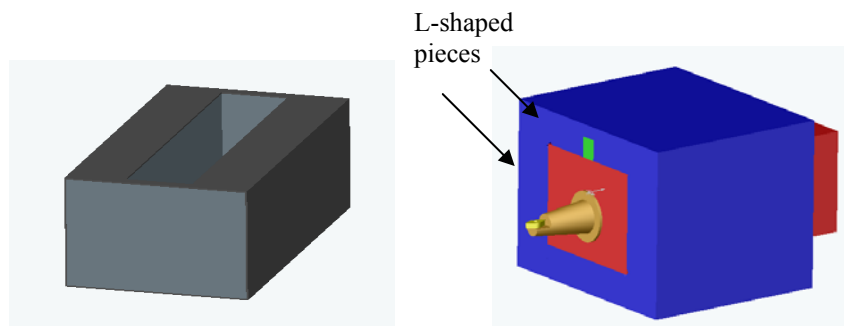


Figure 2-17. (Left) Simplified box design (darker, outer shell is aluminum; lighter parts are honeycomb). Cutout is needed so motor may be embedded. (Right) Box design shown with housing. The rectangle in the middle represents the slide shown on the left.

2.3.2 V-Shape Design

The V-shape slide design consists of two aluminum honeycomb beams joined at a 90° angle. The motor coil rests on a triangular spacer (Figure 2-18) that runs the length of the slide. This spacer provides a flat surface to mount the motor coil. Allowing the coil to sit down in the V-shape greatly reduces the coil force offset at the tool as described in Section 2.3.4. The housing consists of four main parts: the top, bottom, and two rectangular spacers that run the entire length. The rectangular spacers ensure the proper

air gap necessary for the bearing to achieve optimal performance. Additionally, the rectangular spacers are easily replaceable and can be modified to assist assembly much more effectively than a two-piece housing.

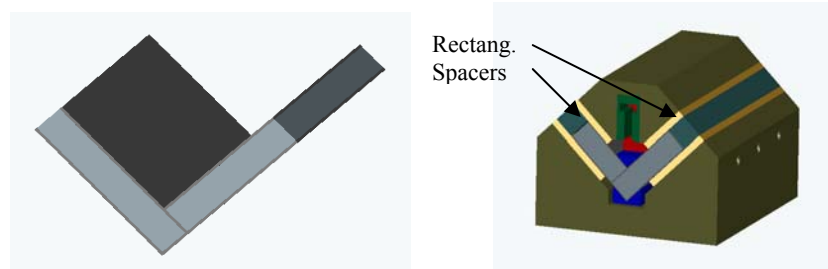


Figure 2-18. Simplified V-shape design (left) and V-shape slide with housing (right).

2.3.3 Triangle Design

The triangle design was very similar to the V-shape design, but it had another honeycomb beam connecting the sides. It was originally designed with a small cutout in the back to embed the motor and reduce coil force offset (Section 2.3.4), however the design was changed to hang the motor coil off the back of the slide instead of embedding it (final design shown in Figure 2-19). This small change increased the structural natural frequency of the slide. The housing is two pieces, with the bottom having a small channel in the middle down the entire length to allow room for the vertex of the slide.

This design also includes faceplates on the front and back, but they were excluded from this analysis to maintain consistency. The housing is two pieces, with the bottom having a small channel in the middle down the entire length to allow room for the vertex of the slide.

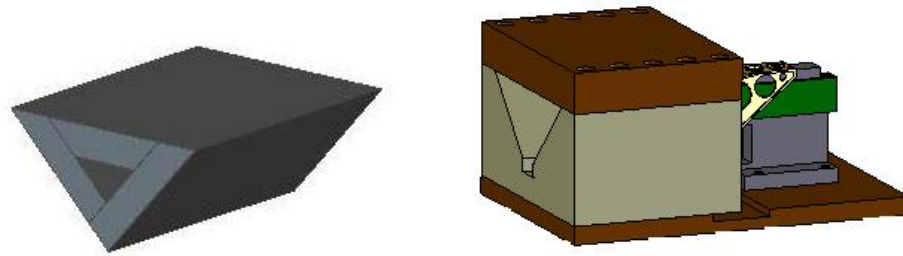


Figure 2-19. Simplified view of the triangle design (left) and the housing for this design (right).

2.3.4 Shape Comparison

Each design had strengths and weaknesses, so four main criteria were used to decide among them: moving mass, natural frequency, motor offset and number of parts.

Moving Mass – It was important to keep the moving mass of the slide as low as possible. As moving mass decreases, so does the force needed to drive the system. Since the force a motor can produce is proportional to its size, smaller required force for the system meant a smaller motor could be chosen, reducing bulk and mass. For a fixed motion amplitude and frequency, the reaction force produced by the system increases linearly with mass. High reaction forces can excite the base of the turning machine, producing unwanted vibration.

Natural frequency – The higher the slide/moving mass natural frequency, the faster the system can operate (higher frequency) without the possibility of exciting a physical resonance and producing unwanted motion.

Motor coil force offset – When a voltage is applied to the motor coil, the magnet track in turn produces a force on the I-shaped coil. This force acts through the center of the I-beam web (the vertical line in the “I” shape is referred to as the “web”). If the center of force of the coil (center of the web) is not aligned with the center of gravity (CG) of the slide, some moment will be created, causing a pitching motion in the slide. Naturally, this offset distance should be minimized to reduce the moment forces. The distance between the slide CG and the coil center of force is the coil force offset.

Number of parts – Cost and ease of manufacturing was the final issue to be considered. An assembly with more parts is less favorable than one with fewer parts.

	Box	V-shape	Triangle
Moving mass (g)	450	400	445
First natural frequency (Hz)	1900	3450	3950
Coil force offset (in)	<0.05	.85	1.5
Number of parts (slide not included)	2	4	2

Table 2-3. Comparison between slide shapes.

Table 2-3 presents a comparison between the designs using the preceding criteria. The table shows a similar moving mass for all designs. There is a large gap between the first natural frequency of the box design and the other two designs because so much material was removed to embed the motor coil in the box design. This left thin outer walls susceptible to vibration at relatively low frequencies. The triangle design has the largest coil force offset because the coil must sit up on the triangular spacer (Figure 2-18), and, based on the number of parts, the V-shape design will be most difficult to manufacture.

After reviewing the design chart, the box design was eliminated, mainly due to its bulky size and low natural frequency. With the comparison down to the triangle and V-shape designs, a closer look was taken at the stiffness of each design.

Although natural frequency does depend on stiffness, a comparison of how the two designs respond to a static load would provide useful information. It should also be noted that in the frequency analysis, the V-shape design was considerably smaller than the triangle. This means the first natural frequency would be lower for a V-shape slide of similar proportions as the triangle.

To study this static loading affect, a simulated bending test was conducted. The slide was fixed-free, like a cantilever beam, and a force of 100 lb was applied at the free end, as shown in Figure 2-20.

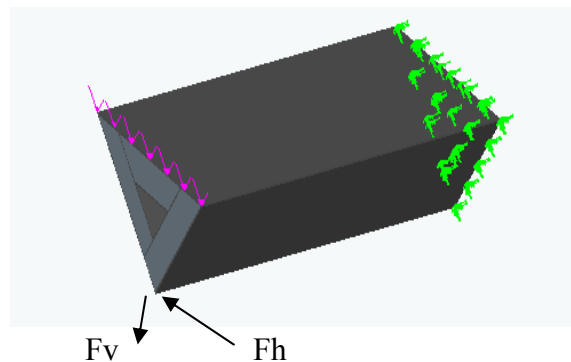


Figure 2-20. Static loading test simulation setup for the triangle slide

While the stiffnesses of the designs were similar in the vertical direction, the triangle slide was much more resistant to lateral forces (Table 2-4), which were applied at the bottom vertex of each design during the simulations. Additionally, the triangle design

only required two parts for assembly (base, top) while the V-shape design required four (base, top, two spacers). The combination of these facts led to the selection of the triangle design.

	Mass (g)	Nat.Freq. (Hz)	Lateral stiffness (N/ μ m)	Vertical stiffness (N/ μ m, Figure 2-20)	# Parts for assembly
V Shape	400	3450	8.145	8.17	4
Triangle	445	3950	25	10.5	2

Table 2-4. Comparison of V-shape and triangle slide designs. The triangle design was chosen because of its high stiffness and relative ease of assembly, shown by the fewer number of parts.

2.4 Slide Length

Choosing an appropriate length for the slide was a very important part of the design process, mainly because this parameter has an effect on so many things. Stiffness decreases with length when all other aspects are fixed. This implies that the structural natural frequency of the slide will decrease with length, as stiffness is proportional to natural frequency.

Another effect of changing slide length is the air bearing stiffness. As described in the introduction to Section 2, the air bearings support and guide the slide. With a longer slide, the air bearing can be made longer, thus increasing its effective surface area. As shown in Equation 2-3 [18], bearing stiffness is proportional to area, so all natural frequencies associated with the bearing will rise as the length of the slide increases.

$$k \propto \frac{AP}{d}$$

(2-3)

A = effective area
P = pressure
d = clearance

The moment stiffness at the tool tip is also affected by bearing stiffness, making a bearing with greater stiffness less sensitive to tool tip forces in the vertical direction.

The first step of the length analysis was to observe how the different modes of vibration change with changing slide length. The structural vibration is defined as the vibration of the moving parts of the system, including the slide, motor coil, and coil mount bracket. This analysis was done in COSMOSWorks, and two distinct modes of vibration occurred: vertical bending and horizontal twisting. These two mode shapes are shown in Figure 2-21.

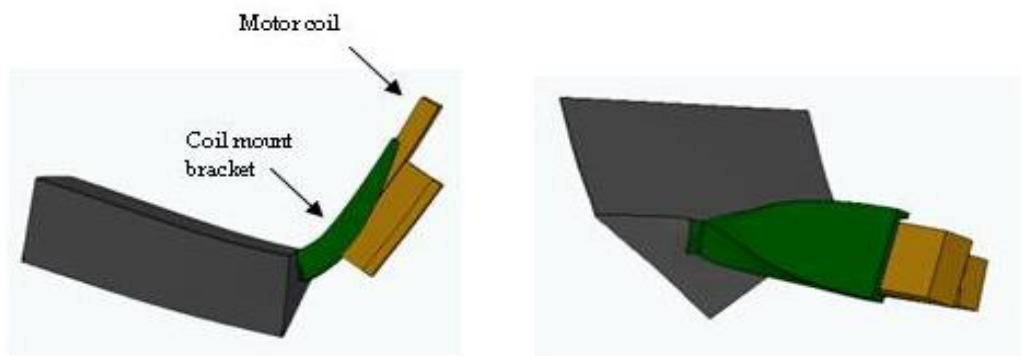


Figure 2-21. Vertical bending (left) and horizontal twisting modes of the slide-bracket-coil assembly.

The bearing stiffness also has an effect on slide vibration. In this case, the slide, bracket and coil act as one rigid body suspended on springs that have a combined stiffness equal to that of the bearing (Figure 2-22).

The translational natural frequency is found by simply using Equation. 2-4:

$$\text{natural frequency} = \sqrt{\frac{\text{bearing stiffness}}{\text{moving mass}}} \quad (2-4)$$

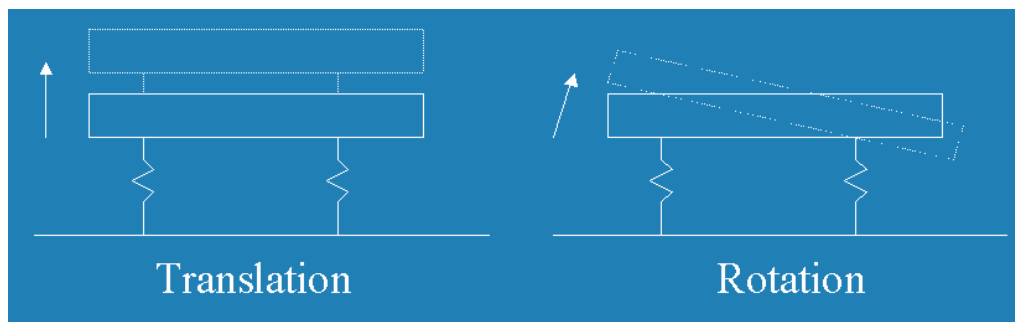


Figure 2-22. Rigid body modes of vibration due to the bearing.

The analysis for the rotational natural frequency assumes rigid body motion and purely rotational motion. Equation 2-5 was used to obtain the natural frequencies [13].

$$\omega_n = \frac{1}{2\pi} \sqrt{\frac{2ka^2}{J}} \quad (2-5)$$

$k = \text{one - half of total bearing stiffness (lb / in)}$
 $a = \text{one - third of bearing length (in)}$
 $J = \text{mass moment of inertia (lbm * in}^2\text{)}$

A total bearing stiffness of 1.3 million lb/in was used in the calculations (See Appendix B for more details). The results for all types of vibration for a variety of slide lengths are shown below in Table 2-5.

Piston Length (in.)	Coupled with Air Bearing		Structural	
	Predicted Translational	Rotational Natural	Natural Frequency (Hz)	
	Natural Frequency (Hz)	Frequency (Hz)	Vertical	Horizontal
6	3134	1841	1574	1105
7	3312	2111	1509	1059
8	3455	2344	1431	1011
9	3572	2552	1369	974

Table 2-5. Comparison of the translational and rotational natural frequencies due to the bearing stiffness and the vertical and horizontal natural frequencies of structural vibration.

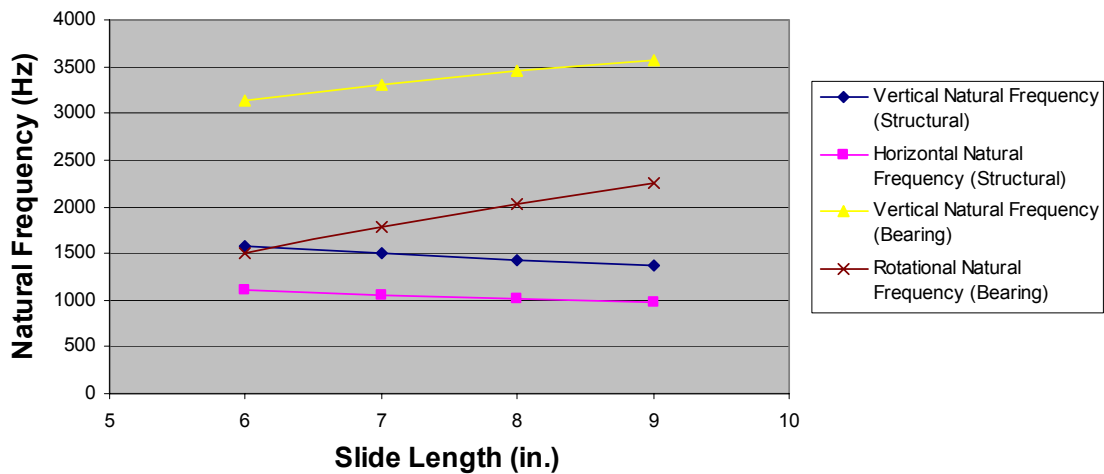


Figure 2-23. Graphical comparison of structural and bearing natural frequencies.

The table shows the natural frequency due to a coupling with the air bearing (translational and rotational) and the structural natural frequency for slides of different lengths. The information is represented graphically in Figure 2-23. The line marked “Structural” in the legend refer to the structural natural frequency of the slide and the lines marked “Bearing” represent the natural frequency of the slide-bearing coupling. Figure 2-23 shows the structural vibration occurs at lower frequencies (around 1000 Hz) than those types due to the bearing (rotational – 1500 Hz, vertical – 3000 Hz). However, an

increased bearing stiffness decreases tool tip deflection. Also, a shorter slide will have a smaller moving mass, decreasing the forces generated on the machine base due to oscillatory motion (base reaction forces). To further help in making the optimum choice, the tool tip moment stiffness for varying slide lengths was examined.

To find the moment stiffness at the very front of the slide (in lb/ μ rad), the system was assumed to be a finite, free-free beam on an elastic foundation (the bearing). With the foundation (bearing) stiffness known as a function of length and the material properties known, bearing lengths of 4.5", 5.5", and 7" were analyzed. These bearing lengths correspond to slides of length 6", 7" and 8.5", respectively, because geometry constraints set the slide length approximately 1.5" longer than the bearing length.

The analysis produced the results shown in Table 2-6 and is covered in full detail in Appendix B. These results show a considerable jump in stiffness (29%) from the six inch slide to the seven inch slide, but a much smaller increase (11%) when going up to eight and one-half inches. Therefore, increasing the length of the slide past seven inches will not add enough stiffness to justify the drop in the slide's structural natural frequency. For this reason, a seven inch slide was selected.

Slide Length (in.)	Moment stiffness (lb-in/ μ rad)
6	1.18
7	1.52
8.5	1.74

Table 2-6. Tool-tip moment stiffness for different slide lengths.

2.5 Experimental Verification of Slide Design

Active Precision in Keene, NH fabricated two slides for the LAT system. The first was shipped to the PEC immediately after completion for testing. The second was sent to Precitech to be assembled in the actual system. Upon receiving the test slide, experiments were performed to assess the validity of the FEA model used to analyze and design the system. These experiments are explained in the following section.

2.5.1 Bending Test

A bending test was performed on the slide to assess the validity of the results from the simulated bending test in COSMOS. The setup consisted of the slide, a Chatillon force gauge and a Federal gauge (Figure 2-24).



Figure 2-24. Setup for the slide bending test. Force was applied at the vertex of the triangle, and the deflection was measured below.

Although a cantilever test was used for the prediction, a simply supported test was implemented in the experiment. This is because the “fixed” boundary condition of the cantilever test is very difficult to replicate in a physical experiment.

The results from the bending test are shown in Figure 2-25 in a Force vs. Displacement plot. The fact that the relationship does not become linear until about 20 lbs are applied indicates that there is some settling in the support, most likely in the protective cloth. Also, it should be noted the stiffness for this beam is less than the stiffness given on page 32 because a smaller length was used in the former analysis.

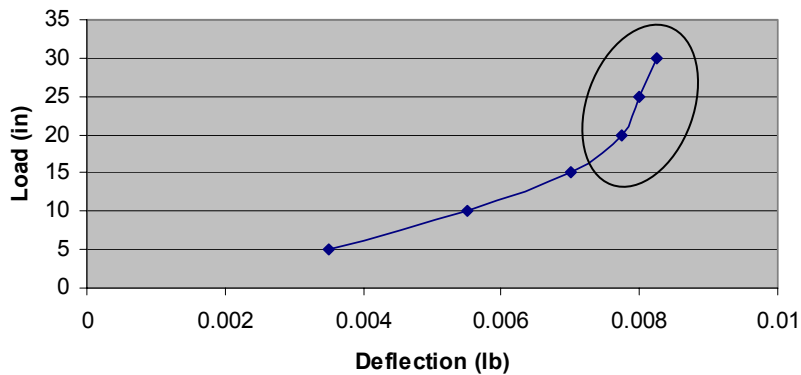


Figure 2-25. Force vs. Deflection plot for the slide bending test. The elastic region is located inside the circle.

Using the experimental data, it was possible to find the flexural rigidity, EI , of the slide using Equation 2-7, the deflection of a simply supported beam under a midpoint load [13]:

$$y = \frac{Wl^3}{48EI} \quad (2-7)$$

Where y is the deflection (in.), l is the length from either edge to the midpoint (in.) and W is the load (lbs.) in the simply supported setup. The flexural rigidity could then be used

in the cantilever deflection Equation (2-8) to find the expected deflection based on experimental results.

$$y = \frac{Wl^3}{3EI} \quad (2-8)$$

For any arbitrary load, W , the deflection predicted by the model is only about 60% of the actual deflection. The original material testing in Section 2.2.2 indicated the model was off by about 20%, but the additional error noticed in this experiment was unexpected. However, calculations show that, under typical cutting forces (<1 N), the cantilever bending deflection of the slide will lead to a tool tip deflection less than 10 nm.

2.5.2 Frequency Analysis

One reason for selecting the triangle design was its high natural frequency compared to the other designs. From the COSMOS FEA analysis, the predicted first and second modes of vibration of the triangle slide occurred at 3950 Hz and 5110 Hz, respectively, as described in Section 2.3.4. The shapes of these modes are shown in Figure 2-26. The first mode (pictured on the left), is a twisting mode and the second mode is bending.

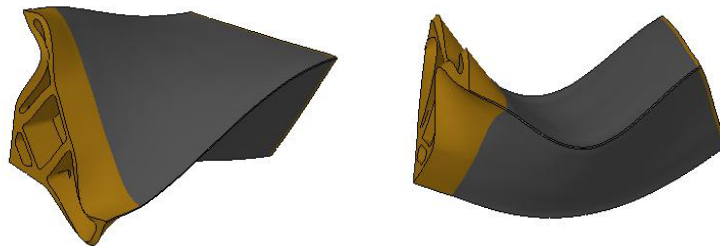


Figure 2-26. First (left) and second (right) predicted modes of vibration for the triangle slide. The first mode (twisting) occurs at 3950 Hz and the second (bending) at 5110 Hz (results from COSMOS FEA analysis).

To find the vibration modes for the slide experimentally, a frequency test similar to the one described in Section 2.2.3 was performed. However, the slide rested on pieces of soft foam in this case to simulate a free-free environment (Figure 2-27). The slide was struck in different places to excite different modes, and an accelerometer on the slide (top right corner of Figure 2-27) recorded the resulting motion.

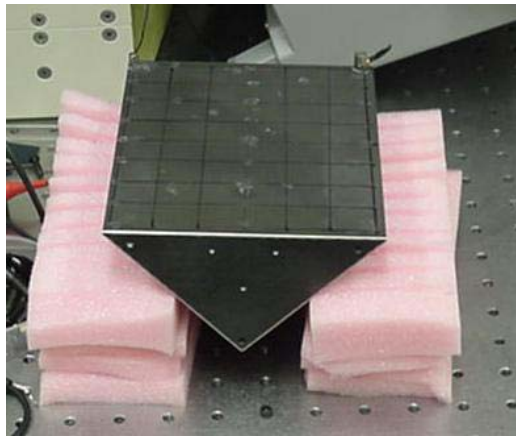


Figure 2-27. Setup for the slide frequency analysis (left). An accelerometer is seen attached to the far right corner of the slide. The accelerometer amplifier is shown on the right.

The signal from the accelerometer was amplified with the Bruel & Kjaer charge amp and sent to a Stanford signal analyzer, where the FFT of the signal was plotted. Repeated testing showed two different dominant spikes, the frequency of which depended on where the slide was struck. These results are shown on screens from the Stanford Signal Analyzer in Figure 2-28. When excited in the center (top plot), a large spike in the FFT appeared at 3540 Hz. An impulse to the corner of the slide (bottom slide) resulted in a spike at 4660 Hz. These are the magnitudes of the first and second modes of vibration, respectively.

While the frequency of vibration was relatively easy to find, the mode shapes were more difficult. To do so, a grid was drawn on the slide (Figure 2-29), and locations on the grid numbered. Two accelerometers were placed at different grid locations, and the slide was excited. The phase and relative magnitude of the two signals were recorded, and the test was repeated with the accelerometers in different spots.

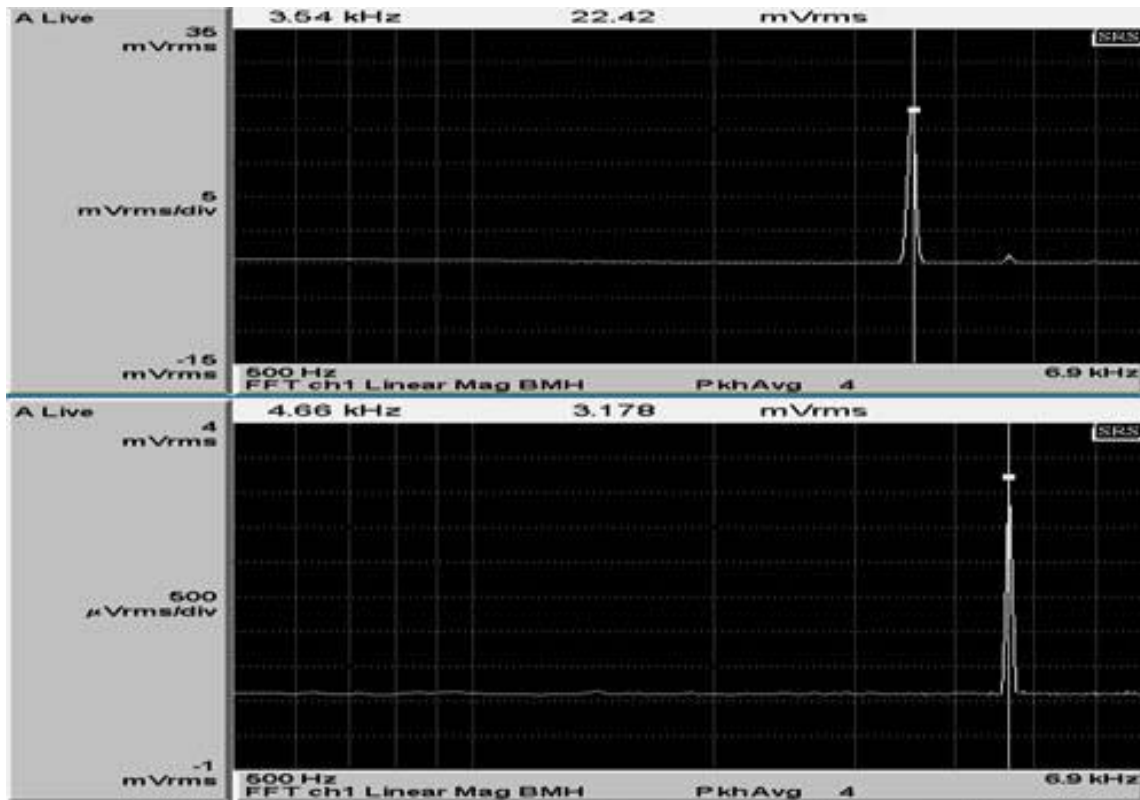


Figure 2-28. Magnitude results from slide frequency test. When the slide was struck in the middle, a spike around 3550 Hz occurred (top plot). When struck at the corner, the dominant frequency was around 4660 Hz (bottom).

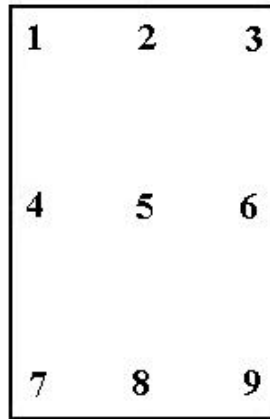


Figure 2-29. Layout of the slide grid used in the frequency analysis.

With phase and relative magnitude data from the top surface of the slide, the mode shape can be determined. For example, when the slide was struck repeatedly in the corner, nodes 1 and 9 were in phase with equal magnitude while nodes 1 and 7 were out of phase with equal magnitude. Additionally, 1 and 3 were out of phase, and very small amplitude was always seen at node 5. These characteristics indicate a twisting motion just like the first predicted mode shape shown in Figure 2-26. Similarly, data obtained from striking the slide in the middle revealed a bending motion like the second predicted mode shape.

The results of this experiment are compared with the predicted results in Table 2-7. The comparison shows that, although the frequencies are a little lower than expected, the ratio between the first and the second modes is essentially identical. Additionally, the actual mode shapes were the same as the predicted mode shapes, validating the model. The drop in frequency is most likely due to small changes in the structure and geometry of the slide from the material property development stage to the manufacturing stage.

	1st Natural Frequency (Hz)	(shape)	2nd Natural Frequency (Hz)	(shape)	Ratio of First/Second
Predicted Results	3950	twisting	5110	bending	0.77
Actual Results	3540	twisting	4660	bending	0.76

Table 2-7. Comparison of predicted and actual results for a slide frequency analysis.

2.6 Linear Motor

A brushless linear motor was chosen for its smooth motion characteristics, high accuracy, repeatability, high acceleration capabilities and stiffness. Also, this type of drive has exhibited quality performance in many other applications [14,15]. This device consists of a series of copper wire coils embedded in epoxy that rest in a channel of permanent magnets. When the current in the coils is varied, the epoxy solid moves linearly down the track (Appendix C). First, a motor was sized and selected. Then, the motor was analyzed so a realistic finite element model of the motor could be created. A brief theory of operation for linear motors is given in Appendix C.

2.6.1 Motor Selection

To reduce the moving mass of the system, the smallest/lightest motor capable of producing enough continuous force to drive the system under its most strenuous operating conditions (2 mm at 20 Hz) was desired. Equation (2-6) was used to determine the maximum force needed to drive the system in a sine wave motion:

$$F = mA\omega^2 \quad (2-6)$$

m is the mass in Kg, A is the amplitude in m and ω is the frequency in rad/sec. For an assumed moving mass of 500 g, an operating frequency of 20 Hz and an amplitude of 2 mm (for a total stroke of 4 mm), 15.8 N are needed to drive the system. From the Airex Linear Motor P12 Series, the P12-1 was chosen (continuous force 27 N, peak force 84 N, see Appendix D for specs). The moving mass of the motor is 100 g.

2.6.2 Motor Analysis

Moving the motor coil to the rear of the slide instead of embedding it greatly reduced coil force offset and raised the structural natural frequency of the slide. Figure 2-30 shows the difference in these two approaches. On the left is the embedded coil configuration, where the motor coil sits down in the slide. The right picture shows the slide-bracket-motor coil configuration. Since the center of force of the motor coil is lined up with the center of gravity of the slide, the coil force offset is virtually eliminated. However, due to the motor coil mass (100 g), a moment that tends to cause pitching of the slide is created. To analyze the effect of this moment, it was first necessary to understand the make-up and properties of the motor coil itself.

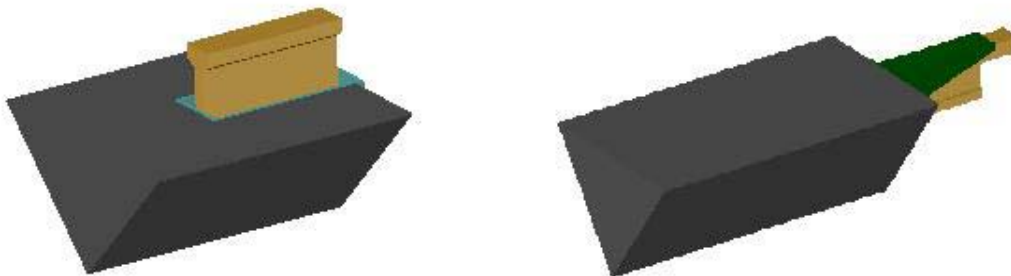


Figure 2-30. Embedded motor coil design (left) and rear-attached motor coil design.

The Airex P12-1 Linear motor is roughly 1.5” tall, 3/4” wide, and 2.5” long. It consists of an aluminum base which houses the “I-coil.” The “I” is a composite that has many tight wire wrappings cured in Stycast 2850 FT-FR epoxy (Figure 2-31). The properties of the composite are neither copper nor epoxy. For this reason, it was necessary to experiment with the motor coil to find its true mechanical properties.

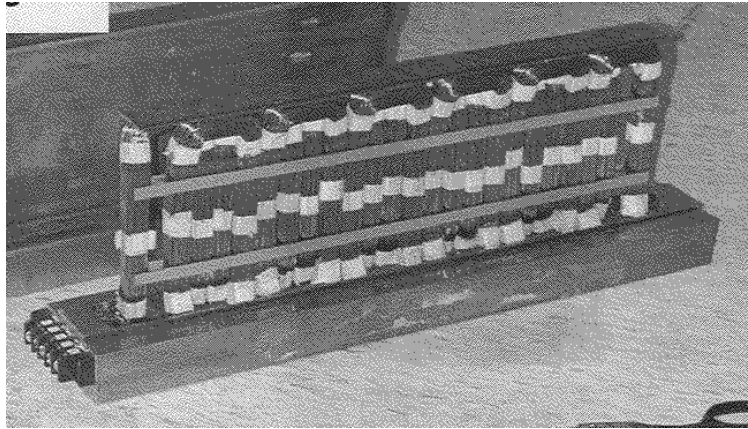


Figure 2-31. Cutaway view of a linear motor I-coil. The banded strands of copper wire can be seen.

The experiment performed was a simple bending test, using a Federal electronic indicator and a Chatillon force gauge. Different loads were applied to the simply supported I-beams shown in Figure 2-32, and the deflection was measured with the Federal gauge. From this data, an average stiffness was calculated. Using this value and knowing the formula for the theoretical stiffness for a simply supported beam, the transformed area method was used to solve for the modulus of elasticity.

The data from the bending experiments and transformed area method are displayed in Appendix E. The results yielded an elastic modulus of 1.88×10^6 psi for the copper-

epoxy composite. This value is approximately 25% higher than the modulus of the epoxy by itself, indicating that the copper coils stiffen the structure in bending.

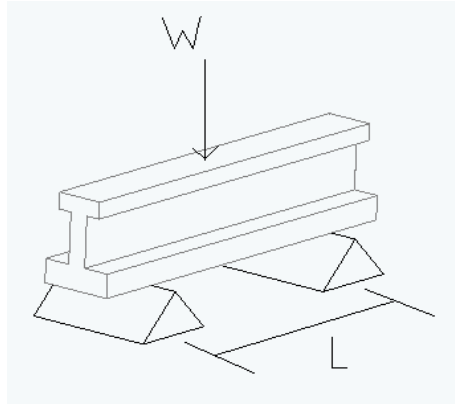


Figure 2-32. Experimental setup for the motor coil bending test.

2.7 Motor Mount Bracket

2.7.1 Bracket Design

The bracket connecting the motor and slide is a very important part of the slide design. It must allow the motor enough room to have one inch of travel but also be as short as possible to minimize the moment arm of the motor weight. Another issue was size: a bigger, bulkier bracket would help add stiffness to the structure but would also add unwanted weight to the moving mass.

The design consisted of a bracket with a flat, square plate on the front, a length that covered the coil until just after the bolt holes, and vertical gussets on each side for bending support (Figure 2-33). All parts of this bracket were 1/16" thick.

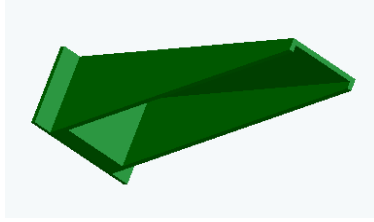


Figure 2-33. Original design of motor mount bracket.

A simulated frequency analysis in COSMOSWorks revealed a few flaws in this bracket. First, local deformation occurred at the flat front plate of the bracket, indicating a thicker front plate was needed. Also, the first mode of vibration for the entire slide-bracket-motor system showed most of the deflection in the bracket and very little if any deformation in the slide or motor (Figure 2-34). The ideal bracket design would be as stiff as the slide or motor coil.

To make the bracket more rigid, two major changes were made. First, the thickness of the front plate was doubled from 1/16" to 1/8". Also, the front plate was made taller to increase the moment of inertia of the structure. Holes in the vertical gussets were also added to reduce weight without sacrificing stiffness. The improved bracket is shown in Figure 2-35.

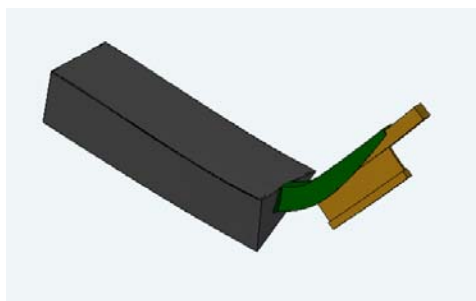


Figure 2-34. The first mode of vibration of the system using the original bracket showed significant deflection in the bracket.

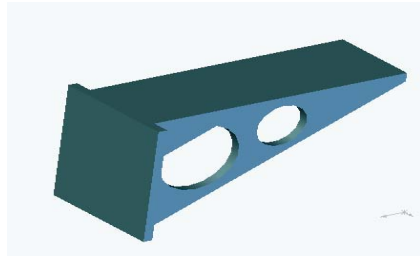


Figure 2-35. New bracket with thicker faceplate, horizontal gussets and lightweighting holes.

These changes improved the bracket's performance considerably. The motion of the first natural frequency now shows significant deformation in the slide and motor coil (Figure 2-36), indicating the bracket is sufficiently stiff.

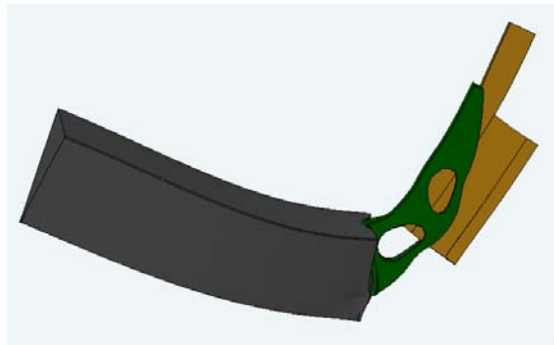


Figure 2-36. First bending mode with new bracket. Deformation now occurs in the slide and motor coil, indicating a sufficiently stiff bracket.

Table 2-8 compares the first two natural frequencies of the structure for the two bracket designs. The natural frequency of the system undergoes a large jump with the new bracket. This is especially true for the vertical bending natural frequency, since the added height of the bracket greatly increases the moment of inertia, and vertical stiffness (the moment of inertia is proportional to the height cubed). Also, it should be noted that the mode of lowest natural frequency changes from vertical bending to horizontal bending

for the new bracket. This is mainly due to the increased vertical stiffness of the bracket. Horizontal gussets will be added to the top to help with the horizontal stiffness.

	Vertical bending Nat.Freq.	Horizontal bending Nat. Freq.
Original bracket	804	866
New bracket	1509	1059

Table 2-8. Natural frequencies of the system for the two bracket designs.

2.7.2 Magnet Track Relief

Another important part of the bracket is the moment arm of the motor coil weight. The further the motor is offset from the back of the slide, the larger the moment created by the motor's weight. A large moment will result in an unwanted pitching force on the slide that could negatively affect the system's performance. To reduce the offset, a new configuration was designed with a cutout section at the back of the slide. This area of relief for the magnet track would enable the motor to be placed in almost direct contact with the back of the slide, reducing the moment arm considerably.

A new rear plate (Figure 2-37) with a cutout for the magnet track and threaded holes for the bracket screws was mated to the cutout section at the back of the slide and glued in place.

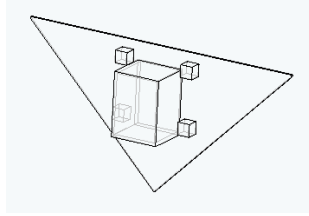


Figure 2-37. 3D drawing of the new rear faceplate of the slide. This view is from inside the slide looking toward the back. A relief (the large box) is provided for the magnet track, and the four small squares are used to hold the bracket screws.

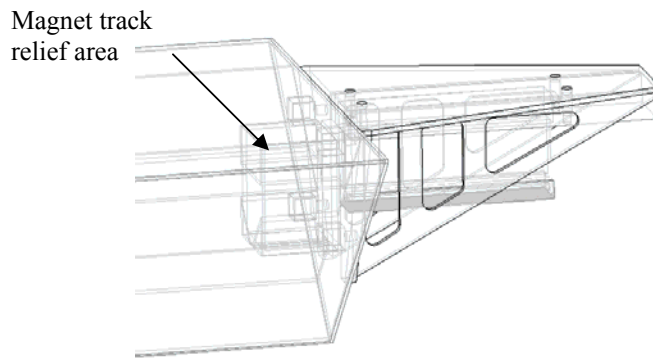


Figure 2-38. Slide-bracket-motor assembly. The magnet track forms a channel around the bottom of the motor I-coil and extends into box-shaped relief area in the slide.

Part of the front plate of the bracket was removed to allow space for the magnet track. The final bracket design and the slide-bracket-motor assembly are shown in Figures 2-38 and 2-39, respectively. Further details of this analysis are provided in Appendix F.

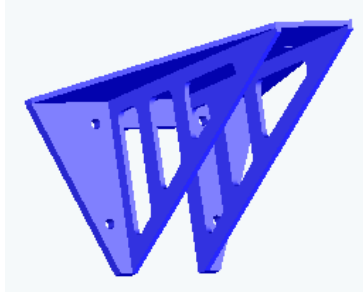


Figure 2-39. Final bracket design.

2.8 Air Bearing

The triangular slide is supported by a base assembly and a top as shown in Figure 2-40. The base assembly is composed of a v-block with an innovative air bearing design and fabrication procedure, developed at Precitech in Keene, NH.

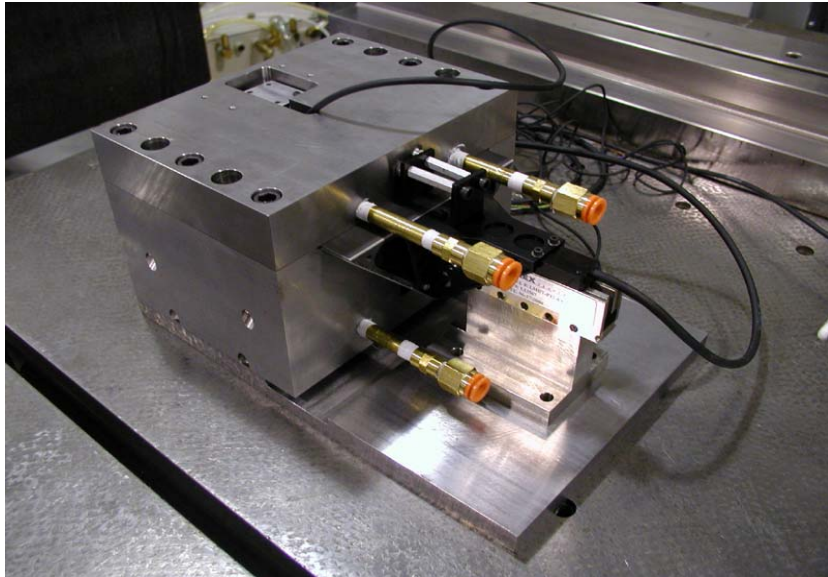


Figure 2-40. Photograph of LAT system. The slide and air bearing housing are shown.

The air bearing assembly includes eight replaceable brass orifices and external pneumatic fittings (see Figure 2-40) that permit adjustment of the dynamic stiffness. The bearings in the base assembly were optimized for stiffness and damping in the frequency range of the first dominant vibration mode (horizontal bending around 1000 Hz as described in

Section 2.4). The bearing surface is precision ground to provide precise air film gaps. The air bearing in the top was not as stiff as the lower bearings but was designed primarily to provide a preload. This greatly relieves the manufacturing tolerances. All surfaces were lapped to improved flatness and finish and the final straightness on average was less than 0.0001" (2.5 μm) and the finish was 20 μin or 0.5 μm .

Stiffness measurements were taken with the base sitting on a granite plate and a steel bridge built from steel used to support a 10 lb test weight as shown in Figure 2-41. The slide was protruding approximately 0.60" from each end of the base/top plate. Precision ground risers were placed on each end of the slide to form the test bridge assembly and 80 psi air was applied. The 10 lb test weight was placed in the center of the bridge, and the electronic indicator was positioned on the end of the slide. The indicator showed 5-7 μin of deflection, or a stiffness of 1.67 million lb/in, slightly higher than the 1.3 million lb/in used to calculate the bearing natural frequency in Section 2.4. This value represents the overall stiffness of the bearing. Then, the test weight was moved from the central position on the test bridge to the end of the test bridge, directly over the indicator. Now the indicator showed 30-35 μin of deflection – a stiffness of 300,000 lb/in. This is the stiffness in the vertical tool tip direction. For this test, the magnetic base supporting the electronic indicator was positioned on the top plate to minimize deflection in the measurement loop.

The air flow to the slide was measured.

- Flow measurements on the base with 80 psi applied was 94 liter/min.

- Flow measurements on the top plate with 80 psi applied was 96 liter/min.

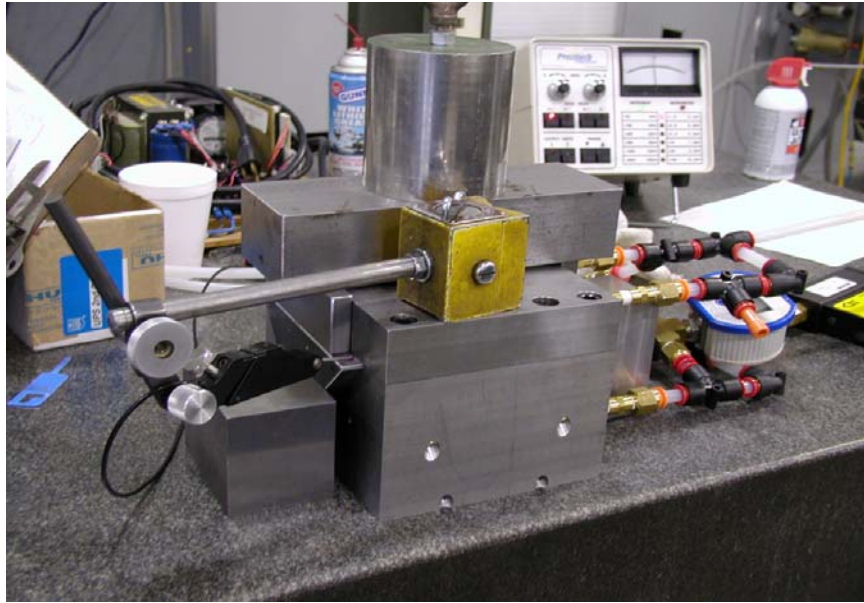


Figure 2-41. Setup for air bearing stiffness measurements.

2.9 Additional Design Considerations

2.9.1 Linear Encoder

The Renishaw RGH24B linear encoder provides position feedback to the UMAC controller for position control and to the amplifier for commutation. The encoder scale is in the form of a steel tape that is attached to the top of the slide via an adhesive backing. The readhead is rigidly attached to the housing of the bearing (Figure 2-42). The encoder signal is a pair of one 1 V peak to peak sine waves that are 90 degrees out of phase with a period of 20 μm . The output signal is interpolated by the UMAC controller into 4096 counts per period, giving a theoretical resolution of 5 nm. Unfortunately, a noise level of approximately 5 mV on the sine wave signals limits accuracy of the position sensor to about 100 nm.

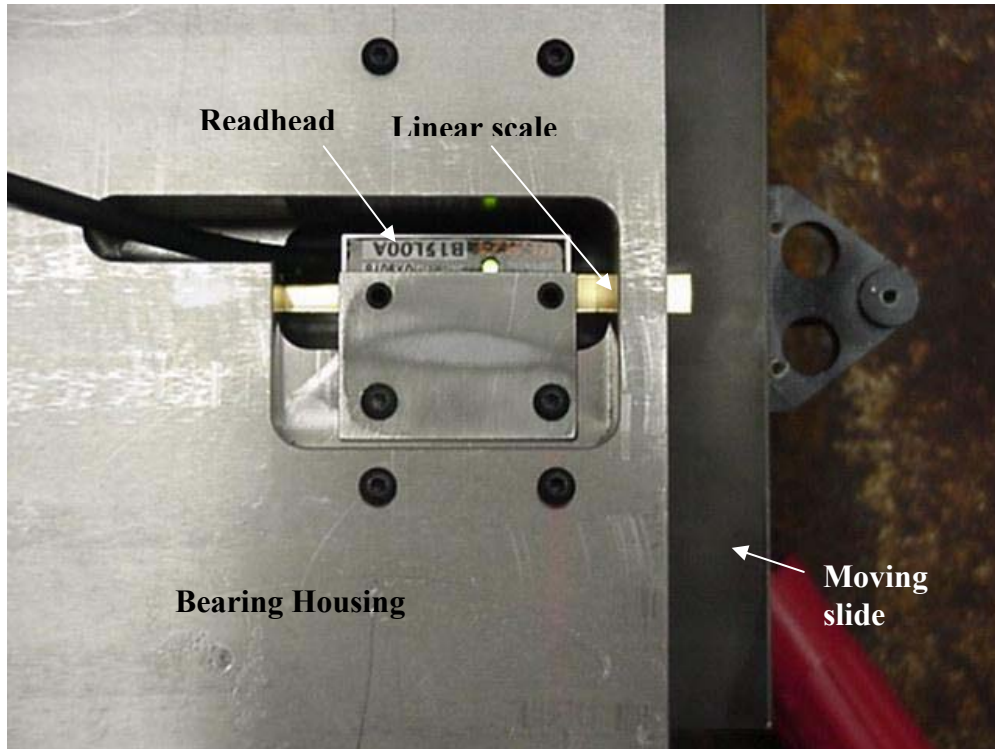


Figure 2-42. Renishaw RGH24B linear encoder with scale.

2.9.2 Tool Holder

Precitech designed the lightweight tool holder pictured in Figure 2-43 attached to the front of the triangular slide. The diamond tool is mounted on a trapezoidal shank (standard commercial tool) that is bolted to the tool holder. The tool is in line with the linear encoder that is attached to the slide so there is no Abbe offset in the position measurement.



Figure 2-43. Tool holder mounted to the front of the triangular slide.

2.9.3 Vertical Tool Adjustment

The LAT system layout on the Nanoform 600 diamond turning machine is shown in Figure 2-44. The feed direction is x and the LAT axis motion direction is z (into the part). The square box with a knob shown in the figure is the micro-height adjuster, which allows the tool 200 μm of vertical deflection (the y direction) needed for tool centering. To allow the system to bend under small loads from the micro-height adjuster, a flexure plate was designed to which the LAT bearing housing and magnet track were attached (the notched rectangular plate in Figure 2-44). Two cylindrical washers were machined and inserted directly under the flexure plate to facilitate bending.

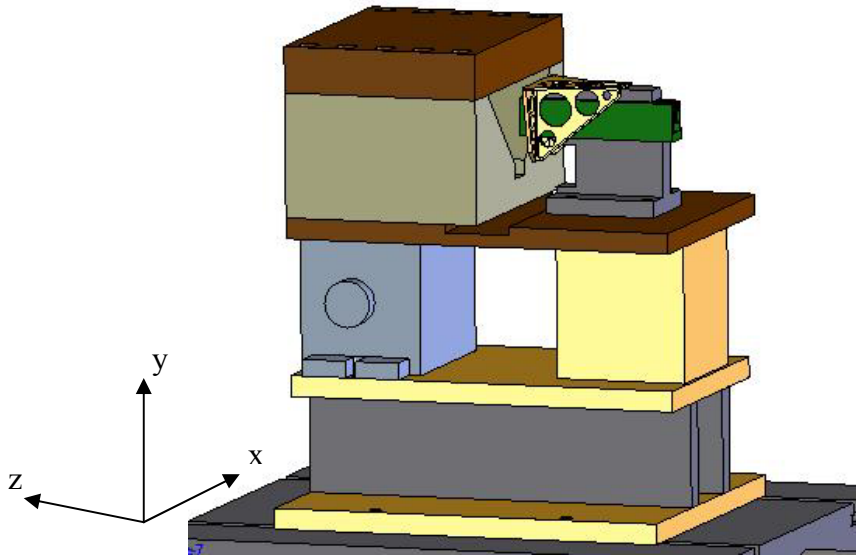


Figure 2-44. Flexure plate layout on the Nanoform. The box with the knob directly under the slide housing is the micro height adjuster. The notched plate directly above the micro height adjuster is the flexure plate.

SolidWorks COSMOS FEA package was used to analyze the plate's deflection. The plate was designed to have a stiffness of $5 \text{ N}/\mu\text{m}$ at the point of contact of the micro height adjuster, with a maximum deflection of $300 \mu\text{m}$ under the estimated maximum possible load – 1500 N (see Appendix G for calculation details). Simulations were run to confirm the analytical calculations. A drawing of the plate's natural and deflected positions is shown in Figure 2-45. This figure shows the bending motion of the plate.

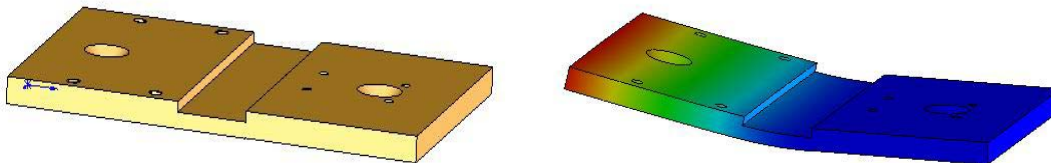


Figure 2-45. Model of the flexure plate in its natural (left) and deflected (right) positions.

2.10 Dynamic Testing

One major concern in attaching the LAT system to the Z-axis of the Nanoform 600 DTM was the effect it would have on the Z-axis motion. Initial estimates showed that, given the design parameters, the impact on the DTM's Z-axis would not be significant due to the axis's high stiffness and the relatively small moving mass of the LAT axis. The stiffness of the Nanoform Z-slide is 60 N/ μm . The displacement of the Z-axis with the LAT moving +/- 2 mm at 20 Hz would be about 350 nm. If this displacement only occurred at the excitation frequency of the LAT motion, the result would be a small reduction in the amplitude of the servo motion (~0.02%). However, the LAT motion excites the Z-slide at its natural frequency of about 110 Hz as well. Figure 2-46 shows the motion of the Z-slide during operation of the LAT axis. The relative motion of the Z-slide is +/- 197 nm at 110 Hz (the high frequency in wave in the figure) and +/- 205 nm at 20 Hz. While the 20 Hz Z-slide motion will only slightly reduce the amplitude of the LAT, the 100 Hz motion will have a deleterious effect on the surface finish and some remedy must be developed to reduce this effect. Several ideas including counter-balance masses and tuned dampers will be examined in a later phase of the project.

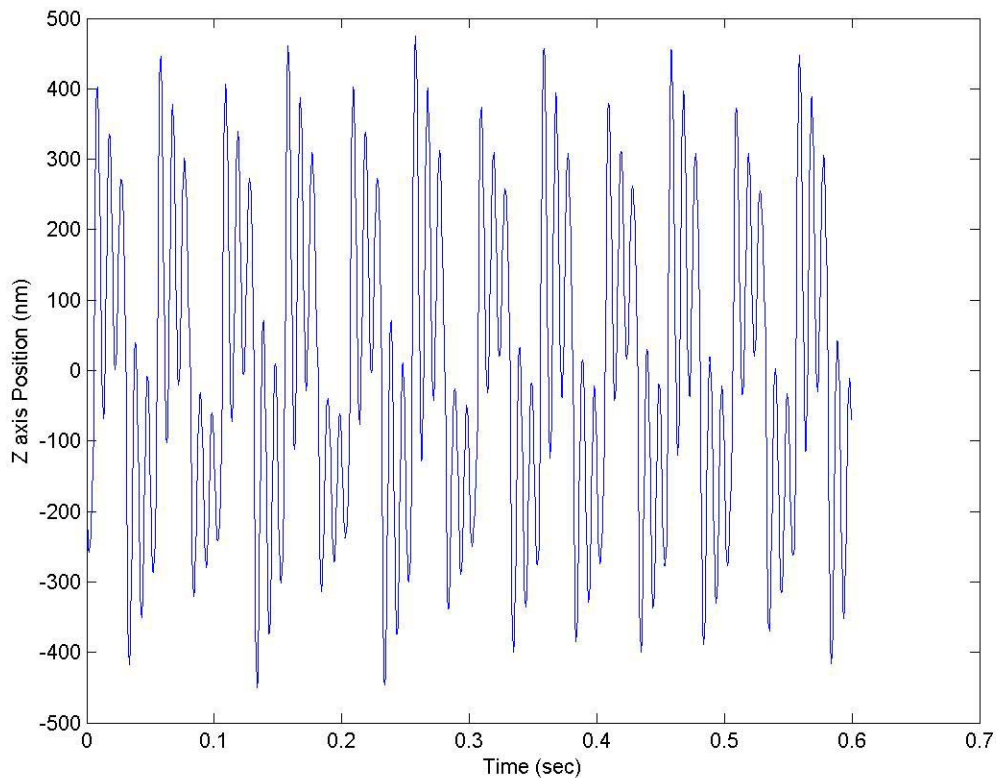


Figure 2-46. Z-axis motion during LAT operation at +/- 2mm, 20 Hz.

2.11 Design Summary

The final actuator design is based on a 7" long triangular slide made of aluminum honeycomb (Figure 2-47). The slide is driven by an Airex P12-1 linear motor. The motor is attached to the slide by a bracket that features horizontal and vertical gussets 1/16" thick and a 1/8" thick faceplate. The bracket also includes lightweighting holes. At the rear of the slide is a relieved area for the magnet track. This reduces the moment arm created by the motor coil while still allowing the one-inch stroke. The entire slide is

supported by stiff air bearings on its two bottom faces (90° from each other). Another, less-stiff air bearing is used on the top face as a preload.

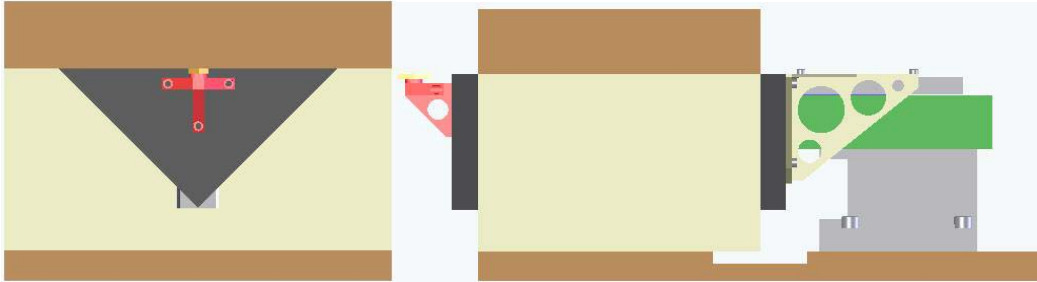


Figure 2-47. Final design drawings for the LAT system. Front and side view shown.

3 LAT System Characterization

After fabrication was complete, the next step was to operate the LAT and characterize its behavior so a motion controller could be designed and implemented.

3.1 Description of Experimental Apparatus

Setting up the LAT system involved creating wiring schemes to integrate the slide on the diamond turning machine. Also, the motor amplifier had to be configured and a commutation scheme established. Finally, the UMAC controller on the diamond turning machine was configured to drive the motor.

3.1.1 System Components

A general layout of the uncontrolled system is shown in Figure 3-1, and each of the major components is described.

Host PC - A host PC is the front/user end of LAT system. It executes the user interface for the Delta Tau UMAC controller (PWIN Pro) and the software for the Elmo Cello amplifier (Elmo Composer) that drives the linear motor. The PC is used to configure the amp and to give any commands to the motor (through the UMAC and amplifier, shown in Figure 3-1, Figure 3-2). It was also used to collect and display much of the motion data from the slide via the linear encoder and to tune the controller for the closed loop system.

Delta Tau UMAC Turbo Controller – The UMAC controller stores motion program commands from the PC and converts them to voltages that are sent to the motor amplifier (Figure 3-1). Sent through a USB cable, these commands come in the form of quick

changes (bias value) or motion programs, which load onto the UMAC's main board and run at appropriate times. The UMAC is also responsible for reading the linear encoder signal from the slide.

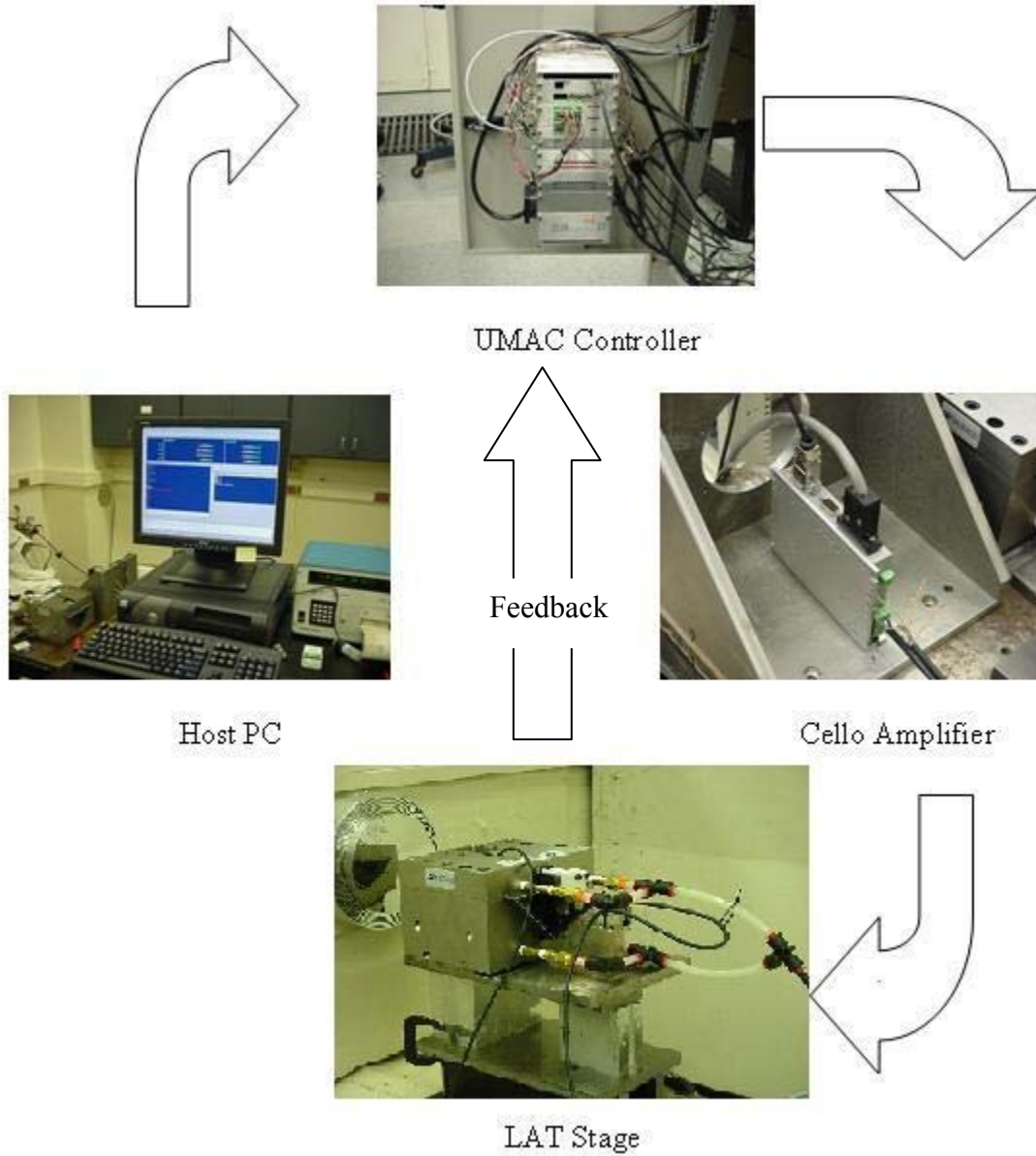


Figure 3-1. Main component layout of the LAT system. The arrows show the direction of command.

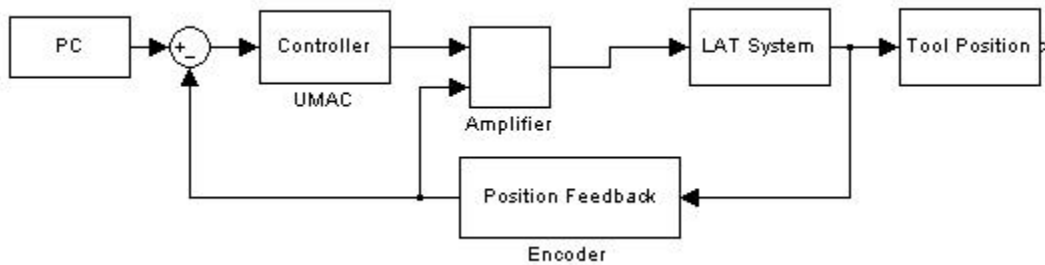


Figure 3-2. Block diagram of the entire system. The signal from the PC is compared to the current tool position, then sent to the UMAC. It is acted on by the controller and sent to the amplifier, which commutates the system based on the position feedback.

4096 Interpolator card – Accessory 51E. This accessory is a sine wave input interpolator designed to integrate up to four analog quadrature encoders to the UMAC system. It reads a sine wave voltage from the LAT encoder (Section 2.9.1) and converts it to a position based on the amplitude and phase of the wave. This position is then used as feedback for the controller. This card was used because, at the desired speeds of this application, an external analog interpolator could not convert the analog signal to a quadrature signal fast enough to provide the high resolution necessary for the LAT’s positioning requirements.

Elmo Motion Control Cello 3/100I Motor Amplifier – The Elmo Cello is a pulse width modulation (PWM) motor amplifier with a switching frequency of 22 KHz. It takes a voltage command based on the error amplitude from the control algorithm in the UMAC and converts it to a scaled current sent to the motor. This particular amplifier has a current maximum of nine Amps. The amplifier also controls the motor commutation. It sends the commanded current to the motor in three phases 120° apart (Appendix C) and

drives the motor. To do this, the amplifier needs to know the location of the slide, so the encoder signal was split and runs into the amplifier as well as the UMAC interpolator, as shown in Figure 3-2.

LAT Stage – The current from the amplifier goes directly to the motor coil in three phases. The magnetic field of the permanent magnets in the track acts on the current in the coil and creates a force, driving the motor. With the motor mount bracket acting as a rigid coupling, the slide moves along the air bearing surfaces, and its position is measured by the linear encoder.

3.1.2 Amplifier Configuration

As mentioned in the previous section, the linear motor amplifier was used to convert voltage commands to three-phase current commands needed to drive the motor. Several steps had to be taken to configure the amplifier. The process is described in Appendix H, where all values are taken from the manufacturer's specifications [14].

3.1.3 UMAC Configuration

To determine the dynamics of the LAT, it was necessary to run it in open-loop mode. Although the UMAC does not technically allow motion programs to run in open-loop mode, this problem was circumnavigated. Each motor controlled by the UMAC has a bias value that is simply a voltage offset for that motor. This bias value is controlled by variable Ix29, where x represents the motor number in the system (Motor 2 in this

application). Using this variable, it was possible to apply a varying voltage to the LAT input without specifying a closed-loop command. This technique is explained in more detail with the actual code in Appendix I.

3.1.4 Cooling Issues

Heating is a concern in linear motor systems due to constant current flowing through the coils to hold position of the slide. To dissipate this heat and keep the motor below its critical temperature, air and fluid cooling systems are often used [15]. Temperature measurements were taken on the LAT motor to see if this step would be necessary.

The motor is equipped with a built-in negative temperature coefficient (NTC) thermistor. Thermistors use certain metal oxides whose resistance changes with temperature [16]. A NTC is one in which the resistance decreases with an increase in temperature (for a positive temperature coefficient thermistor, resistance increase with increasing temperature).

To find the temperature in the motor, the thermistor resistance was measured and the manufacturer's specifications (Appendix J) were used to calculate the temperature. The motor followed a sine wave of 2 mm at 20 Hz (harshest operating conditions) for five minutes.

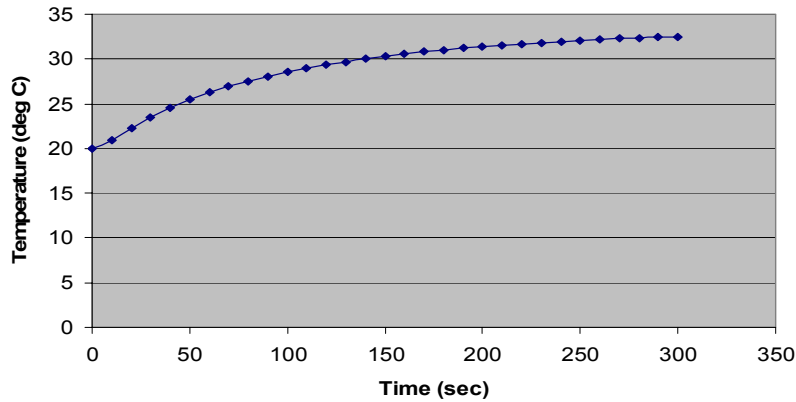


Figure 3-3. Plot of motor temperature versus time.

Figure 3-3 shows the motor temperature is asymptotic to 33° C, a value much lower than the motor’s critical safe temperature of 125 C, making an additional cooling system unnecessary for this application. Possible reasons the temperature stays low are the natural convection due to motion and the forced convection due to the air bearings dissipating much heat from the system. Additionally, local thermal deformation will have no effect on tool position because the encoder is located at the front of the slide, away from the motor. Further detail of temperature analysis is shown in Appendix K.

3.2 System Characterization

A system model was created and later verified through a series of open loop response tests. After studying the system, physical damping was added to improve the performance. The rationale for this added damping is explained and the experimental methods used to find the transfer functions are described in the following sections.

3.2.1 Undamped System Model

A free-body diagram was used to obtain the system model. The drawing is shown in Figure 3-4. The components of the moving mass (slide, bracket, motor and motor cable) were combined into one lump mass. Since there is no damping or restoring force (stiffness) involved with the motion, the only consideration is an inertial load due to the system mass. The system's response in the x direction to an arbitrary force input, U, was considered.

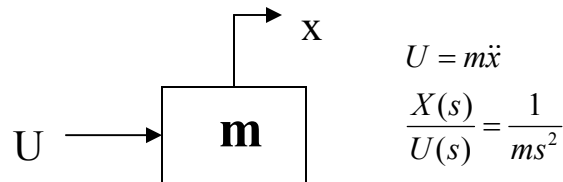


Figure 3-4. Free-body diagram of the undamped LAT system

The equation of motion for the system comes directly from Newton's Second Law. Then the Laplace transform was taken, and the transfer function, $X(s)/U(s)$ in Figure 3-4, was developed. This expression gives the ratio of the system's response X (distance), to a given input U (force). The result is a double integrator represented by the s^2 in the denominator of the transfer function. The mass (m) is found by weighing the moving parts of the system. The mass of each component and the total moving mass are shown in Table 3-1.

COMPONENT	MASS (g)
Slide with tool holder	517
Motor mount bracket	38
Motor	100
Motor cable	10
TOTAL	665

Table 3-1. Mass of LAT system's moving parts.

The system model will also have a gain in the numerator. This is the scaling necessary to change Volts (Input) to mm (Output). The scale factors are 0.3 Amps/Volt (the amplifier scalar), 8.4 N/Amp (the Motor Constant, provided by the manufacturer) and 1000 mm/m (the output of the Transfer Function is meters). The full block diagram is pictured in Figure 3-5, and the frequency response (Bode plots) is shown in Figure 3-6. As expected, the magnitude of the system drops off at the rate of 40 dB/decade (20 dB/decade for each integrator) and is constantly 180° out of phase (relationship between acceleration/force and position).

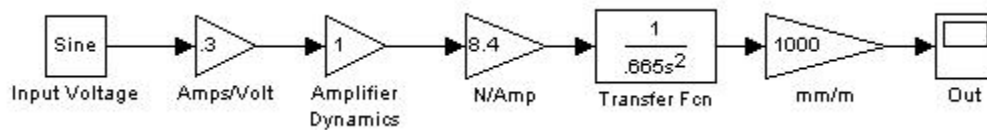


Figure 3-5. Open-loop block diagram of the undamped system.

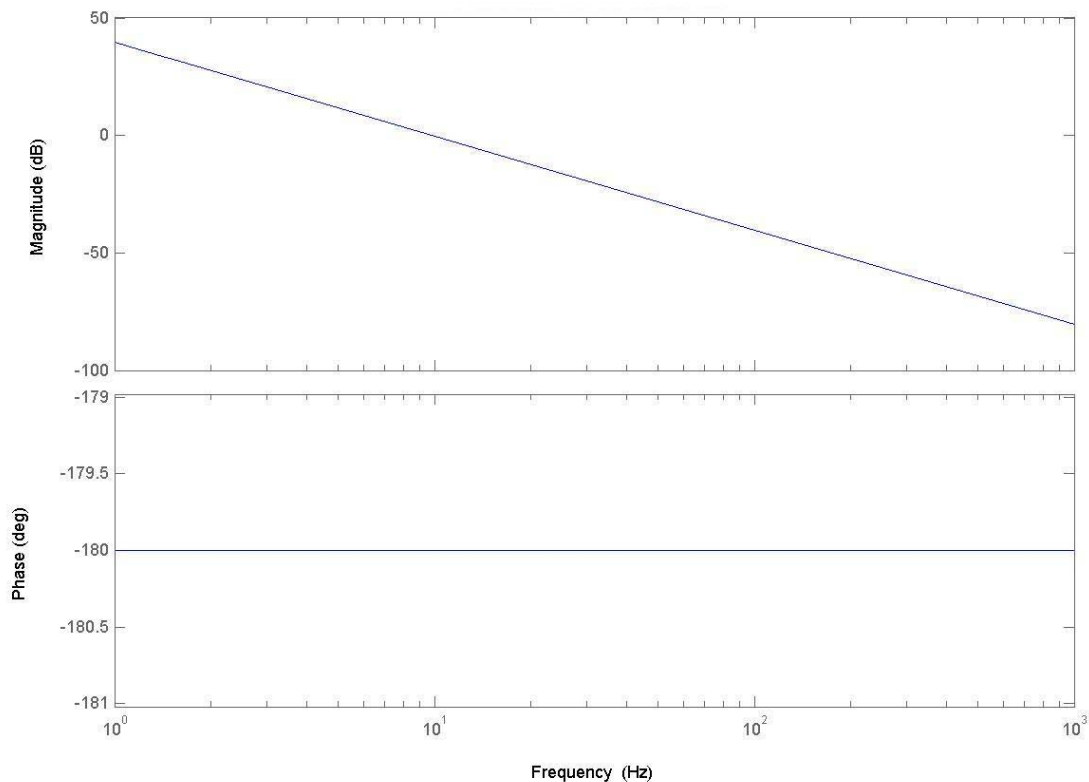


Figure 3-6. Theoretical open-loop Bode plots of the undamped system.

Amplifier Dynamics Because the dynamics of the amplifier were assumed to be much faster than those of the motor, it was modeled as a unity gain in the system’s block diagram in Figure 3-5. To verify this assumption, a current input command was sent to the amplifier in closed-loop mode, and the current output was recorded with the amplifier software tools. Since a manual tuning feature was not available during the amplifier setup, the controller gains were obtained through the amplifier software’s auto-tune process. The amplifier’s response to a step command is shown in Figure 3-7.

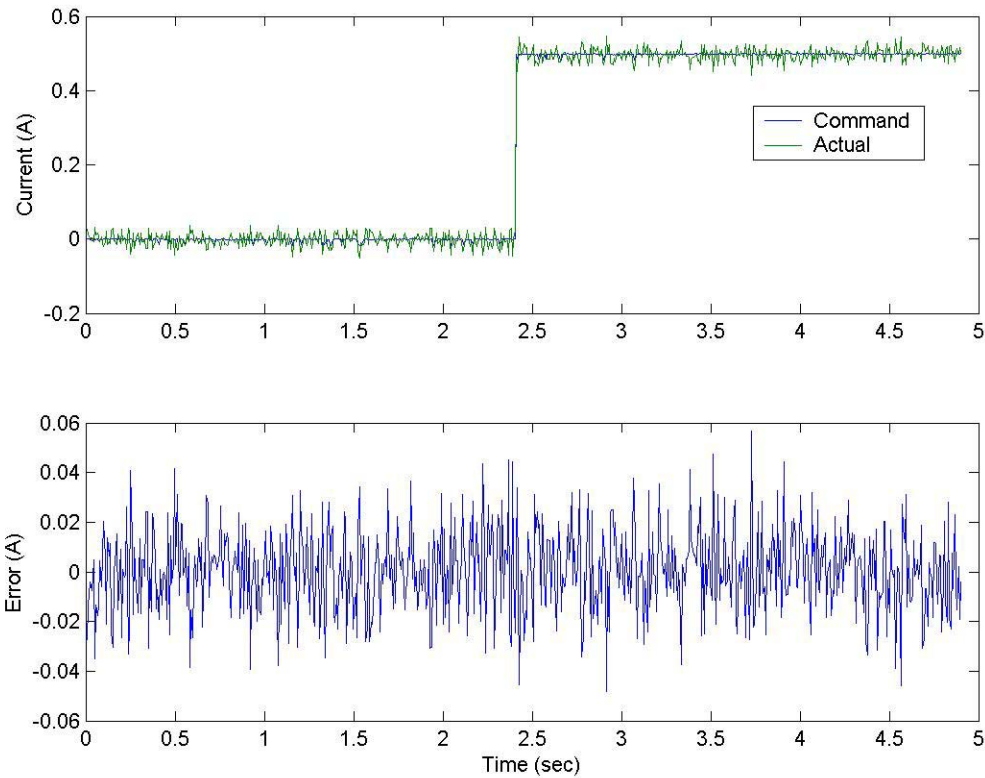
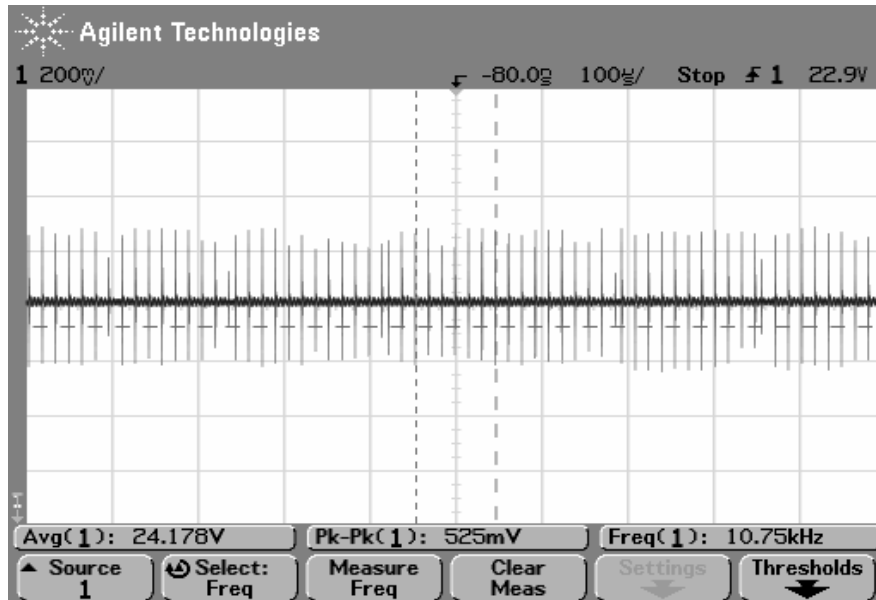


Figure 3-7. Amplifier response to a closed-loop step command.

The plot shows a PV current error of roughly 0.08 Amps and an RMS value of 0.0167 Amps. This corresponds to a peak force of 0.67 N (0.14 N RMS). Although the PV value of the current error was reduced to approximately 0.06 Amps by changing the current loop controller gains in the amplifier software, it will still have a deleterious effect on the surface.

The source of this noise was found to be the amplifier's 24 V power source. Figure 3-7 shows the source on an oscilloscope screen. A 525 mV peak-to-valley variation occurs at 10.75 KHz. This variation in voltage corresponds to a PV error of around 100 nm.

However, this problem was not noticed until after machining and had an adverse effect on surface finish.



3.2.2 Open Loop System Verification

Open loop frequency tests were used to verify the system model described in Section 3.2.1. Using the bias value associated with Motor 2 on the UMAC, sine waves of constant amplitude and varying frequency were sent into the system. The inputs (in Volts) and the system's response to these inputs (in mm) were captured with the PEWIN Plotting tool.

The input and output data was changed to the frequency domain using Fast Fourier Transform (FFT). The magnitudes of the vectors are compared at finite frequencies to get points on the magnitude Bode plot (the y-axis is $20\log\left(\frac{\text{output}}{\text{input}}\right)$). Similarly, the

difference in phase gives the values of the phase Bode plot. The system's response to input frequencies of up to 1000 Hz is shown in Figure 3-8 and is compared to the theoretical transfer function associated with the system model.

The experimental results show the actual system behavior is very close to the model, although the magnitude ratio of the actual system is lower. This indicates that the actual motor constant is lower than the published value used in the model. There are no noticeable mechanical resonances up to 1000 Hz, and the two sets of data have the same phase and both decay at the expected rate. Thus the model is a valid representation of the system and can be used to examine the effect of various control algorithms.

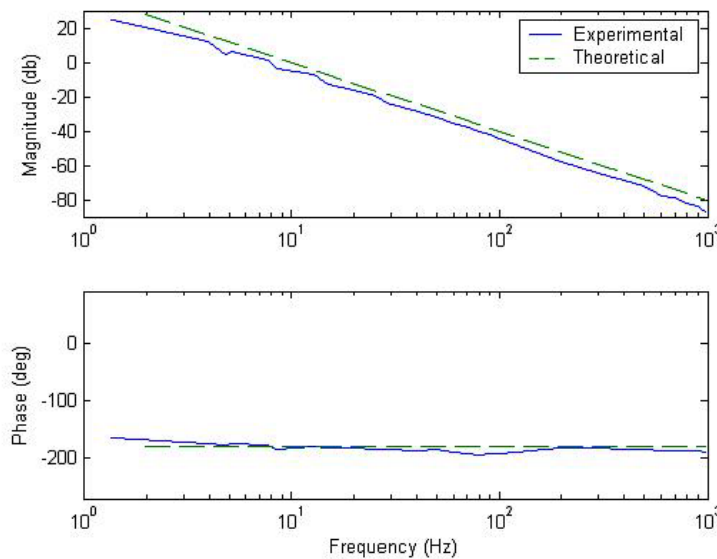


Figure 3-8. Experimental undamped transfer function compared with system model.

3.2.3 Damped System Model

Anticipating disturbance rejection problems, techniques for adding physical damping to the undamped LAT system were considered. Physical damping provides a force

proportional to the velocity of the slide that opposes its motion. The effect of this damping force is to decrease the system's settling time and maintain stability [17]. Another important reason to add physical damping is to improve the system's disturbance rejection.

The free-body diagram of the damped system is shown in Figure 3-9. It is the same as the undamped case except for the damping force ($b\dot{x}$), which always opposes the motion of the slide. This force is directly proportional to the velocity of the slide. A Root Locus plot shows how a system's closed loop poles change with changing gain. The root locus plots in Figure 3-10 show the closed-loop poles move from a marginally stable location (along the imaginary axis) to a stable location (the left-hand s plane) with the addition of damping. The plots show the values used to model the damped and undamped LAT system ($m = 0.665$, $b = 10$).

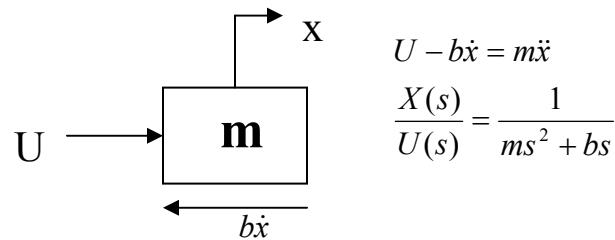
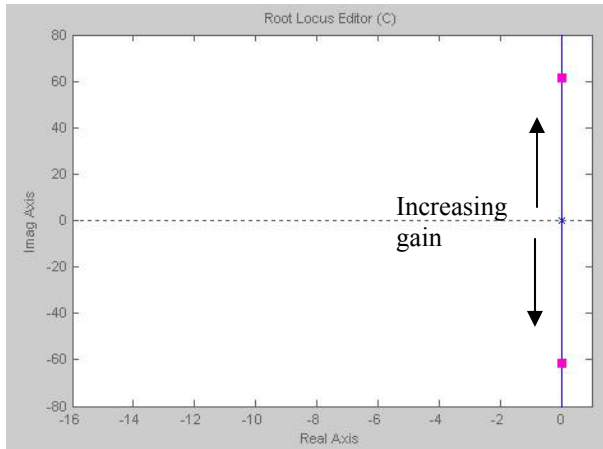
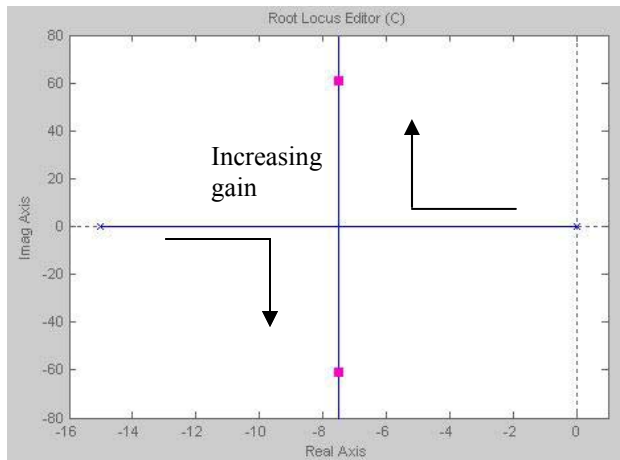


Figure 3-9. Free-body diagram of the damped system.



a.) Undamped System



b.) Damped system

Figure 3-10. Root Locus plot for the undamped (a) and damped (b) systems. The addition of the damping force pushes the closed loop poles into the left-hand plane, indicating a stable system.

(the imaginary axis) to a stable location (the left-hand s plane) with the addition of damping. The plots show the values used to model the damped and undamped LAT system ($m = 0.665$, $b = 10$).

The difference between a marginally stable system – the undamped case – and a stable one can best be observed by its response to a step input. The decay rate of the system is exponentially proportional to the real part of its closed loop poles. Therefore, systems with right hand poles (positive real parts) will exponentially increase and are unstable. Those with poles on the imaginary axis (real part equals zero) are marginally stable and will never decay or grow (undamped case), and systems with poles in the left hand plan (negative real parts) will decay. This phenomenon is displayed in Figure 3-11.

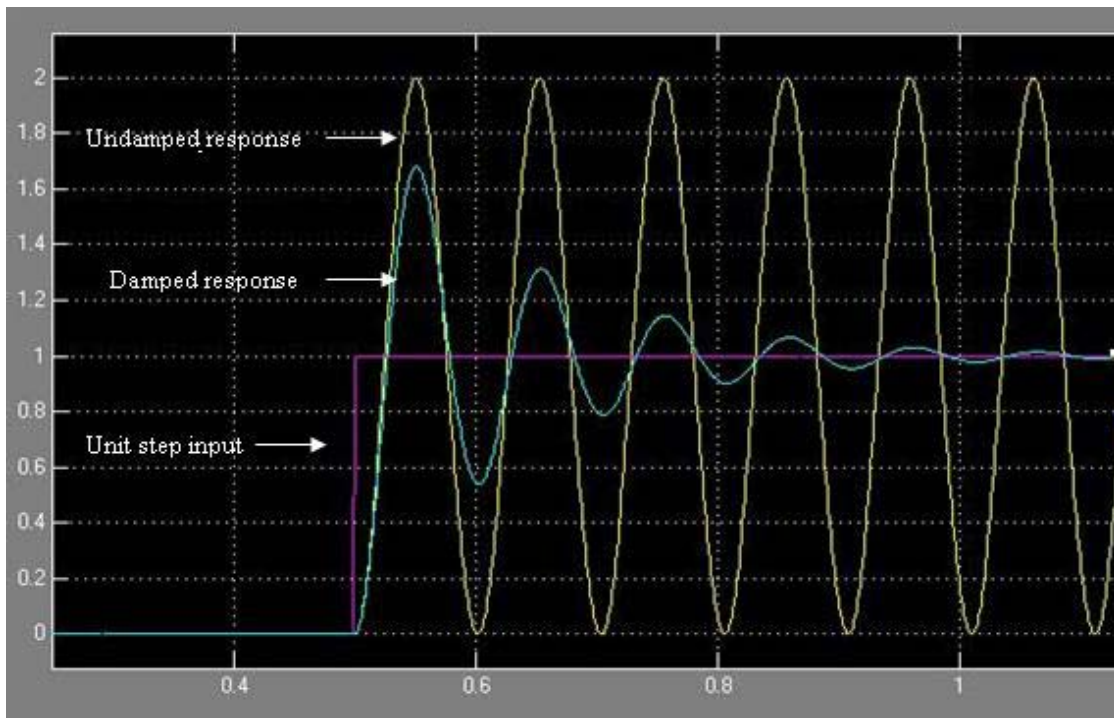


Figure 3-11. Step response of the damped and undamped system. While the damped system decays, the response of the undamped system maintains constant amplitude (marginally stable).

3.2.5 Damper Design and Verification

Several preliminary designs were built but they resulted in undesirable friction between moving parts. Friction is very difficult to model because the resistance force varies with the object's velocity. To ensure purely viscous damping (resistance a constant multiple of the velocity), the design in Figure 3-12 was used. The damper consists of two stationary "L" brackets of 0.8 mm thick aluminum that support a rubber O-ring. A rod is attached to the moving slide whose diameter is slightly smaller ($350\ \mu\text{m}$) than the O-ring.

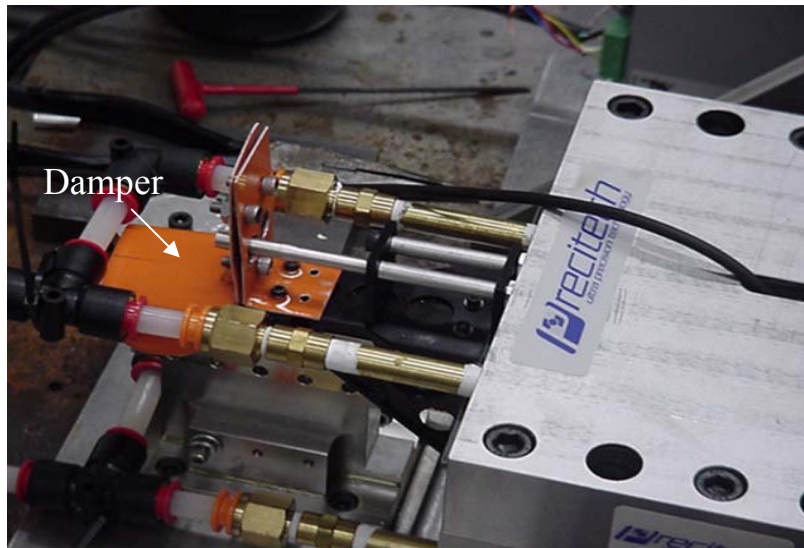


Figure 3-12. The damper for the LAT system. The rod shown slides through an O-ring sandwiched between the two brackets.

The clearance between the O-ring and the stationary rod is filled with gear oil (80W-90) to provide lubrication. Since there is no contact between the rod and the O-ring, little if any friction was present. The damping force was result of shear in the fluid and proportional to the fluid's viscosity and the shear rate. The damper was modeled as completely viscous so linear control analysis could be applied.

While the form of the damped system transfer function is known (Figure 3-9), the exact value of the damping coefficient, b , is not. To find this value, an analytical approach was used and later verified with experimental data. The model in Figure 3-13 was used to determine the force. The horizontal line at the bottom represents the outer diameter of the stationary rod, while the sloped and rounded line is the O-ring. The tangential force created due to the fluid (per unit velocity) is proportional to the viscosity of the fluid, the difference in the clearance between the center and the edge, and the relative slope between the surfaces.

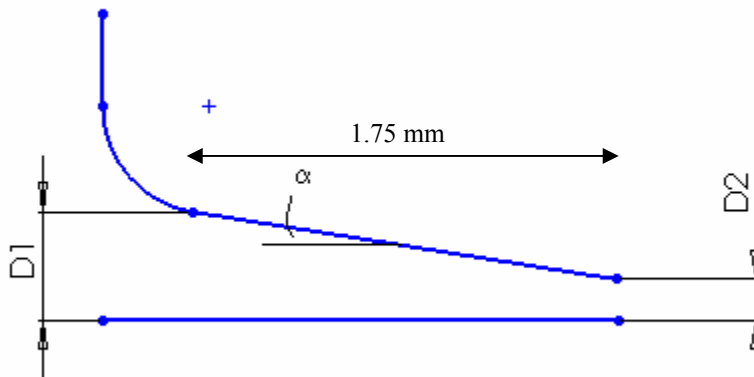


Figure 3-13. Diagram of rod (horizontal line) - O-ring (curved line) interface.

The force created by this fluid layer always opposes the motion and is given by Equation 3-3 [29].

$$\frac{F_t}{U} = \frac{2\mu}{\alpha} \left[3 \left(\frac{D_1 - D_2}{D_1 + D_2} \right) - 2 \ln \left(\frac{D_1}{D_2} \right) \right]$$

- F_t = tangential force (N)
 U = velocity (m/s) (3-3)
 μ = fluid viscosity (Pa-s)
 D_1 = center clearance (m)
 D_2 = edge clearance (m)
 α = angle between surfaces (rad)

The center clearance (D_2 in Figure 3-13) is one-half the difference in diameter of the rod and the O-ring, and the viscosity of 80W-90 gear oil at 20° C is 2.5 Pa-s [15]. However, the edge clearance (D_1 in Figure 3-13) was unknown and very difficult to measure because of the elastic deflection of the O-ring during operation. A range of probable values was used to determine the most likely damping forces. The angle between the surfaces was calculated using the two clearances and a parabola approximation. The full analysis is shown in Appendix L. A plot of viscous force vs. edge clearance is shown in Figure 3-14. It shows the damping force is in the range of 6-14 N-s/m based on the possible edge clearances.

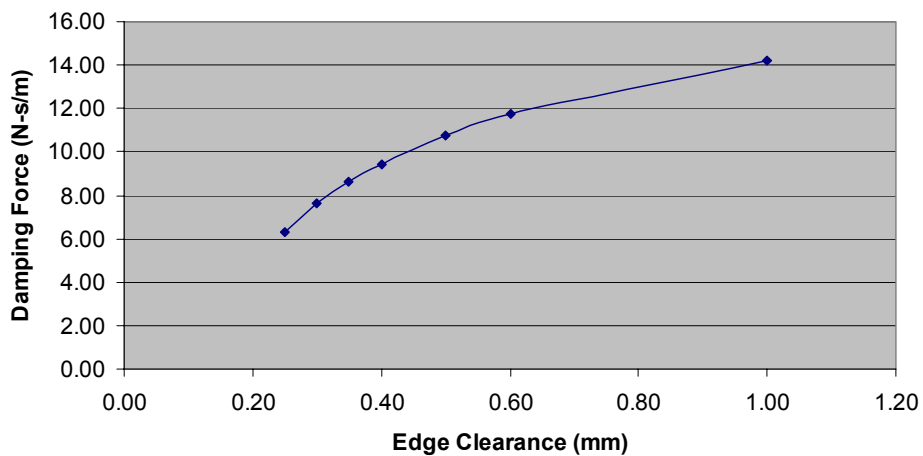


Figure 3-14. Viscous Damping Force vs. Edge Clearance.

Open loop frequency response tests were used to measure the damping force and compare with the values shown in Figure 3-14. An amplifier gain of one was assumed and the tests were carried out using the procedure described in Section 3.2.2.

The effects of damping can be noticed in the open loop response shown in Figure 3-15. While the damped and undamped system responses are identical at high frequency (they can be seen beginning to converge in Figure 3-15), the ratio of the output to the input is considerably smaller for a damped system at low frequencies because the damping force is relatively large compared to the input force. As the damping force increases, the output to input ratio decreases and the frequency at which the damped and undamped system response begins to look alike increases. Physical damping also reduces the phase lag at low frequencies for the same reason it reduces amplitude. The larger the damping force, the greater the reduction in phase lag.

The theoretical open-loop responses were plotted for the anticipated range of damping values using Simulink. The experimental data was plotted on top of these theoretical curves to find a match. Figure 3-15 shows the comparison. The experimental data (“jagged” line) seems to line up well with the plot for a damping force of 10 Ns/m. With this value used as b , the damping coefficient, the damped system block diagram takes the form of Figure 3-16.

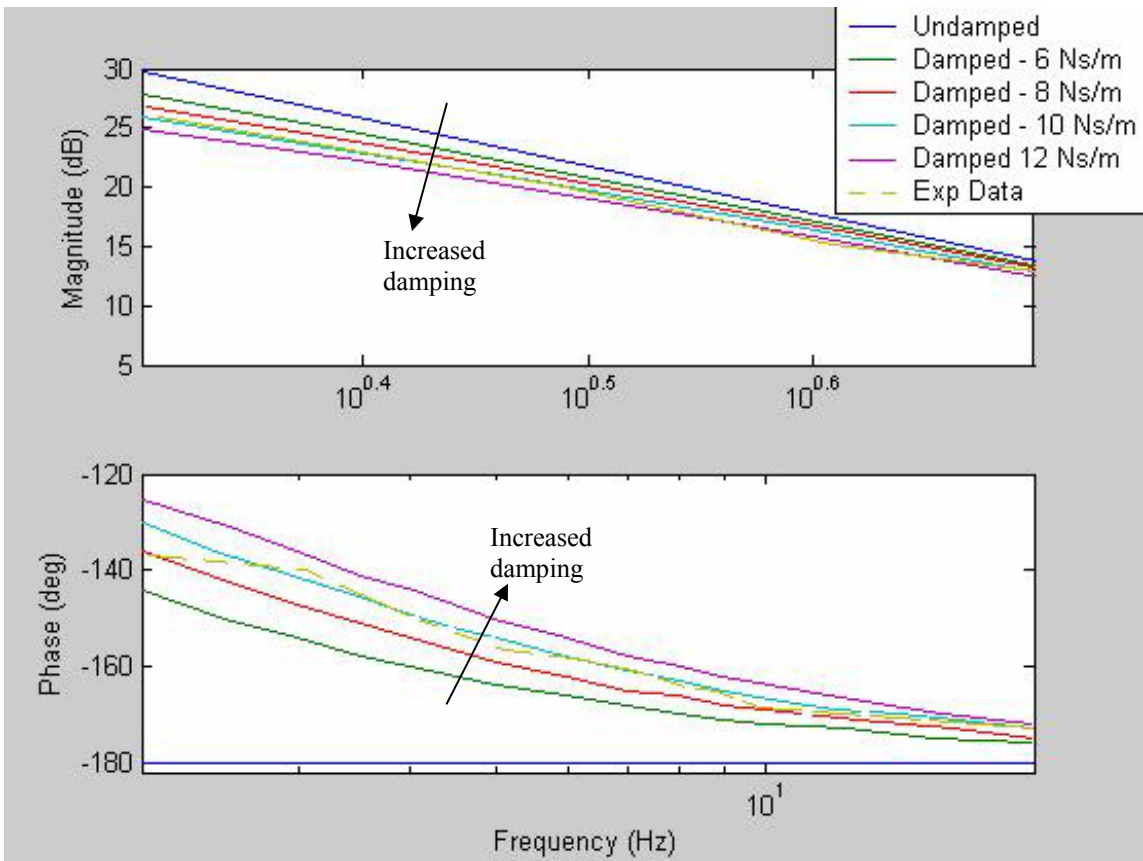


Figure 3-15. Bode Plots for varying systems with varying damping forces. The "jagged" dotted line is the experimental data.

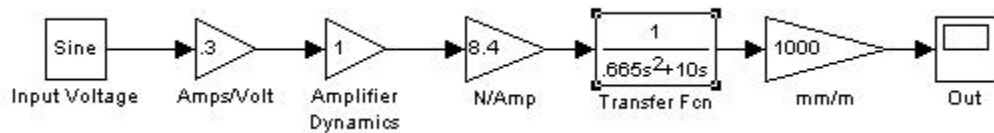


Figure 3-16. Open loop block diagram of the damped system.

4 Controller Design and Implementation

A linear motor depends on the control system to provide both static and dynamic stability. The following error, stiffness, disturbance rejection and stability depend on the motor torque, the moving mass, the feedback sensor, the controller algorithm and update time. The control system must be fast and flexible to deal with these issues and respond to the commands needed to create a freeform optical surface. The control scheme used in the LAT application is described in the following sections.

4.1 Controller Components

A Delta Tau Turbo UMAC was used as the controller in the LAT system. This controller consists of hardware and software components used to tune current loops, implement PID schemes and feedforward algorithms, calibrate DAC bias values, add filters to the system and capture command and motion data. The UMAC includes trajectory generation code to specify a tool path for the LAT axis that is updated at 2.3 KHz.

As shown in control layout in Figure 4-1, the UMAC controls the LAT axis as well as the other linear axes (X and Z) and the spindle of the Nanoform diamond turning machine. This setup, as opposed to one where a separate computer controls the LAT axis, was chosen to simplify the integration process and make use of the existing UMAC high resolution interpolator card to read the LAT axis encoder. Additionally, at the desired speeds of this application an external analog interpolater could not convert the analog signal to a quadrature signal fast enough to provide the high resolution necessary for the LAT's positioning requirements.

The signal from the LAT encoder is split and goes to the amplifier and the UMAC. The amplifier uses this signal for motor commutation, and the UMAC uses it for position feedback. The position is compared with the new commanded position, the controller makes appropriate modifications, and the UMAC sends a new force command to the motor through the amplifier. This cycle is repeated at 442 μ sec intervals.

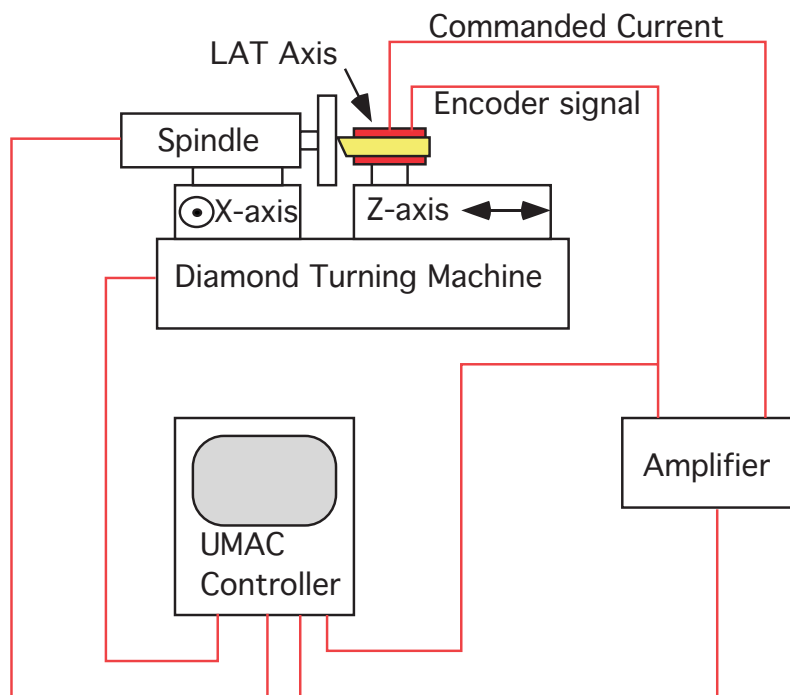


Figure 4-1. Control layout for the LAT system.

4.2 Role of Damping in the LAT System

To a degree, damping may be implemented in the control system with derivative control. However, when a derivative signal is created in the controller from the position data, the

presence of high frequency noise can often cause error around points of direction change due to rapid changes in the sign of the slope [17].

Another important reason to add physical damping to the system is its influence on disturbance rejection. While a controller with large gains and a fast update rate will add a sufficient amount of virtual damping to the closed loop transfer function, it cannot defend the system against a force disturbance that enters the plant after the controller as well as physical damping. These external disturbances may come in the form of electrical noise or forces from another source (i.e., machining forces). The effect of these forces on the systems response can be examined analytically (Equation 4-1) to show the usefulness of the real damping.

$$\frac{c_D}{D} = \frac{Ks}{ms^2 + bs + (K_d s^2 + K_p s + K_i)K} \quad (4-1)$$

In Equation 4-1, c_D/D is the ratio of the disturbance response to the disturbance input in a mass-damper system with PID control. K represents the system gain and K_d , K_p and K_i represent the controller derivative, proportional and integral gains, respectively. The larger the denominator of Equation 4-1, the smaller the relative disturbance response of the system. Holding the mass (m) and PID controller (terms in parentheses) constant, the effect of external damping can be observed by varying b . This term is zero for undamped systems, thus adding nothing to the system's robustness (the value of the denominator). For a damped system with finite b , the denominator is increased, thus reducing the effect of the disturbance. As the controller gains approach infinity and the sample time approaches zero, the physical damping becomes less and less influential. But in practical systems, these parameters are limited and a sample time of zero is certainly not the case,

meaning the physical damping will have a positive effect on disturbance rejection and lead to better surface finish, which will be illustrated in Section 4.3.

4.3 PID Control Scheme

The UMAC provides a position loop PID control scheme with velocity and acceleration feedforward loops. The UMAC PID servo equation as given by Delta Tau is shown in Equation 4-2.

$$DAC_n = 2^{-19} K_P \left[\left\{ S_P FE_n + \frac{K_{VFF} CV_n + K_{AFF} CA_n + K_I IE_n}{2^7} \right\} - \frac{K_D S_V AV_n}{2^7} \right] \quad (4-2)$$

- DAC_n is the output voltage in counts (16-bits) at servo cycle n
- S_P position scale factor
- S_V velocity scale factor
- K_P proportional loop gain
- K_D derivative gain
- K_{VFF} velocity feedforward gain
- K_I integral gain
- K_{AFF} acceleration feedforward gain
- FE_n following error in counts at servo cycle n
- CV_n commanded velocity at servo cycle n
- CA_n commanded acceleration at servo cycle n
- AV_n actual velocity at servo cycle n
- IE_n integrated following error

To better understand how each parameter affects the control, Delta Tau also provides a block diagram of the controller, shown in Figure 4-2. A few things should be noted about this diagram. First, the portion shown is only the control block (the plant is not shown). It takes two inputs, a reference position (command) and the actual position of the slide, and outputs a voltage to the motor. The controller provides a notch filter option (block directly after K_p - the proportional gain) to filter out specific frequencies and includes a

saturation (directly after the notch filter) to limit the voltage output of the controller. Secondly, while the integral gain (K_i) acts on the position error, the derivative gain (K_d) operates on the derivative of the actual position, not the error. Also, the proportional gain is implemented after a final summing block for all other gains. While this controller is not in the form of classical PID, it is a scheme often used in practical applications [26]. Finally, the acceleration and velocity feedforward gains (K_{aff} and K_{vff}), respectively, act on the input signal only, not on the position error. They have the effect of altering the command signal to account for future trajectories.

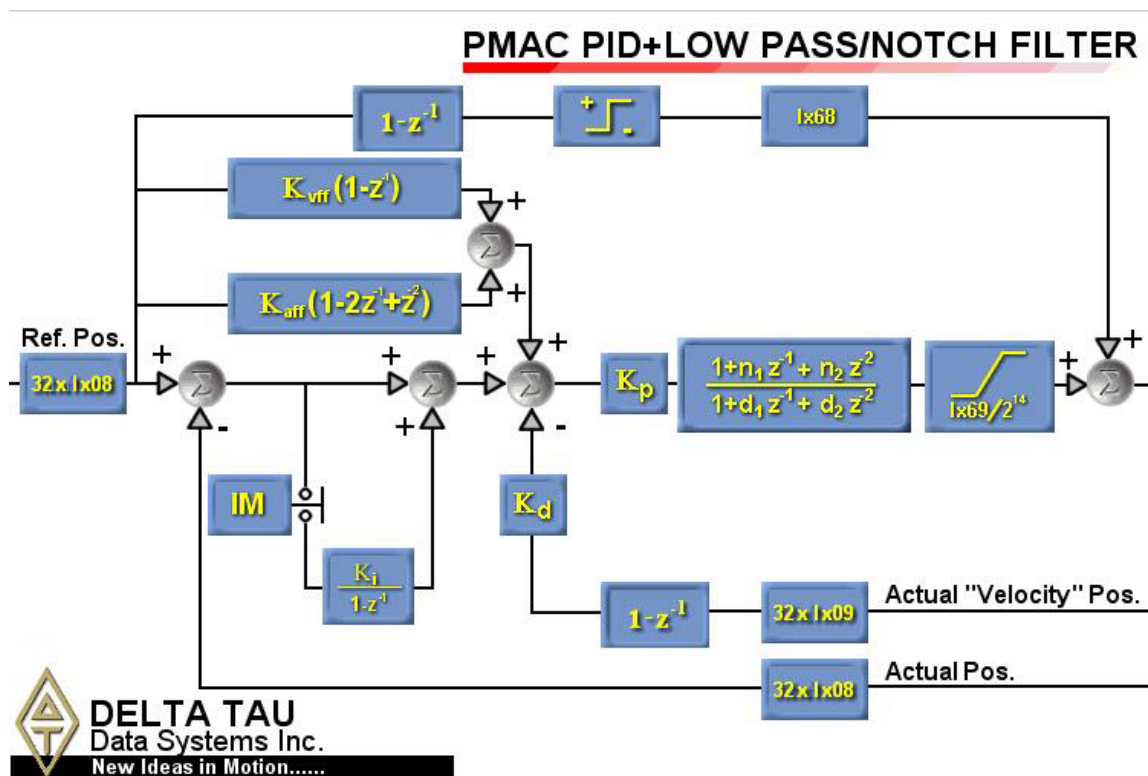


Figure 4-2. Block diagram of UMAC PID control scheme.

A block diagram of the entire system (motor, controller, and all gains) is shown in Figure 4-3. This Simulink model was created so the basic gains for the controller could be obtained without repeated testing on the system. These gains could then be implemented in the Delta Tau controller and fine tuned based on the actual system response. The block labeled “LAT System” contains the motor system (Figure 3-5) and the block labeled “Controller” contains a representation of the Delta Tau controller (Figure 4-2). The triangle shaped blocks are gains specific to the UMAC settings. This diagram is covered in detail in Appendix M.

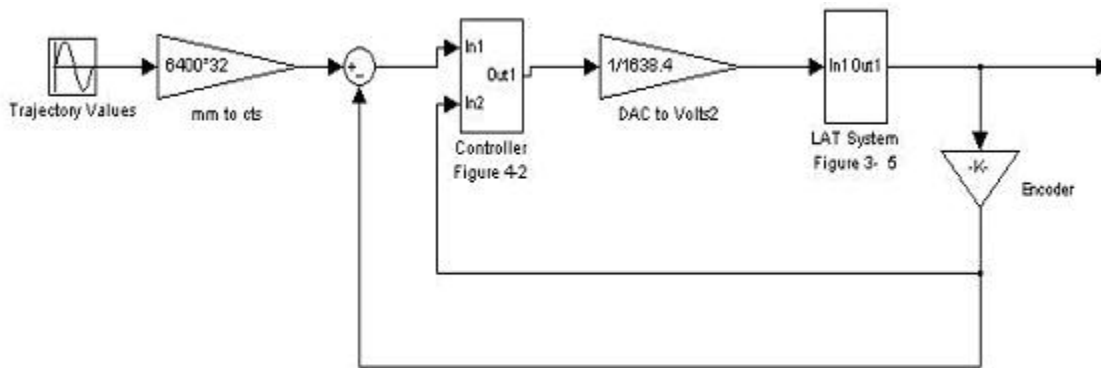


Figure 4-3. Simulink model of the controller and motor system

4.4 Controller Tuning

Gains for the controller were obtained through an iterative tuning procedure. For the damped and undamped case, suitable gains were found using the Simulink model described in the previous section. These gains were then implemented in the actual system. The following sections describe this process.

4.4.1 Simulink Model Tuning

As described in Section 4.3, a PID scheme with velocity and acceleration feedforward control was used on the PMAC controller. The Simulink model was designed with the same PID form but without feedforward control. A step input was used to tune the proportional, integral and derivative gains of the PID controller. Additionally, the step response could be optimized without the feedforward gains because they have no effect on the system during constant velocity commands (a step command specifies zero velocity at every cycle except the one during its “jump”). By knowing the effects of each type of gain in the PID controller, the step response could be formed to fit the needs of this application.

Generally, proportional control acts like a spring in the system [19], increasing its stiffness and natural frequency. Thus, it has the effect of decreasing the rise time of the system (making it respond faster) and decreasing, but not eliminating the steady-state error. However, it adds overshoot to the system. Integral control will eliminate the steady-state error but may increase the settling time of the system (the time for the system to get within 5% of its final commanded value). Derivative control increases stability and reduces the overshoot, but also increases the rise time, making the system more sluggish [19].

The goal is for the step response to have as small of a rise time as possible with reasonably small overshoot. Since the command is constantly changing, the steady-performance is not nearly as important as the transient characteristics.

Undamped System The Simulink model response of the undamped system to a $156\ \mu\text{m}$ step is shown in Figure 4-4. This distance corresponds to the largest step command the system will require during 20 Hz motion at 2 mm amplitude. The proportional gain was set as high as possible without making the system go unstable to make the rise time as small as possible. The proportional, integral and derivative gains of this particular system are 400,000, 10,000 and 805, respectively. This system exhibits a rise time (the time to reach 90% of the final steady state value) of 8 msec and no overshoot.

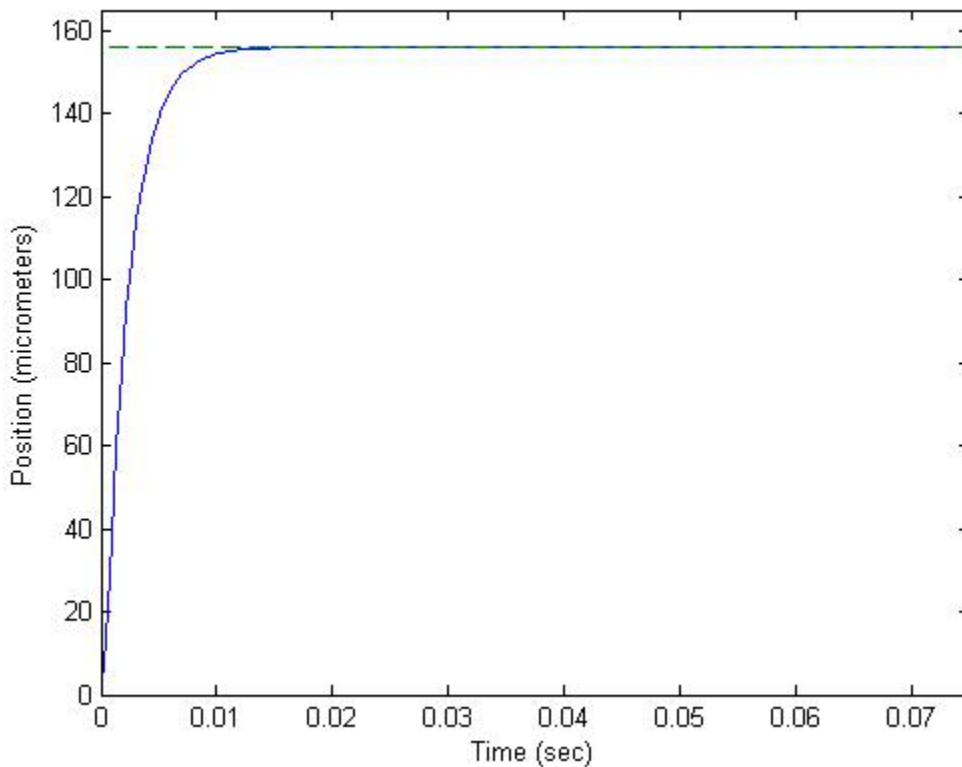


Figure 4-4. $156\ \mu\text{m}$ step response of the undamped Simulink model.

Damped System The tuning procedure used for the undamped system ($b=0$) was also used for the damped system ($b=10$). The step response of the undamped system for gain

values of 700,000 (KP), 400 (KD) and 10,000 (KI) is shown in Figure 4-5. This response has a rise of 4 msec (about half of that for the undamped system). Because of the added damping, the proportional gain may be increased without losing stability. This makes the damped system respond significantly faster than the undamped system. The damped system also exhibits no overshoot.

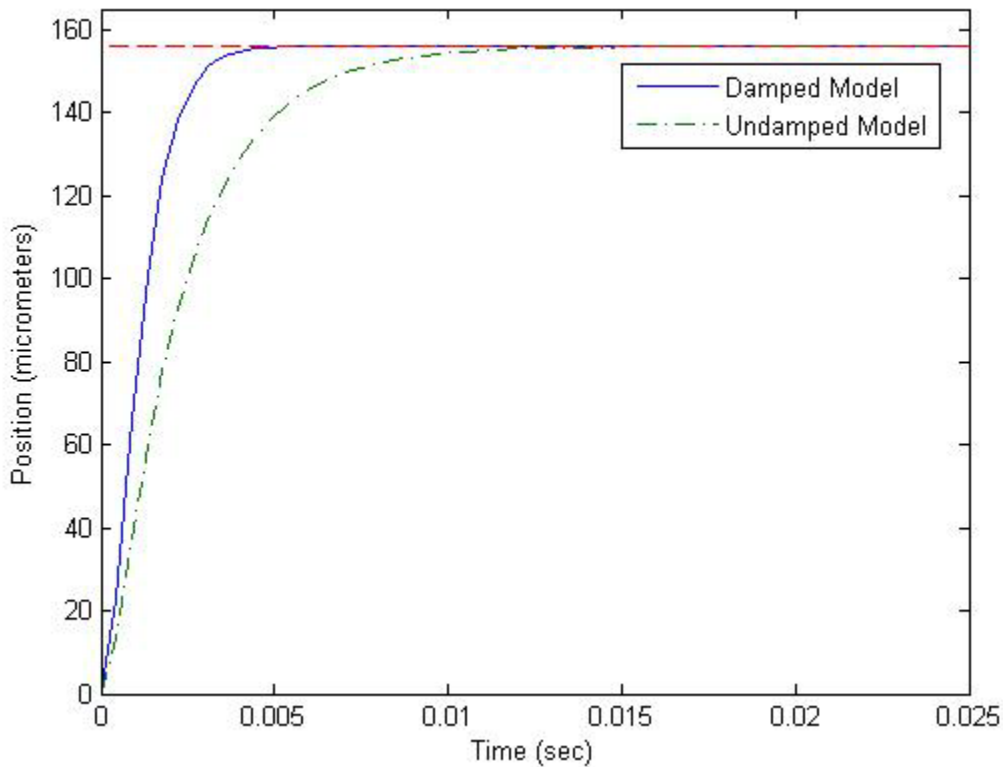


Figure 4-5. Response of the Simulink damped model ($b=10$) to a $156 \mu\text{m}$ step. The rise time is roughly half that for the undamped system.

Disturbance Response The Simulink models were also used to verify the disturbance response behavior displayed in the impulse disturbance instance described in Section 4.2. Each model was subjected to a $156 \mu\text{m}$ step over one servo cycle ($442 \mu\text{sec}$) and the

responses were observed and are shown in Figure 4-6. The plots show that the magnitude of the damped system's response to the disturbance is less than the undamped system's.

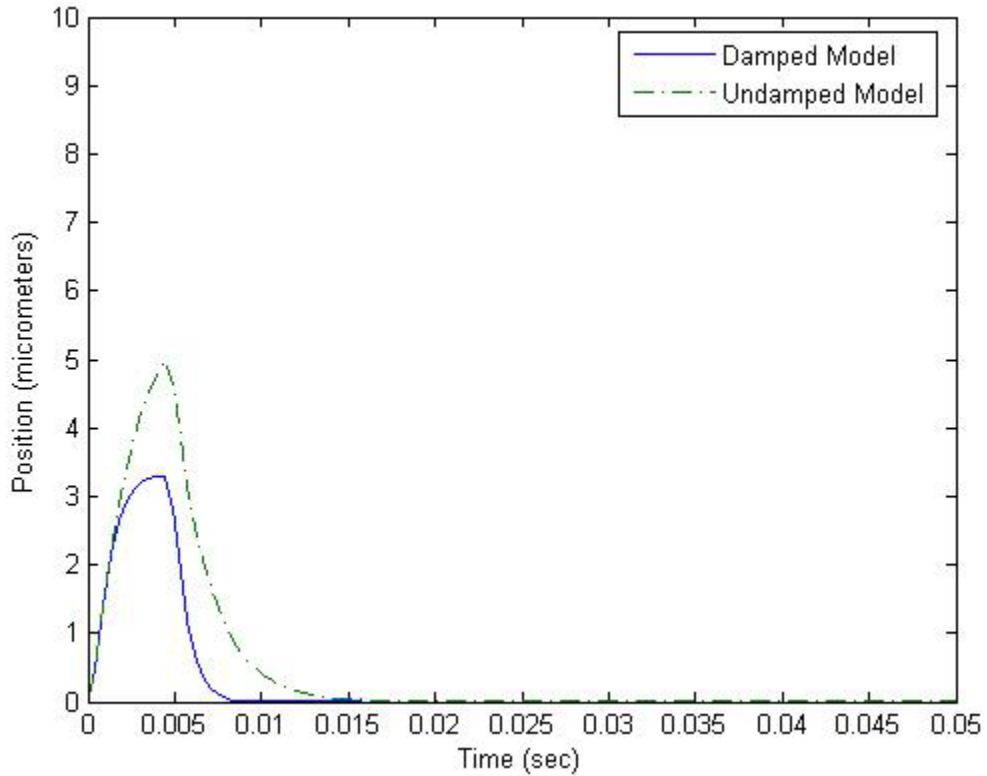


Figure 4-6. The response of the Simulink models to a 156 mm disturbance input over one servo cycle (442 μ sec). The jump seen in the damped system is smaller than that of the undamped system.

4.4.2 LAT System Tuning

The proportional, integral and derivative gains found by tuning the Simulink model were implemented in the actual controller. Feedforward gains were then added to improve the LAT's sine following ability.

Undamped System The system's response to a 156 mm step with proportional, integral and derivative gains of 400,000, 10,000 and 805, respectively, is shown with the theoretical undamped response in Figure 4-7. This system exhibits a rise time of 8 msec that is very close to the expected value seen in the Simulink model. However, it has an overshoot of 3.6 % and a high frequency oscillation is seen in the response around 150 Hz, neither of which were expecting based on the model. The cause of this frequency is undetermined, and it appeared during machining experiments (Section 5). Using alternate gains did not eliminate the oscillation and only worsened system performance, so the Simulink model gains were used.

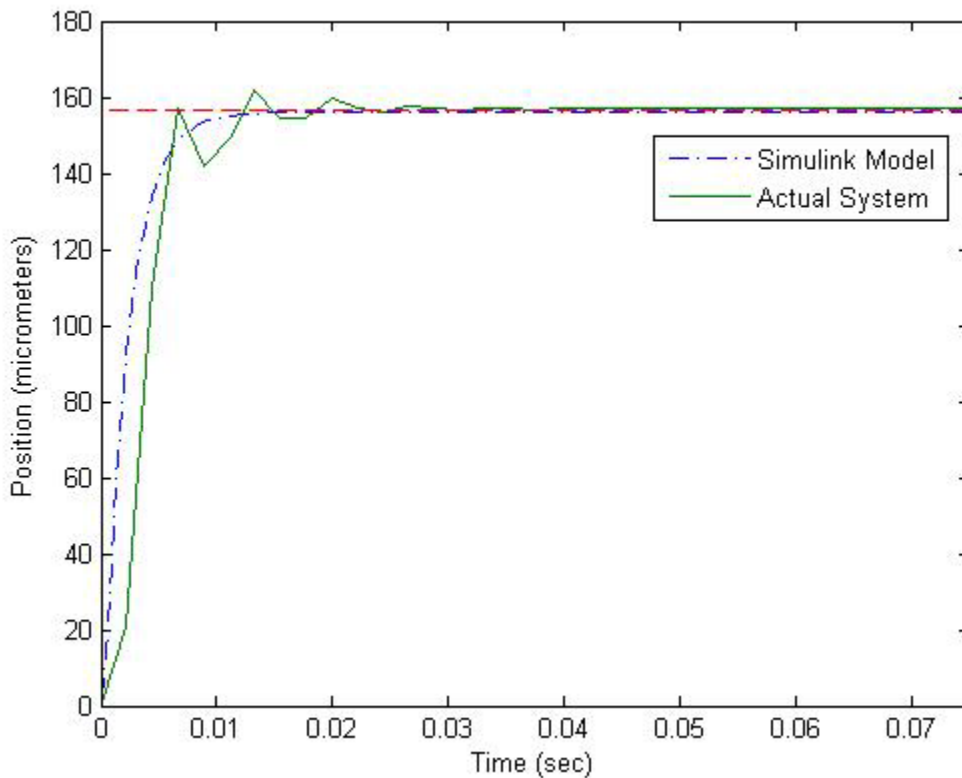


Figure 4-7. Step response of the undamped system

With the PID gains set, feedforward control was used to reduce the system's following error to a sine wave input. Feedforward control can dramatically improve control variance in cases where load changes cause big deviations from setpoint and the actual process dynamics are too slow to allow the feedback controller to operate fast enough to catch these disturbances. Feedforward control predicts the effect of the next move on the system and applies corrective action preemptively [20]. Combining feedforward control with a PID scheme resulted in the best possible system performance.

The feedforward gains were adjusted to minimize the following error for a 1 mm, 5 Hz sine wave input since this would be the profile used to machine the tilted flats (described in Section 5). The velocity feedforward gain (K_{vff}) was set equal to the derivative gain. This procedure was used in the tuning of the other Nanoform axes and typically results in optimal behavior. The acceleration feedforward gain (K_{aff}) was varied until the PV value of the following error was minimized, which was achieved when K_{aff} was 700. Figure 4-8 shows the undamped system's response to the sine wave.

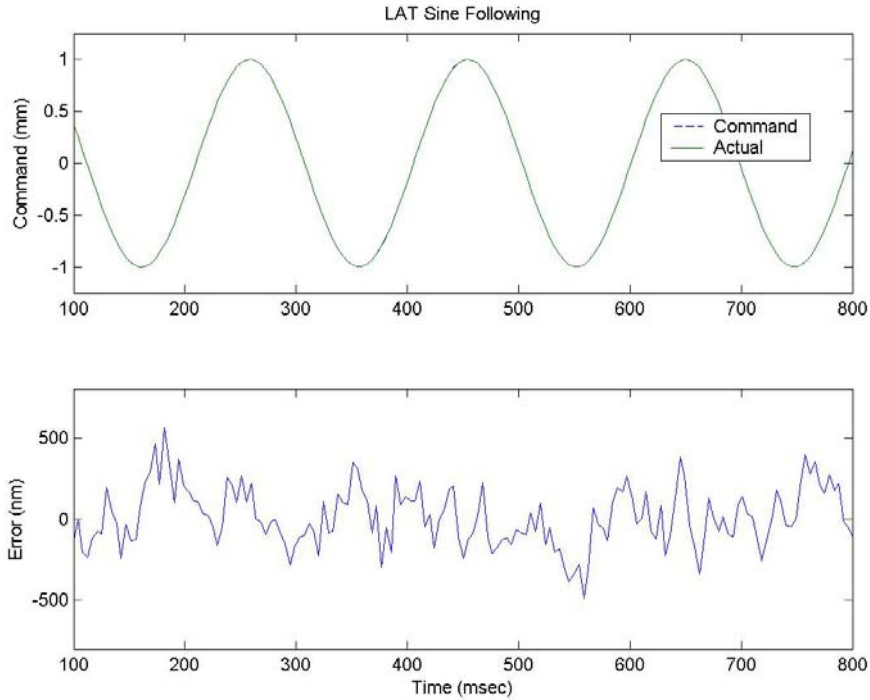


Figure 4-8. Undamped system response to 1 mm, 5 Hz sine wave. The top plot shows the command and actual motion, and the bottom plot shows the error between the two.

Since the error plotted in Figure 4-8 is the result of straight subtraction of the actual position from the command, some of it is due directly to phase shift the system undergoes. The phase error, which has an amplitude of 95 nm, was removed to examine the error due to other factors.

To remove the phase error, a 5 Hz sine wave was fit to the error data using the curve fit tool “cftool” in Matlab. This fit was used because the pure phase error will appear as a constant amplitude sine wave out of phase with the command. The sine fit lagged the input command by 90 degrees, indicating that the error is proportional to LAT velocity.

The values of this best fit sine wave were then subtracted from the error vector, resulting in the following error not due to phase shift. The difference is shown in Figure 4-9.

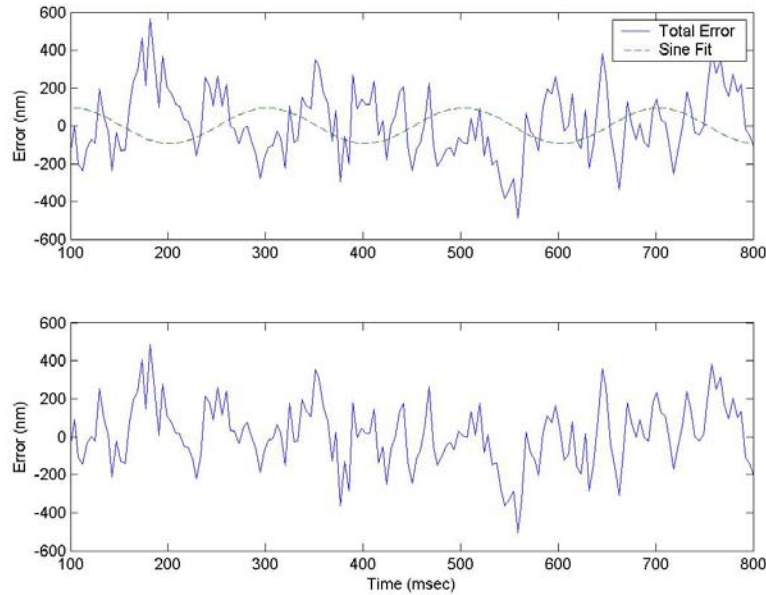


Figure 4-9. Phase error sine fit (top) and undamped system sine following error with phase lag removed.

The top plot in Figure 4-9 shows a sine fit representing the error due to phase shift. This fit was subtracted from the total error to get the bottom plot, which represents the noise error of the system with the phase error removed. This error has a PV value of 990 nm and an RMS of 170 nm. As seen in Figure 4-9, the a sine wave does not provide a good fit to the data ($R=0.2$), so most of the error is not due to phase shift. The remaining error does not appear at a finite frequency, suggesting it is an artifact of external sources such as encoder noise or unwanted motion due to current loop noise in the amplifier. However, due to the sample rate of the data collection (225 Hz), only frequencies up to 112 Hz would be apparent.

The final gains used for the undamped system are shown in Table 4-1.

Proportional gain (K_P)	400,000
Integral gain (K_I)	10,000
Derivative gain (K_D)	805
Velocity feedforward gain (K_{Vff})	805
Acceleration feedforward gain (K_{Aff})	700

Table 4-1. Final gains used for the undamped LAT system (sampling time = 442 μ sec).

Damped System The tuning procedure used for the undamped system was also used for the damped system. The step response of the damped system for gain values of 700,000 (K_P), 400 (K_D) and 10,000 (K_I) is shown in Figure 4-10. Because of the added physical damping, a proportional gain nearly twice as large as that used in the undamped system could be used with the damped system. Additionally, half as much derivative gain was needed in the damped system as in the undamped system due to the added damping, and the integral gains were the same for both systems. This response has a rise time of 5 msec (the model predicted 4 msec). However, it has an overshoot of 8.1% when none was expected based on the modeling. As in the undamped response, an oscillation is seen during the rise, this time at 200 Hz. The cause of this frequency is unknown. Alternate gains were implemented and did nothing to delete the oscillation and worsened system performance, so the Simulink gains were used.

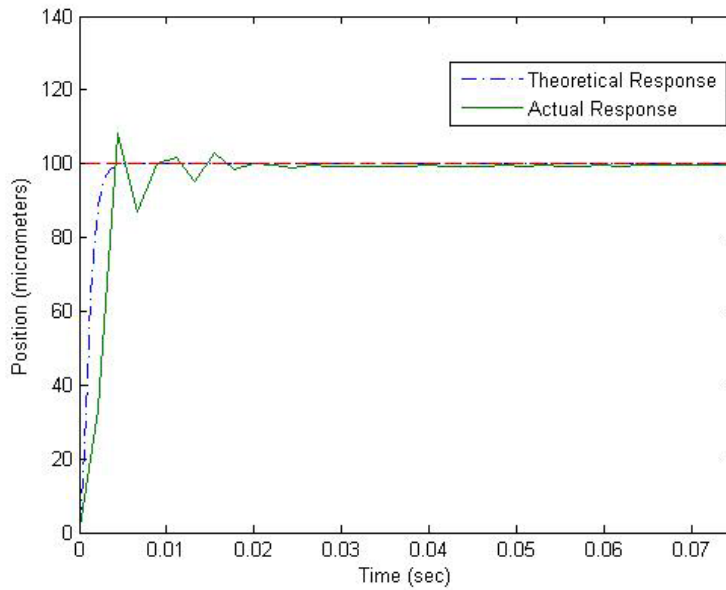


Figure 4-10. Step response of damped system.

The optimal feedforward velocity and acceleration gains to minimize sine following error are 400 and 440, respectively. The damped system's response to a 1 mm, 5 Hz sine wave and the total error created are shown below in Figure 4-11. Since the total error shown in the bottom plot of Figure 4-11 contains phase error, which have no negative effects on system performance, the same process described for the undamped system was used to remove the phase error, which had amplitude of 260 nm. The best-fit sine wave (top plot of Figure 4-12) represents the phase error of the damped system. This sine wave ($R=0.5$), which lags the input signal by nearly 90 degrees (indicating that it's proportional to velocity), was subtracted from the total error to obtain the error of the system not due to phase lag (bottom plot of Figure 4-12), which is the harmful error from a surface finish standpoint. The remaining error has a PV value of 985 nm and an RMS of 188 nm. Since the controlled performance of the damped and undamped systems are very close to the same (985 nm PV for the damped, 990 nm for the undamped), the machining

experiments outlined in the next section serve to highlight the difference external physical damping (or lack thereof) has on two systems that have very similar performance.

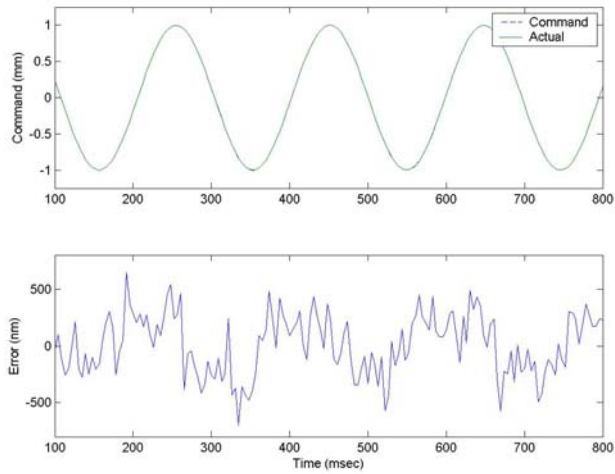


Figure 4-11. Damped system response to 1 mm, 5 Hz sine wave. The top plot shows the command and actual motion. The bottom plot shows the error between the two.

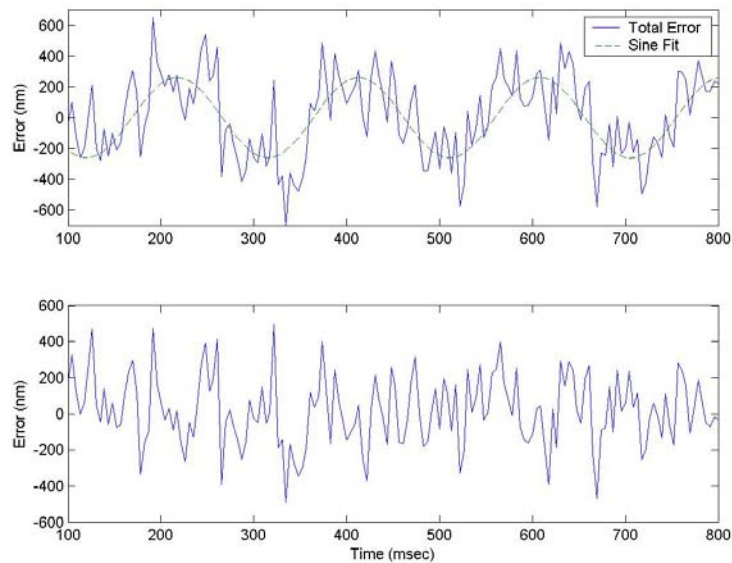


Figure 4-12. Phase error sine fit (top) and damped system sine following error with phase lag removed.

Table 4-2 shows the final gains used for the damped system.

Proportional gain (K_P)	700,000
Integral gain (K_I)	10,000
Derivative gain (K_D)	400
Velocity feedforward gain (K_{Vff})	400
Acceleration feedforward gain (K_{Aff})	440

Table 4-2. Final gains used for the damped LAT system.

Disturbance Rejection The disturbance rejection for the damped and undamped systems was measured to compare with the model. The setup shown in Figure 4-13 was used for the tests. A string with a 100 gram weight attached was tied to the motor bracket and hung over the pulley shown. The weight was lifted and dropped, and the LAT axis position was recorded.

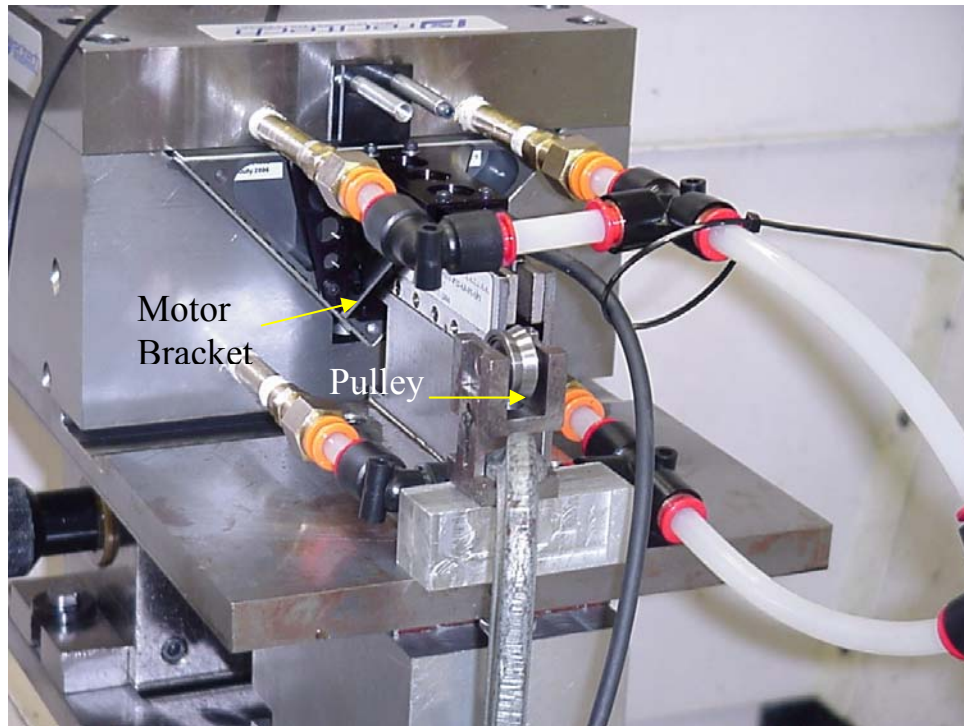


Figure 4-13. Setup for the disturbance rejection test. A string with a weight attached was tied to the motor bracket and hung over the pulley. The weight was dropped, and the system's motion was recorded.

Figure 4-14 shows the response of the undamped (top) and damped (bottom) systems to the external disturbance, with the theoretical response shown with a dotted line. The magnitude of the error for the undamped system is nearly twice as large as the damped system, showing that damped system is more robust when faced with external disturbances. The undamped system returns to 90% of its original value faster than the damped system, but time to totally return is the same for both systems (~ 1 sec). Although the values of the position jumps varied slightly from experiment to experiment due to dropping from different heights, the trend was repeatable, and the same behavior

was noticed during the controller modeling described in Section 4.4.1, although the modeled response was much faster.

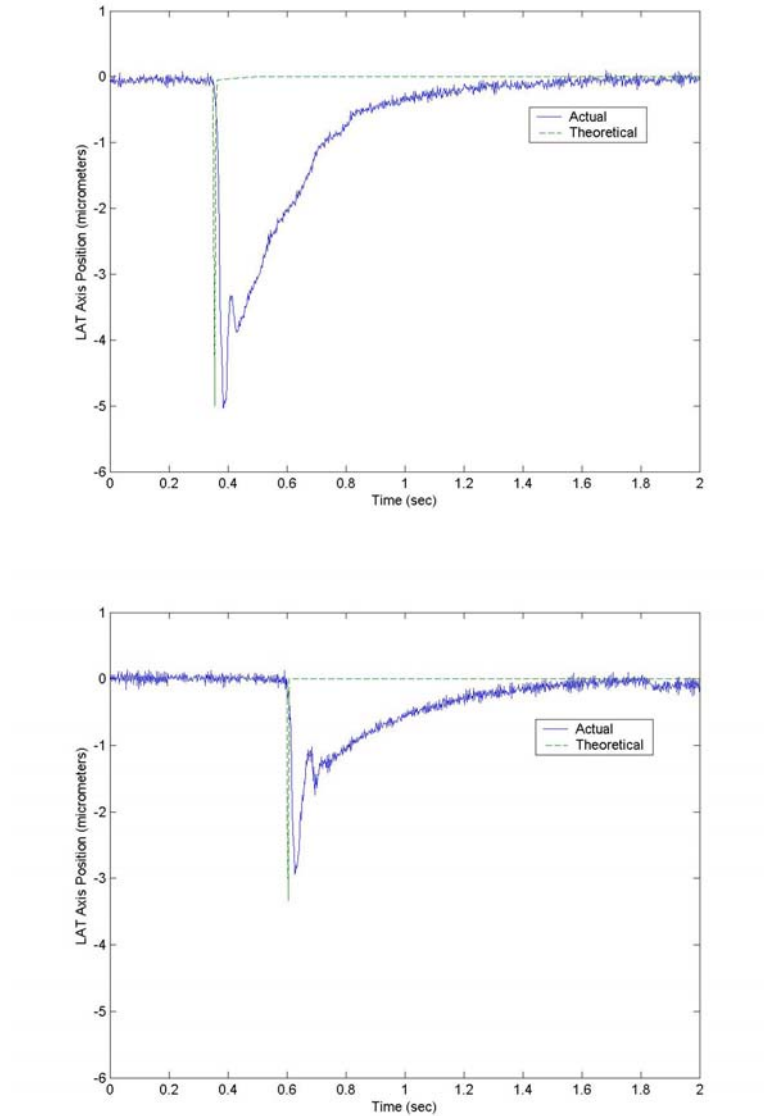


Figure 4-14. Undamped (top) and damped (bottom) system response to external disturbance, with the modeled/theoretical responses shown as dotted lines. A smaller peak value for the damped system shows it is more resistant to external forces.

5 Machining Experiments

Two types of cutting tests were used to study the performance of the LAT: machining a flat surface and machining a tilted flat. Initial testing was performed on PMMA (PolyMethyl-MethAcrylate) pieces and later tests used copper and aluminum parts. The experiments and changes made to the system throughout the process are described in the following sections. Figure 5-1 shows a photo of the LAT axis on the Nanoform 600.

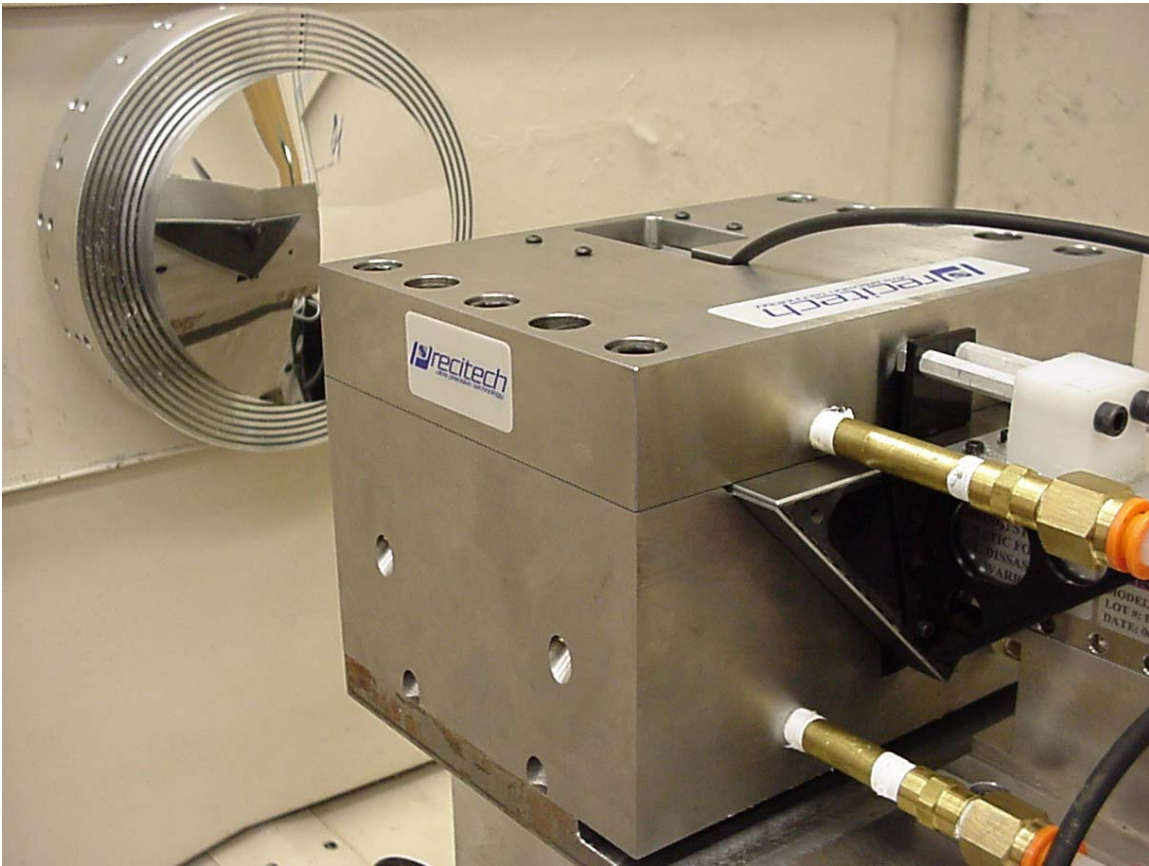


Figure 5-1. LAT axis on the Nanoform 600.

5.1 PMMA Flat

PMMA was a good choice because it is possible to obtain optical surface finishes and because the material is quite soft, the machining forces are small even for large depths of cut. Also, the PEC has experience with this material and it was considered a known quantity. Samples were 50.8 mm diameter, 50.8 mm high cylinders. For the tilted flats, 2 mm of material needed to be removed, so a large depth of cut allowed the part to be machined with a minimum number of passes. Also, if control was lost during the machining experiments, the likelihood of damaging the tool would be substantially less than if a metal workpiece was chosen.

The flat was machined to test the ability of the LAT axis to hold position while machining. External damping was not used for this experiment. The flat was cut at 500 rpm with a 1 mm/min feedrate and 5 μm final depth of cut using a tool with a 1 mm nose radius. The Scanning White Light Interferometer (SWLI) measurement in Figure 5-2 shows the average surface roughness over the 1x1.5 mm area to be 87 nm (Ra) (the theoretical PV was 1 nm). The upper left top-down view of the surface shows an arrow indicating a trace in the tool motion direction. This trace is shown in detail in the lower left. The features along this trace and the accompanying autocovariance plot (bottom right trace) indicate 12.3 nm P-P height at a spatial frequency of 6 μm . This indicates a frequency too high to be vibration and therefore is attributed shear bands in the plastic, as documented by Kobayashi [27]. The shear bands account for less than 15% of the surface roughness for the flat surface.

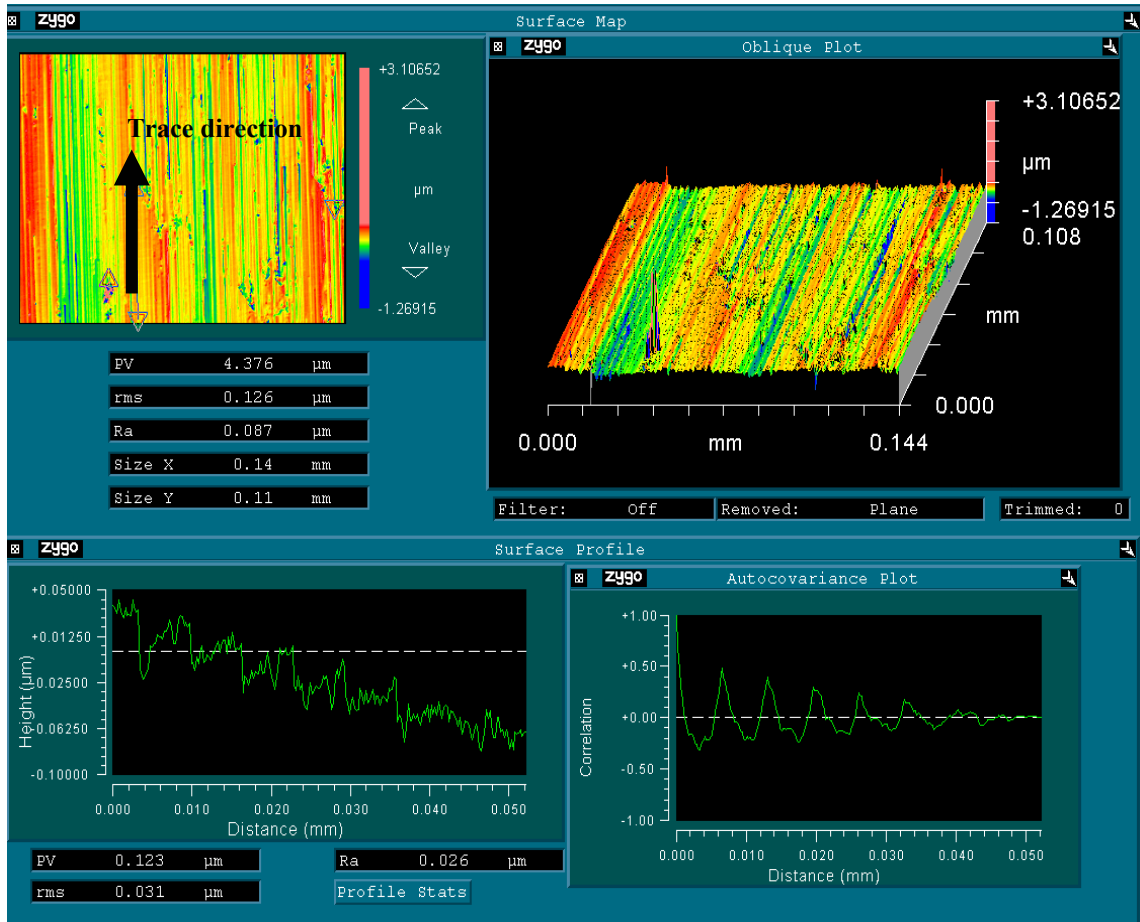


Figure 5-2. Scanning White Light Interferometer (SWLI) image of the PMMA flat machined at 500 rpm with a 1 mm/min feedrate.

The cause of the remainder of the surface error cannot be directly deduced from the surface measurement, though indirect evidence shows two likely main sources: Encoder signal noise and resonance in the LAT axis control. Noise associated with the PWM (pulse width modulation) amplifiers used to power the linear and spindle axes of the DTM is present in the analog encoder signal. This noise appears in the system as a broad-band quasi-white noise. With this noise on the encoder signals, the position feedback signal read by the control algorithm contained a significant error. As a result, the controller failed to accurately position the axis. This is a vulnerability of the chosen encoder feedback system (Section 4.1) where an analog sinusoidal signal is read directly

by the controller as opposed to going through an interpolator box that then sends a digital position feedback signal. Reading the sine wave signals directly was selected because of the need to measure the position at both high resolution and high velocity. Once the noise problem was identified, it was improved from 800 nm PV to 400 nm PV by adding line filters to the axis motors.

The resonance in the axis control system was another source for the high surface roughness measured on the flat surfaces. The axis error during machining is shown in Figure 5-3 along with the frequency content. The time plot over one second shows peaks with a magnitude of 1.6 μm which is similar to the surface roughness of the machined flat. The major frequency identified is 265 Hz. The origin of this peak is not known but a similar value was present during machining of the tilted flat discussed later in Section 5.3. To remedy this problem, a notch filter was added to the controller in the vicinity of 265 Hz as described in Section 5.4. Additionally, extra shields were added to the circuitry to eliminate as much random noise as possible (Section 5.4).

Figure error for the flat was to be measured using a Zygo GPI laser interferometer. Due to the greater than expected roughness and the low reflectance of PMMA, however, measurements could not reliably be made through interferometry. Instead, figure measurements were made using a Brown & Sharpe Gage 2000 Coordinate Measuring Machine (CMM) shown in Figure 5-4. While this instrument was helpful in measuring the form of the tilted flats, the PMMA non-tilted part was found to be flat to better than 1 μm – the resolution of the CMM.

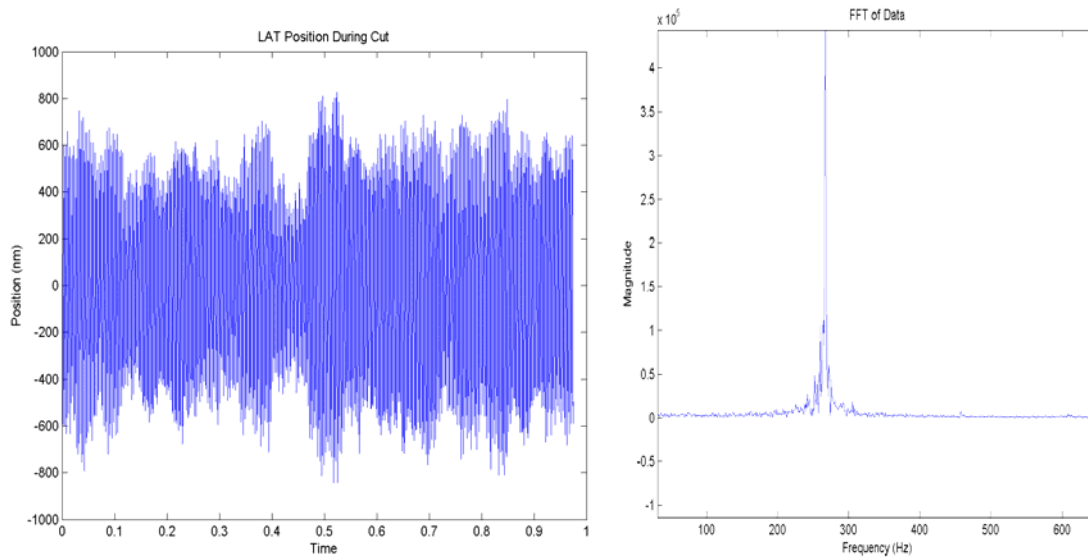


Figure 5-3. Error motion (left) of the LAT axis (commanded minus actual position) during machining at 500 rpm. The figure at right is the FFT of the error.

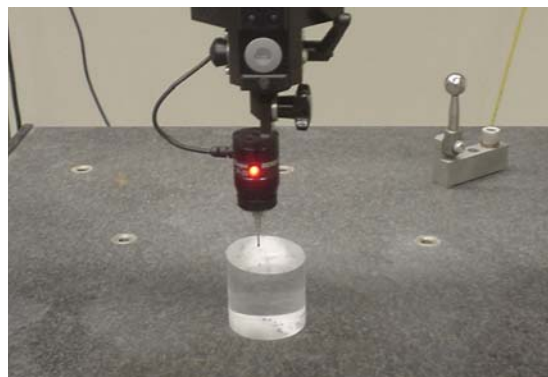


Figure 5-4. Tilted flat being measured by the coordinate measuring machine (CMM). The non-tilted part was flat to less than $1 \mu\text{m}$ – beyond the resolution of the machine.

5.2 Tilted Flat Procedure

The second experiment involved the fabrication of a tilted flat. A sketch of this experiment is shown in Figure 5-5 with the LAT slide moving the tool in a sine wave motion with one cycle per rotation of the part. The LAT slide is programmed to generate a particular depth at each rotary encoder location. As the tool moves from the OD to ID, the tool will move in and out once per revolution with decreasing amplitude to create a flat surface that is tilted with respect to the spindle face. This shape was chosen because it tests the system's signal following capabilities and is easily measured with standard metrology equipment.

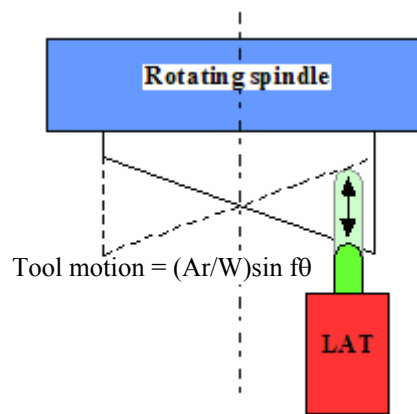


Figure 5-5. Top view of DTM during generation of the tilted flat

5.2.1 Tool Radius Compensation

Due to the radius of the tool and the slope of the part, the position of the LAT axis must be adjusted during cutting to ensure contact of the tool edge with the part is made at the proper location (since the point of contact along the edge is always changing). This adjustment is called tool radius compensation and is always subtracted from the commanded position. The need for radius compensation is illustrated in Figure 5-6. In

the top diagram, the tool is perpendicular to the surface of the part and no compensation is necessary. However, in the bottom picture, the surface is tilted with respect to the tool. This creates unwanted contact along the side of the tool, so the tool must be moved upward to stay on the desired surface. The amount of compensation needed increases as the surface angle increases. Figure 5-7 shows the tool radius compensation associated with an excursion of 4 mm (peak to valley) for a 50 mm diameter part. There are two peaks and two valley per revolution, the amplitude of which are roughly 0.25% of the tool motion amplitude. The figure shows the maximum compensation is need when the LAT is at the peak (positive or negative) of its travel, and no compensation is needed as the LAT position crosses zero because the tool is perpendicular to the part. Tool radius compensation equations and analysis are given in Appendix N.

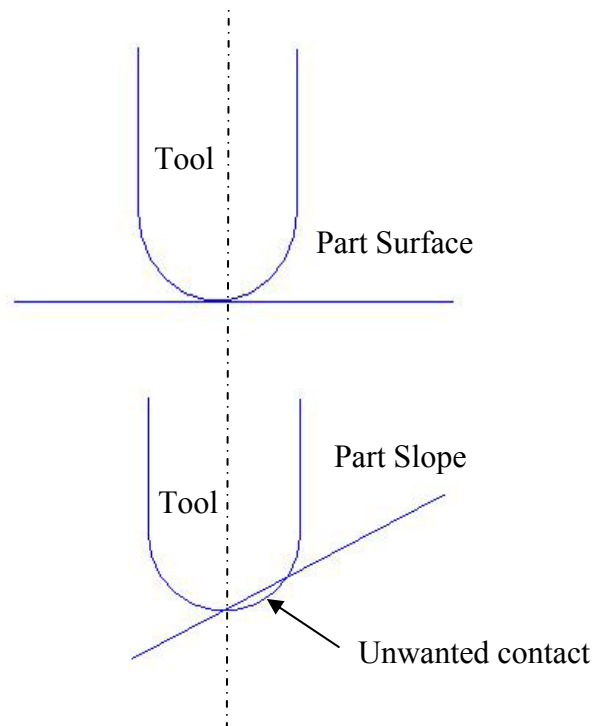


Figure 5-6. Tool tip contact with a flat surface (top) and a tilted surface (bottom). Tool tip compensation is needed to eliminate the unwanted contact associated with a tilted surface.

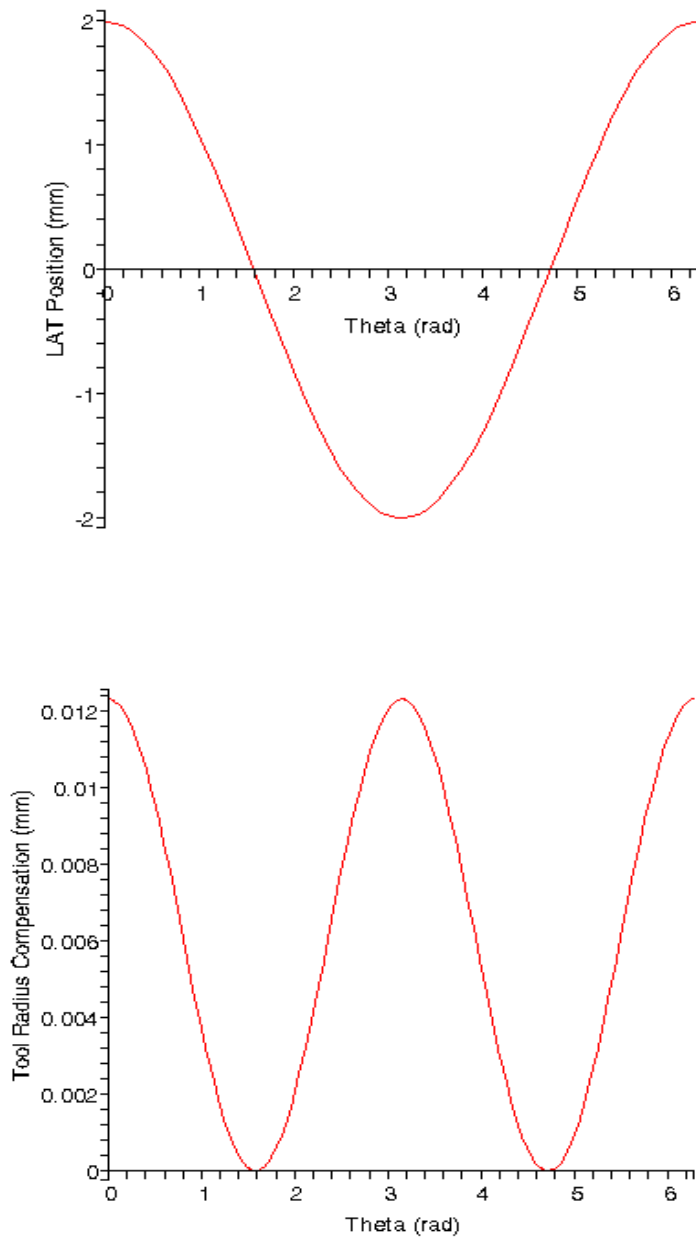


Figure 5-7. The LAT position (top) and the associated tool radius compensation (bottom) for a 1 mm radius tool and a 2mm peak-to-peak flat at 25 mm radius. The compensation is always subtracted from the commanded position.

5.2.2 Cutting Procedure

To machine the tilted flats a motion program had to be written to generate points on the desired tool path. Two methods were explored for creating the motion program for the cutting process. They are described in the following sections.

Position-Based Cutting The first cutting method involved reading the spindle and x-axis positions from their encoders in real time and, based on their locations, creating a force command for the LAT axis. Because the LAT axis motion is based solely on the position of the other axes, this method is referred to as position-based cutting. This was initially attempted with a “while” loop in a PMAC motion program (Appendix I). However, the extensive calculations delayed the loop. In addition, the other axes did not get a new command until the program exited the loop creating a signal that was not smooth.

To create a smoother command based on the spindle and x-axis position, the PMAC kinematic calculation structures were used. These routines read axis positions and deliver a command to another axis at a regular interval. Unlike the “while” loop, all axes received commands at regular intervals, creating a smoother command.

The kinematic routine needs two programs: the forward kinematics program and the inverse kinematics program. The forward kinematics program reads the positions of all the defined axes and places them in a string of operational variables. The inverse kinematics program uses these variables to calculate a command for the LAT axis and places it in the target position register. This exchange takes place in a fixed interval

called the segmentation time, which has a minimum value of 1 msec. The problem with using this type of programming is the segmentation time does not match the servo update time of 442 μ sec. The difference in these two frequencies (1 KHz segmentation and 2.2 KHz servo update) produces a beat in the command, which is seen in the signal at 250 Hz. This frequency is shown in a 1 mm, 5 Hz signal in Figure 5-8 . The top plot shows the position error when using the kinematics routing to command motion. An FFT plot of the frequency content of the error (bottom) shows the 250 Hz occurrence. The magnitude shown in Figure 5-8 is the relative power of the content, but this frequency caused a peak to valley error of 20 μ m in the motion. Because of this large error, a different approach was taken to programming the axis. The kinematics programs are shown in Appendix I.

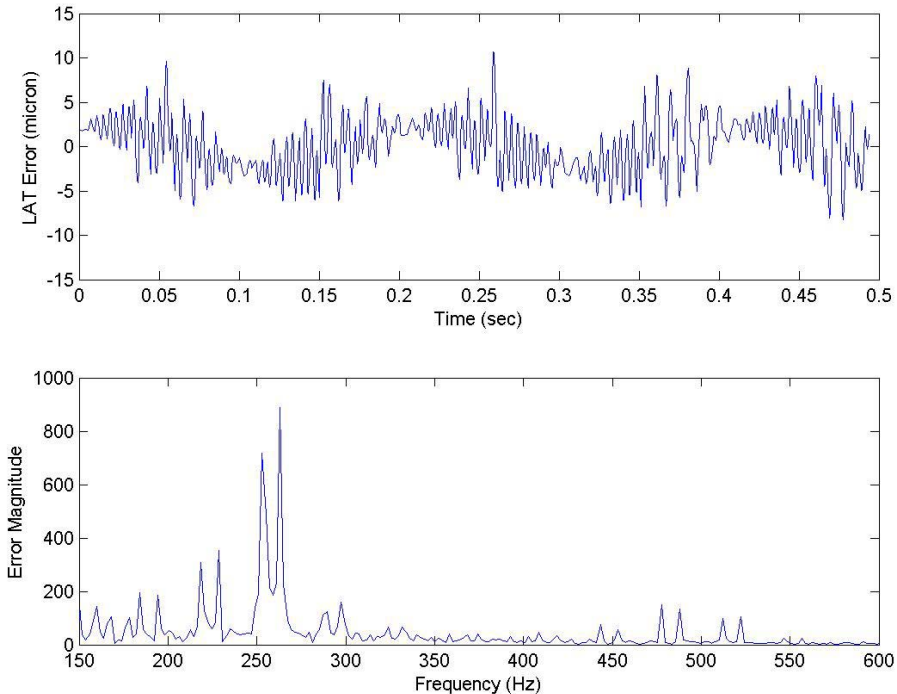


Figure 5-8. LAT axis error generated with the kinematics routine (position-based).

Time-Based Cutting The second method, ultimately used for machining, was independently programming each axis along a desired path. While the axes move with no knowledge of what the others are doing, the controller is responsible for getting each one in the right position at the right time. The error generated by the time-based motion program is shown in Figure 5-9. The LAT motion is much more smooth and the 250 disturbance (as well as that at higher frequency content) is no longer present (bottom plot). This method (“Time Based Cutting” section in Appendix I) improved the following ability of the system by a factor of two and was used for the machining experiments.

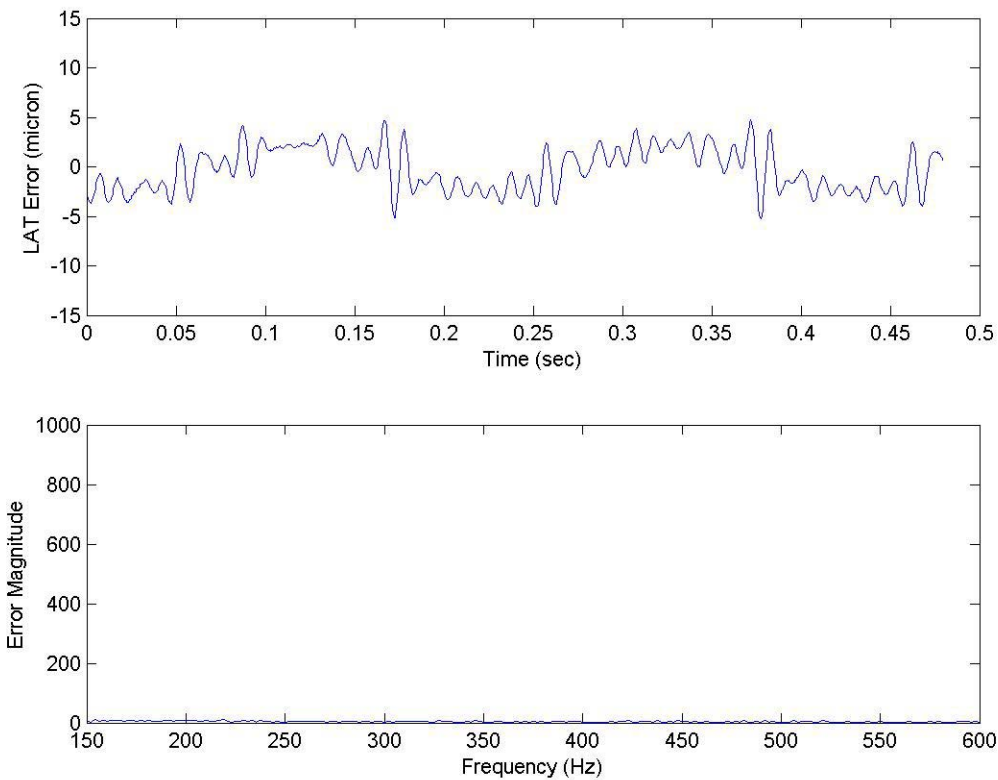


Figure 5-9. LAT axis error generated by the time-based motion program. The 250 Hz. frequency is no longer present.

5.3 PMMA Tilted Flat

The PMMA tilted flat was machined at 500 rpm with a 2.5 mm/min feedrate (5 $\mu\text{m}/\text{rev}$) and 5 μm final depth of cut. These conditions give a theoretical PV surface finish of 3 nm. The time-based cutting procedure described in the previous section was used. Roughing cuts were first performed using a 100 μm depth of rough cut the slope on the part.



Figure 5-10. Surface of the 2 mm PMMA tilted flat machined at 500 rpm with a 2.5 mm/min feedrate. The radial direction is approximately along the grooves.

A sample roughness measurement over a 719x539 μm region is shown in Figure 5-10. This region is about 5 times larger than the flat in Figure 5-2 and represents 144 passes of the tool. Two features dominate the shape of the tilted flat; one is an undulation in the radial direction with a spatial wavelength of 400 μm and the other is lower amplitude but parallel feature with a wavelength of 60 μm . These features are likely due to vibration of the LAT axis. However, an accurate representation of the vibration cannot be obtained by tracing along the grooves because they are the result of vibrations in the tool direction lining up on successive passes. While the amplitudes of vibration of the axis and those measured on the surface are of similar magnitude, correlating any one frequency to the surface defects is not possible. Figure 5-11 shows the time signal and frequency spectrum of the position error (commanded position minus the encoder reading) recorded during the machining of the tilted flat. The FFT shows many resonances occurring in the motion, one of which occurs around 65 Hz. Additionally, a component of the frequency spectrum is seen around 110 Hz, which was shown to be the natural frequency of the Nanoform's z-axis in Section 2.10. Finally, as was the case during the PMMA flat cut, a 250 Hz frequency was observed. Section 5.4 explains the measures taken to reduce the effects of these resonances.

Due to the greater than expected roughness and the low reflectance of PMMA, measurements could not be made through interferometry, so the Browne and Sharp CMM was used. The tilted flat has a P-V error of 46 μm . The shape of the error is due to varying phase shift during the cut and will be described in Section 5.6, as it was seen in subsequent parts.

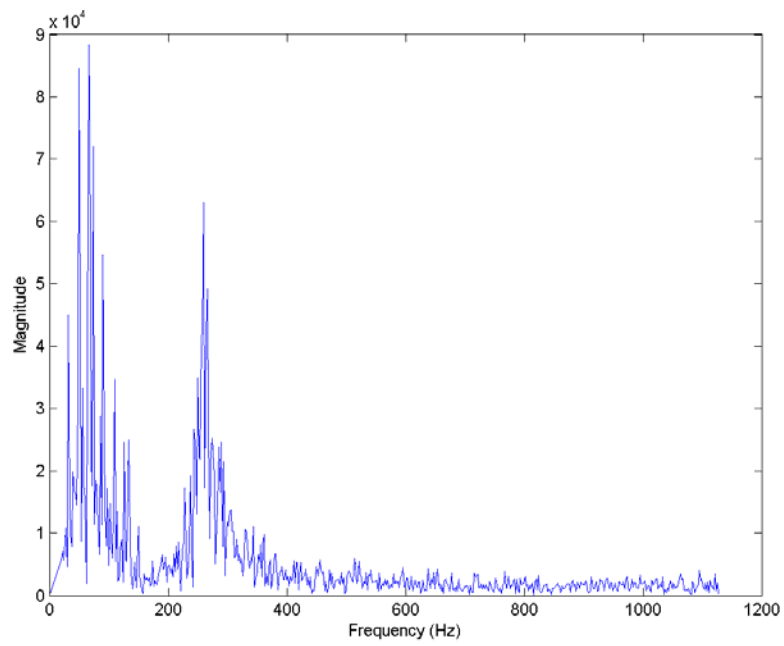
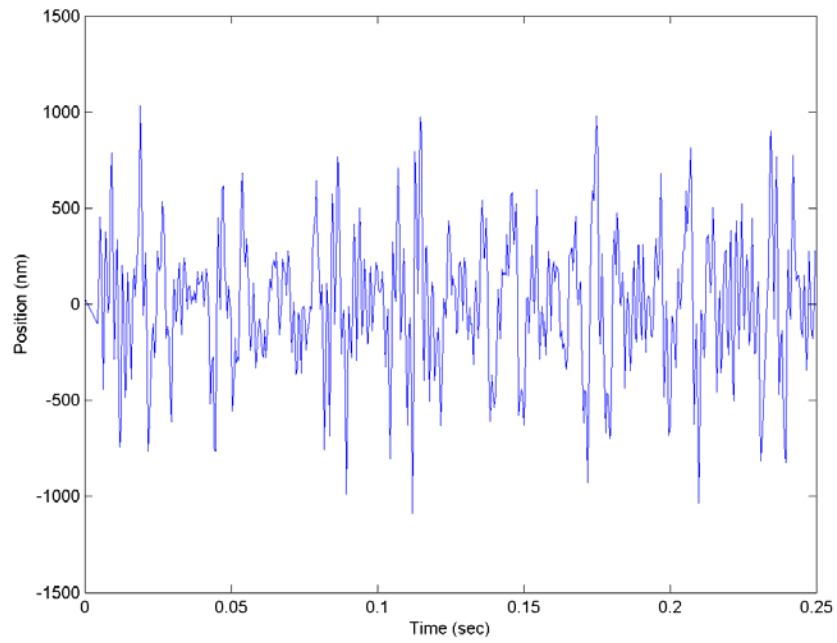


Figure 5-11. PMMA tilted flat cutting data. The top plot shows the error during cutting.

The bottom plot shows the frequency content of the error.

5.4 System Modifications

After the initial set of machining experiments, some changes were made to the LAT system to improve the performance and the flat and tilted flat were machined again. The system changes and results from the second set of experiments are described below.

Encoder Noise The first area of improvement was noise in encoder system. With a large amount of noise in the encoder line, the position of the LAT is uncertain and the controller generates an incorrect control command. This noise level was greatly reduced by adding edge filters to the PWM motor amplifiers and adding shields to the encoder wiring. Edge filters are used to reduce electrical noise from the power cabling that connects PWM amplifiers to their loads. This noise usually shows up at a very high frequency, and by rounding the corners of the PWM pulses, the filters greatly reduce the high frequency components of this noise. The added shields protect the system against ambient electrical noise. The combined effect of these changes reduced the signal noise on the machine ground by significantly. However, the results for the encoder were not quite as dramatic, reducing the noise level from 100 nm P-V to 50 nm P-V. Much of the remaining noise was likely caused by the amplifier power source.

Physical Damping As described in Section 3.2.3, physical damping was added to the system to improve performance.

Notch Filter A notch filter was added to the controller to eliminate the sharp peak around 250 Hz seen during the PMMA flat and tilted flat machining experiments (Figure

5-11). The effect of the notch filter is shown in Figure 5-12. The top graph shows the old system FFT (excluding 8.3 Hz from the command signal) without the notch filter. The bottom shows the system with the addition of the notch filter, which effectively removes the 250 Hz frequency.

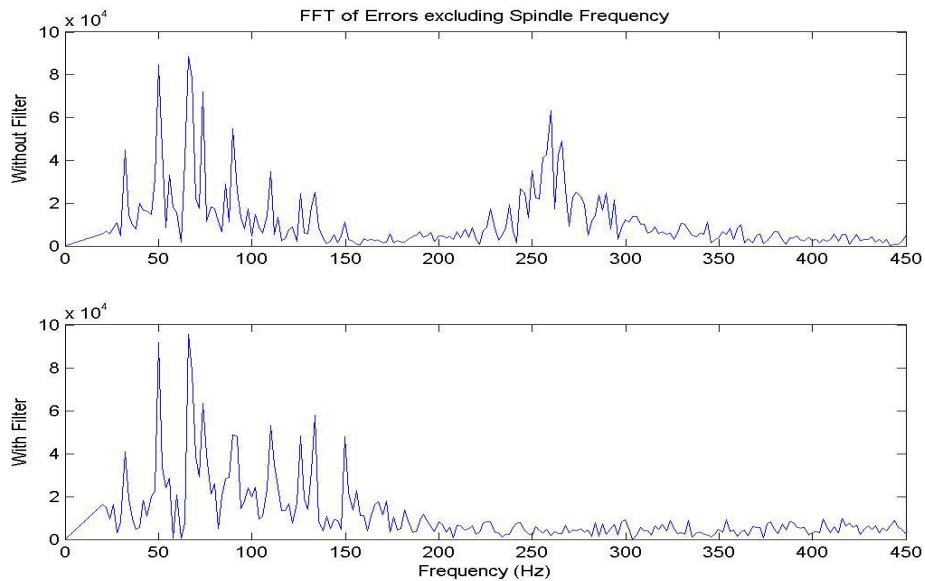


Figure 5-12. The effect of the notch filter in the controller on the system performance.

5.5 Copper Flats

After modifying the system to correct problems from the PMMA cutting process, copper flats were cut. The copper pieces were 12.7 mm in diameter and were cut at 400 rpm with a 0.84 mm/min feedrate (2 $\mu\text{m}/\text{rev}$) and 5 μm finish pass depth of cut. These parameters represent a theoretical PV surface of 1 nm. One flat was cut without damping and one with added external damping to compare the system performance.

5.5.1 Undamped Copper Flat

The surface of the flat cut without damping is shown in Figure 5-13 at 50X with 2.0 zoom. This 50 X 70 μm patch represents approximately 35 tool passes. The image was taken with a scanning white light interferometer (SWLI). The part has a surface finish of 16 nm (Ra) over the section shown, a considerable improvement over the PMMA part, which had a finish of 87 nm (Ra).

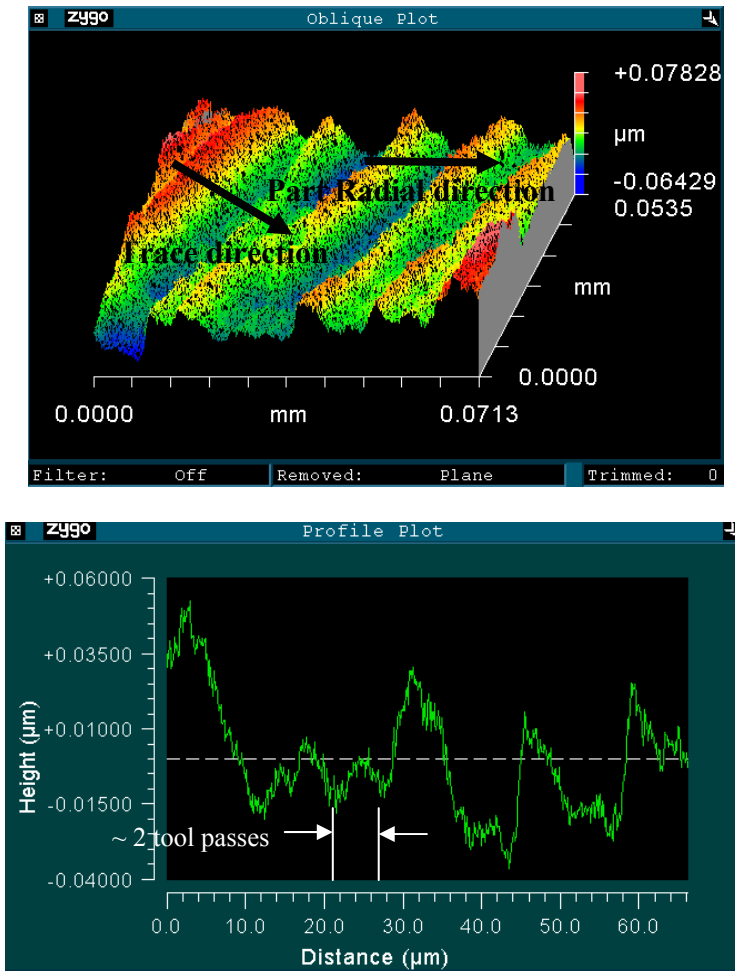
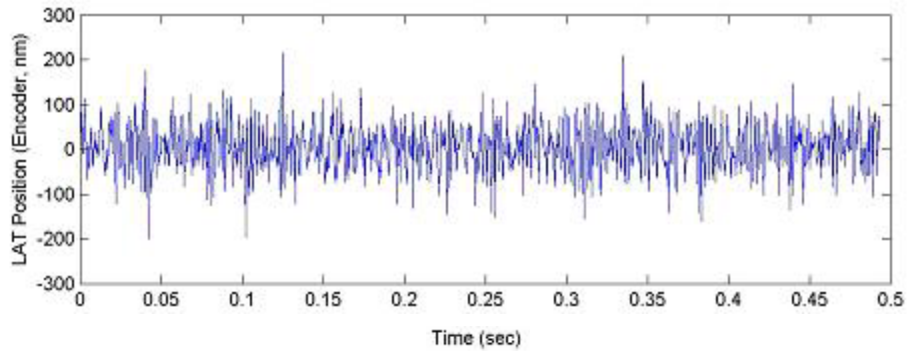
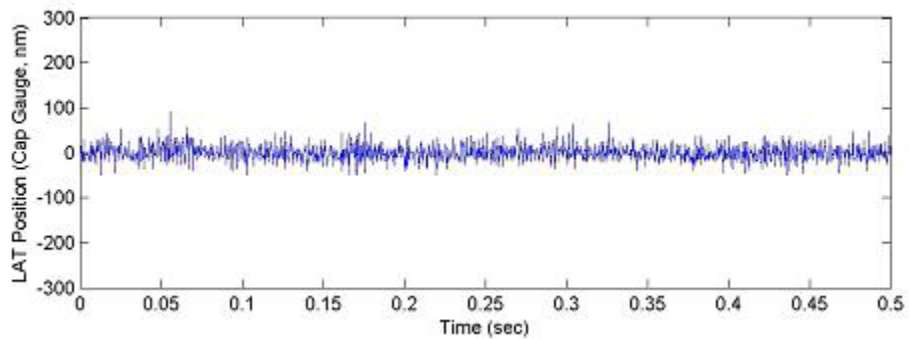


Figure 5-13. 50 X 70 μm area of a 12.5 mm diameter flat machined without damping (Ra = 16 nm). The spindle speed was 400 rpm and the federate was 0.84 mm/min and the tool nose radius was 1 mm.

One cause of the roughness on the surface is shown in Figure 5-14. The plot shows the motion of the LAT axis during position holding (desired motion is zero) as read by the LAT's encoder. Since the peak to valley motion of the slide seemed large, a capacitance gauge was used to check the LAT motion (Figure 5-15). The cap gauge data is shown in the bottom plot of Figure 5-14. This data indicates the LAT axis is not moving as much as the encoder is reporting. Therefore, the control effort is different than it should be and is not positioning the axis as efficiently and accurately as possible.



a. Encoder



b. Lion capacitance gauge

Figure 5-14. LAT motion during position holding. The top plot (a.) shows the motion reported by the LAT encoder. The bottom plot (b.) is Lion capacitance gauge data for the same experiment.

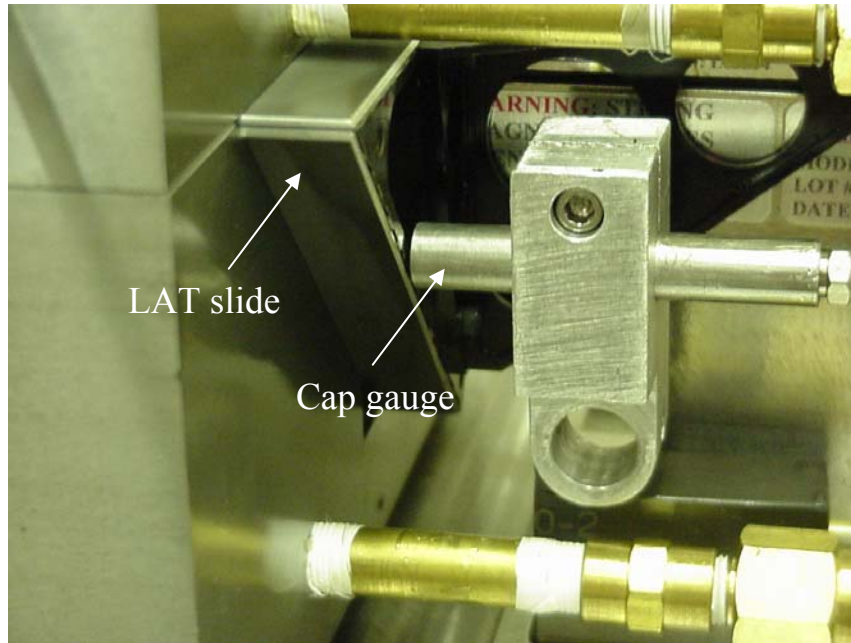


Figure 5-15. Cap gauge data collection setup.

The data from the cap gauge and the LAT encoder show the presence of 400 Hz and 1000 Hz frequencies, although neither accounts for more than 30% of the motion. These values have not been noticed in previous tests and are likely remnants of higher frequencies aliased down by the sample rate (2.2 KHz).

Figure 5-16 shows a Zygo laser interferometer image of the entire part. The figure shows the part's deviation from a perfect flat. The PV form error over the entire part is 321 nm (Ra 27 nm), which is less than $\frac{1}{2}$ wave. This value is very close to the observed PV motion of the slide during position holding (Figure 5-14a) and thus is the limiting factor in achieving better finishes.

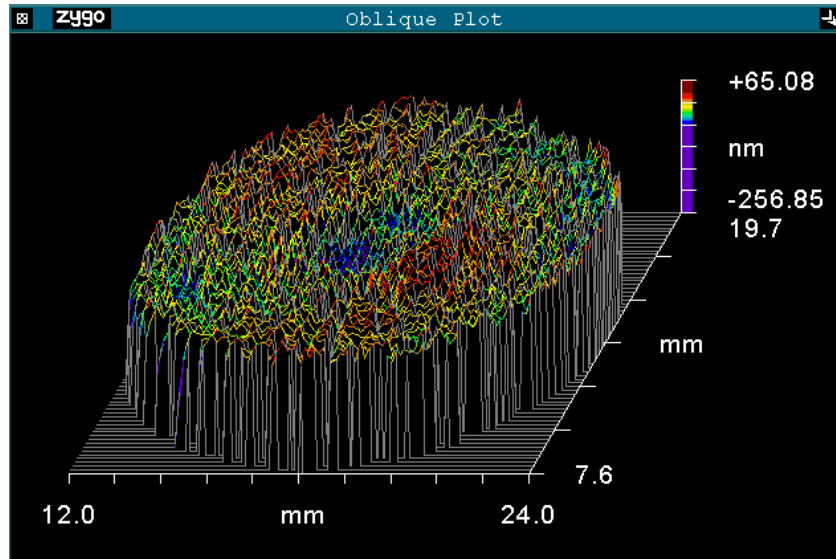


Figure 5-16. Zygo Laser Interferometry image of the surface of the flat cut without damping. The 12 mm diameter surface is flat to less than $\frac{1}{2}$ wave. The part was cut with a spindle speed of 400 rpm and a federate of 0.84 mm/min.

5.5.2 Damped Copper Flat

Figure 5-17 shows the surface of a 12 mm flat cut with the damped LAT system. A 50 X 70 μm section is shown, again representing roughly 35 passes. This SWLI image has a surface finish of 14 nm (Ra), slightly better than the 16 nm surface finish created by the undamped LAT.

A laser interferometry image measuring the difference between the machined flat and a perfect flat is shown in Figure 5-18. The PV form error is 381 nm (29 Ra). Again, the LAT axis position holding error is the limiting factor, as the surface cannot have any less error than what is seen during a zero input command.

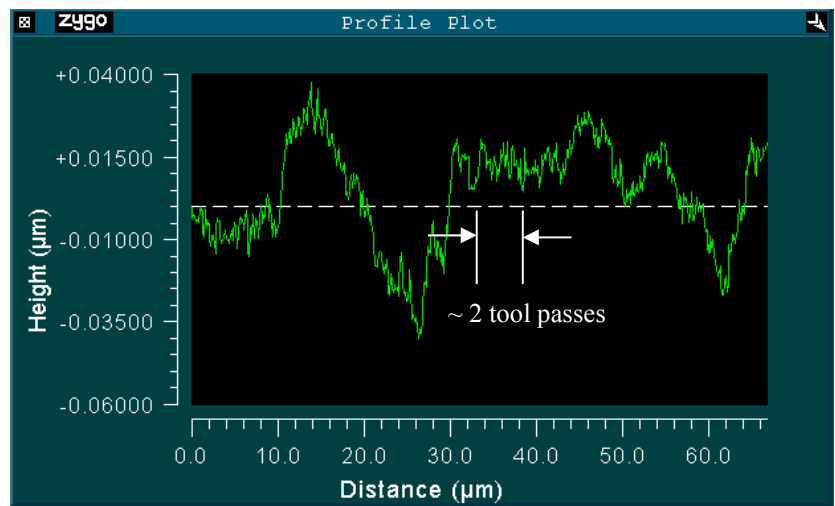
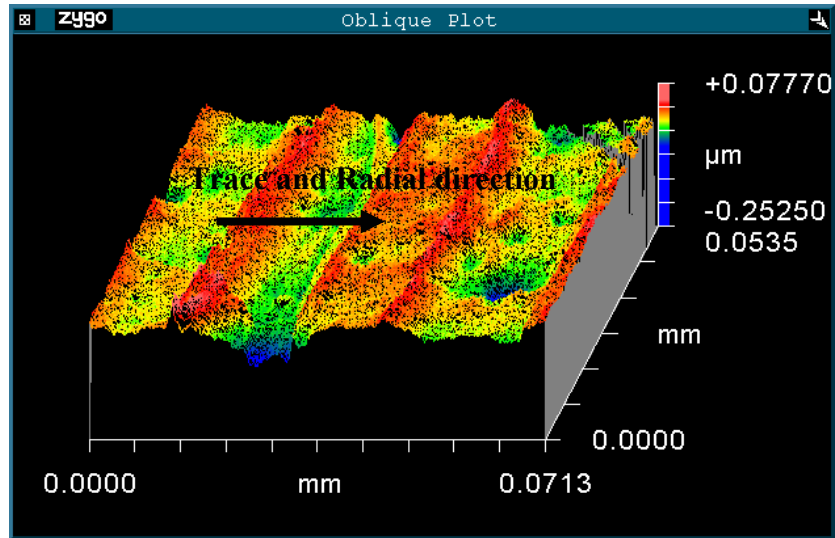


Figure 5-17. SWLI image of the flat cut with physical damping added to the system. The spindle speed was 400 rpm and the federate was 0.84 mm/min. The tool nose radius was 1 mm.

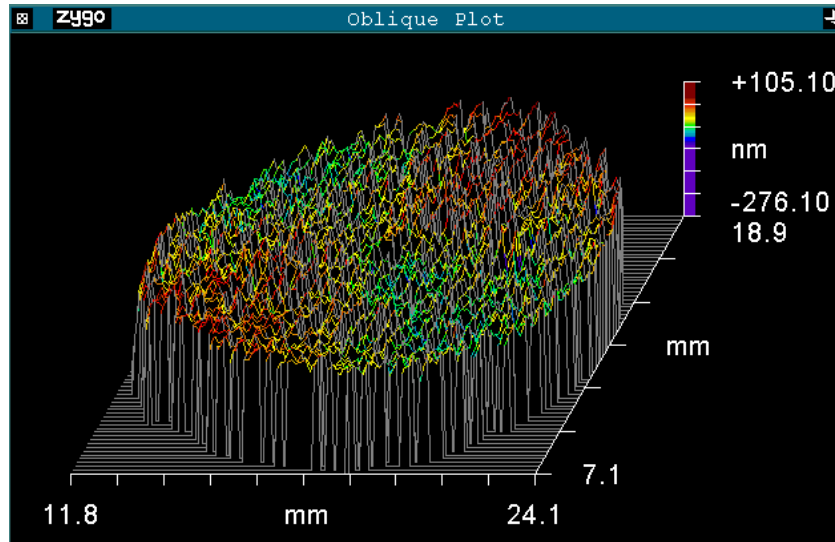


Figure 5-18. Laser interferometry image of the flat cut with the damped LAT system.

The spindle speed was 400 rpm and the federate was 0.84 mm/min.

While the surface finish of the part created with the damped LAT is slightly better than that created with the undamped LAT, the difference is not significant and cannot be conclusively attributed to the damping. In this experiment, encoder noise and noise in the amplifier loop were the limiting factors for surface finish and must be reduced before an accurate assessment of the damped vs. undamped system can be made.

5.6 Aluminum Tilted Flats

The one inch diameter aluminum tilted flats were cut with a tool excursion of 2 mm (peak to valley) at 5 Hz (300 rpm). The finish pass feedrate was 6 $\mu\text{m}/\text{rev}$ and the depth of cut was 5 μm . These parameters represent a theoretical PV surface value of 4.5 nm (1.5 nm Ra). The diamond tool had a 1 mm radius.

Undamped Tilted Flat Figure 5-19 shows a 50 X 70 μm SWLI image of the surface of the tilted flat cut without damping. The surface finish is 24 nm (Ra). Frequency domain data (Figure 5-20) shows a small part of the error (0.012% of the tool amplitude) occurs near 110 Hz, which is the natural frequency of the Z-axis (demonstrated in Section 2.10). Motion was also noticed around 150 Hz and 180 Hz frequencies, the same as seen during the controller tuning (Section 4.3.2). However, as with the copper flats, the observed PV motion of the slide during position holding (roughly 200 nm - Figure 5-14) is the limiting factor in achieving better finishes

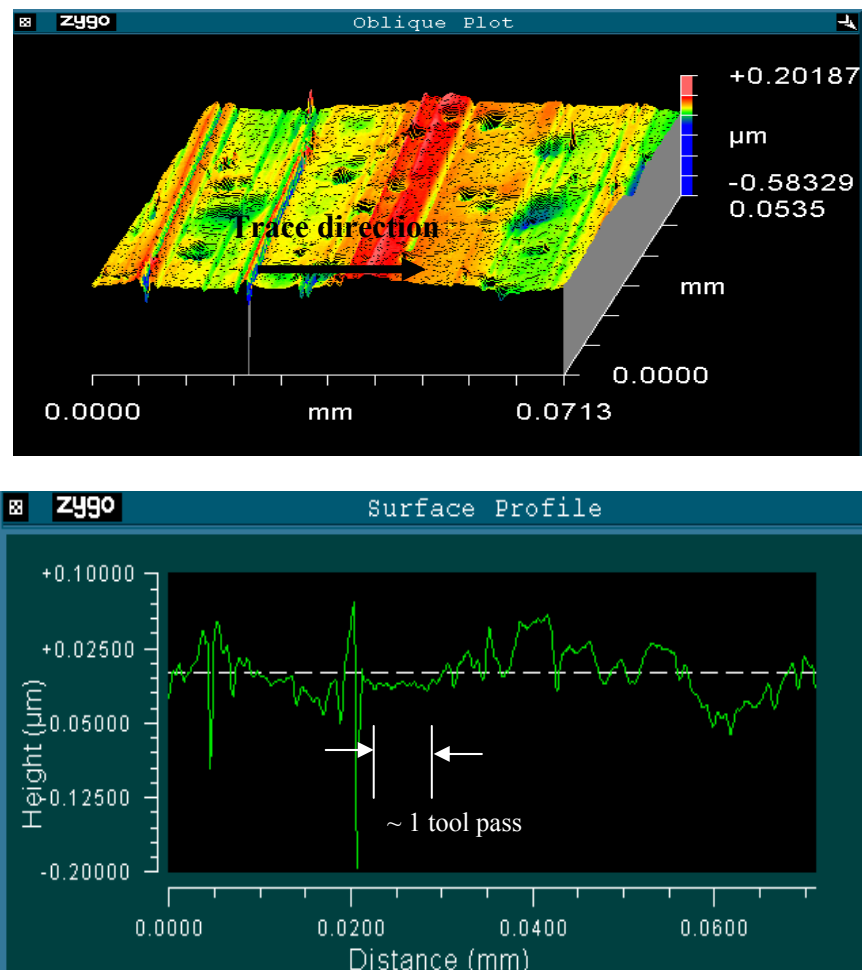


Figure 5-19. Surface of the undamped tilted flat. The part was cut at 300 rpm with a federate of 1.8 mm/min. The tool radius was 1 mm.

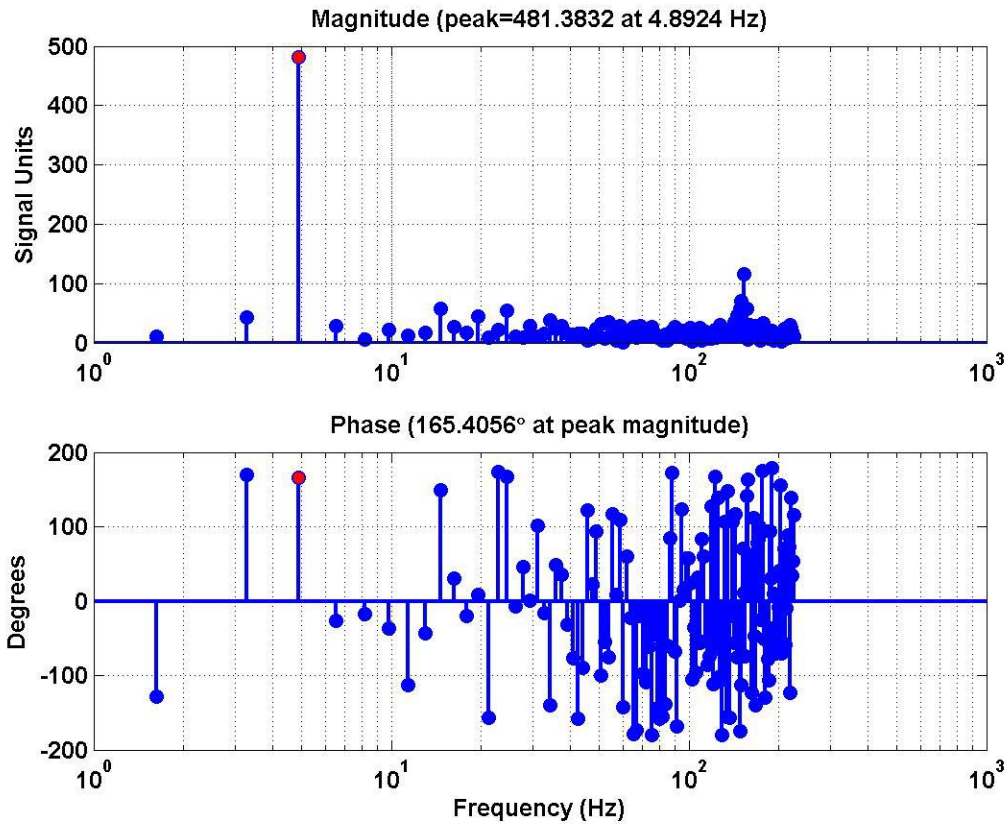


Figure 5-20. FFT data of the LAT motion during cutting. A frequency of 150 Hz is noticed, as was seen in the controller tuning.

Due to large undulations in the surface, interferometry was not available to analyze the part, so the CMM and Talysurf were used. A surface map of the part from the CMM is shown in Figure 5-21. The top left plot shows an isometric view of the surface, the top right plot shows the part error aligned with the surface and the bottom shows the error from a more revealing isometric view.

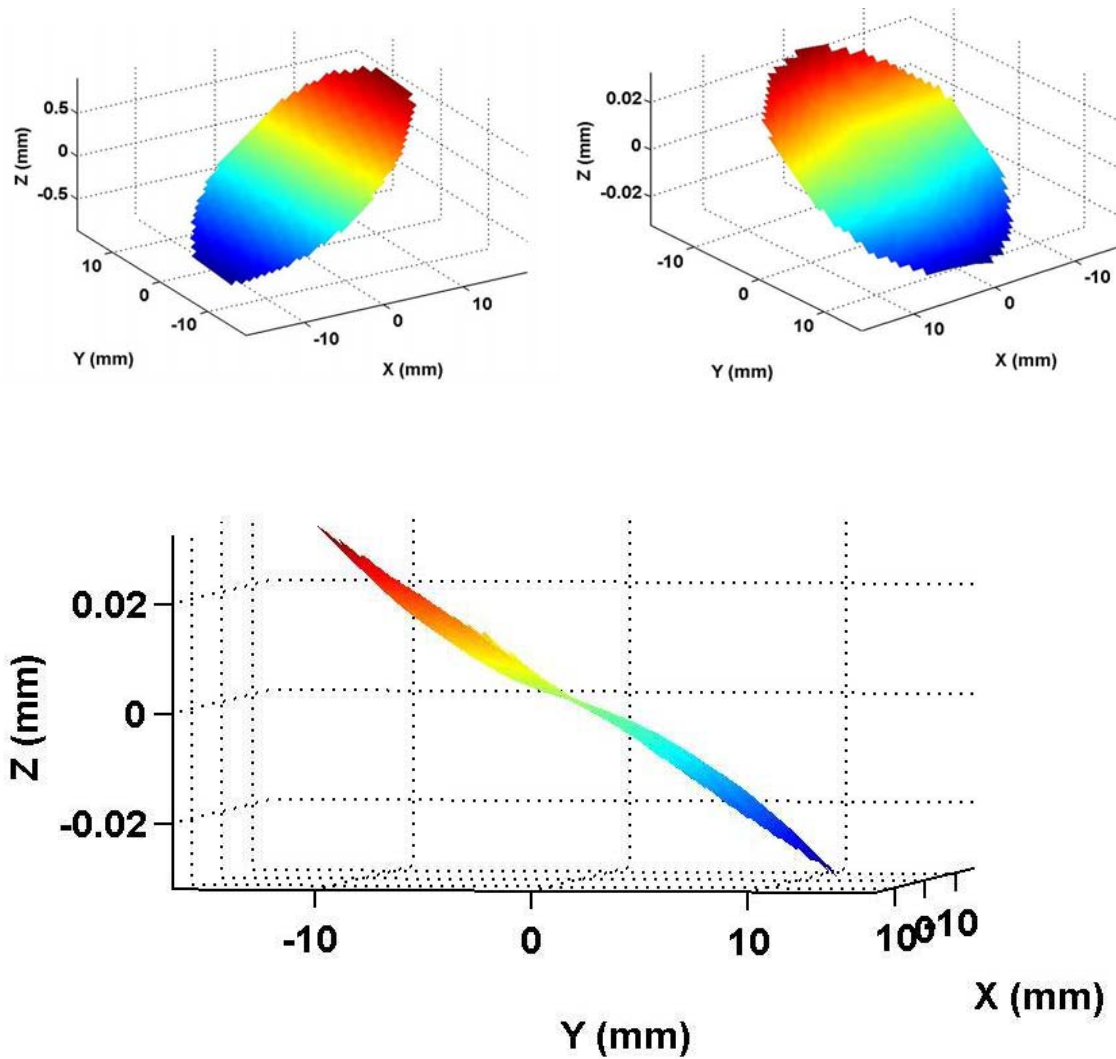


Figure 5-21. Surface of the undamped aluminum tilted flat measured by the CMM. The top left plot is an isometric view of the surface. The top right plot shows the surface figure error (best fit plane residual), and the bottom plot is a side view of the error.

A large hump and valley, roughly 10 μm each (20 μm PV relative to the surface), was measured on the surface using the Talysurf. These features may be due to changing phase lag throughout the cut.

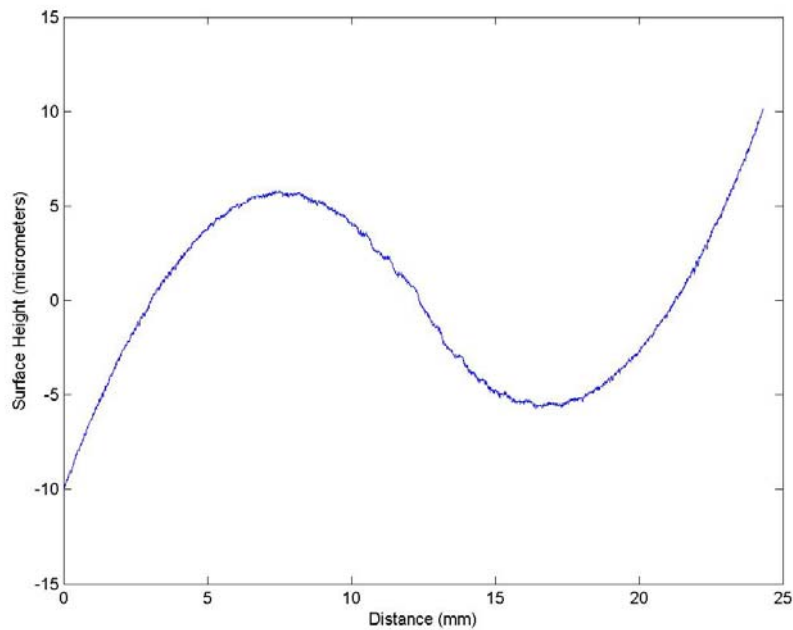


Figure 5-22. Talysurf trace from the low edge to the high edge of the undamped aluminum tilted flat with the slope taken out. The “hump and valley” shape confirms the CMM data in Figure 5-20.

In a linear system, the phase lag is independent of the amplitude. However, nonlinearities in the LAT system would make its phase lag amplitude dependent, producing the figure error characteristics shown in Figure 5-21. Figure 5-23 shows a theoretical tilted flat with a phase angle of 2 degrees at the OD (max amplitude) that decreases linearly to zero degrees at the center of the part. The top left plot is the surface of the theoretical tilted flat. The top right is the error and the bottom is a side view of the error. The theoretical flat with varying phase error has the same characteristic shape as the aluminum tilted flat cut during the machining experiment. It should be noted that the largest error magnitude (of the top right plot) is at right angles to the tilted surface (top

left plot). This is because the error is proportional to velocity and that is 90 degrees out of phase with the displacement.

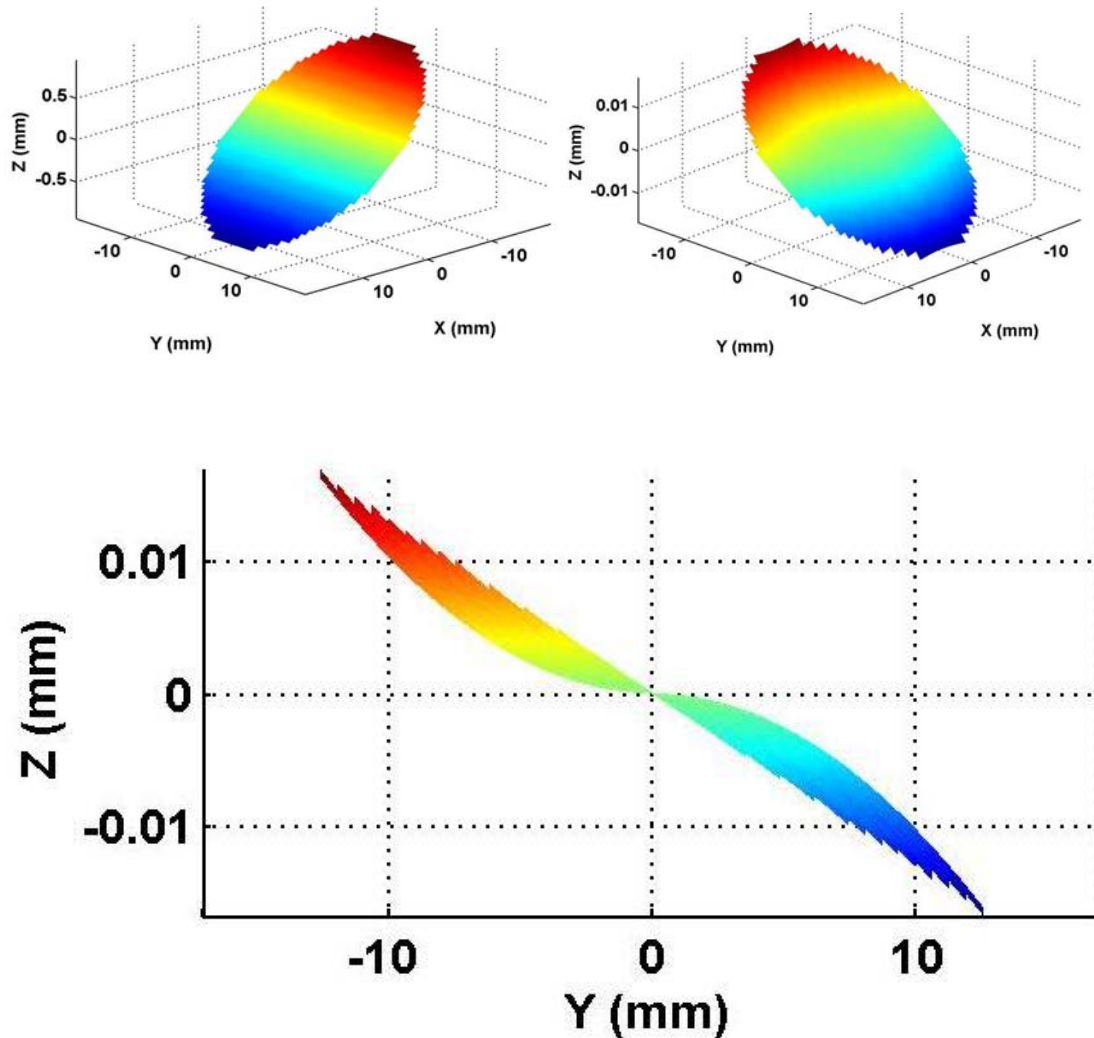


Figure 5-23. Theoretical tilted flat with linearly varying phase lag throughout the cut. Theoretical tilted flat surface (top left), error (top right) and side view of the error (bottom). The shape is the same as that seen in the undamped aluminum flat.

A method developed at the Precision Engineering Center known as deconvolution [28] could greatly improve the LAT's performance. This process essentially modifies the input command to a nonlinear system based on the known system dynamics. The system

then, by its natural behavior, shapes the command in a known way, resulting in the ideal output. Use of the deconvolution should be examined in future experiments with the LAT axis.

Damped Tilted Flat Figure 5-24 shows a 50 X 70 μm section of the surface of the tilted flat cut with the damped system. The same cutting parameters used for the undamped tilted flat were used for the damped tilted flat. The surface finish is 20 nm, 4 nm better than the undamped piece. Again, a frequency component was observed during cutting near the natural frequency of the Z-axis, but the main contribution to surface roughness remains the PV motion of the slide during position holding.

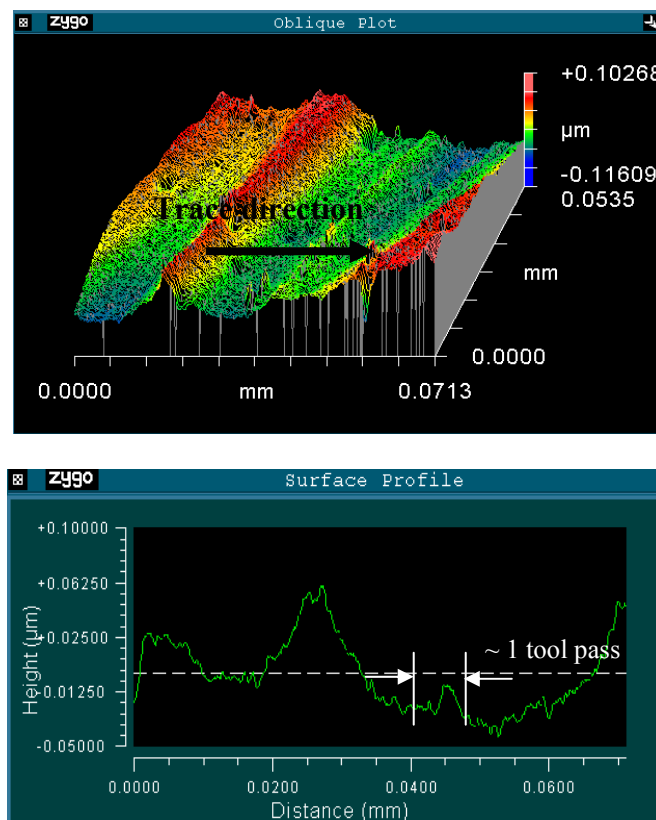


Figure 5-24. Surface of the tilted flat cut with damping added to the system. The spindle speed was 300 rpm and the feedrate was 1.8 mm/min.

Figure 5-25 shows the surface of the tiled flat and surface error as measured by the CMM. The error has the same characteristic shape as the undamped tilted flat due to varying phase lag, and the Talysurf (Figure 5-25) confirmed the PV error relative to the surface is $20\ \mu\text{m}$, same as the undamped part.

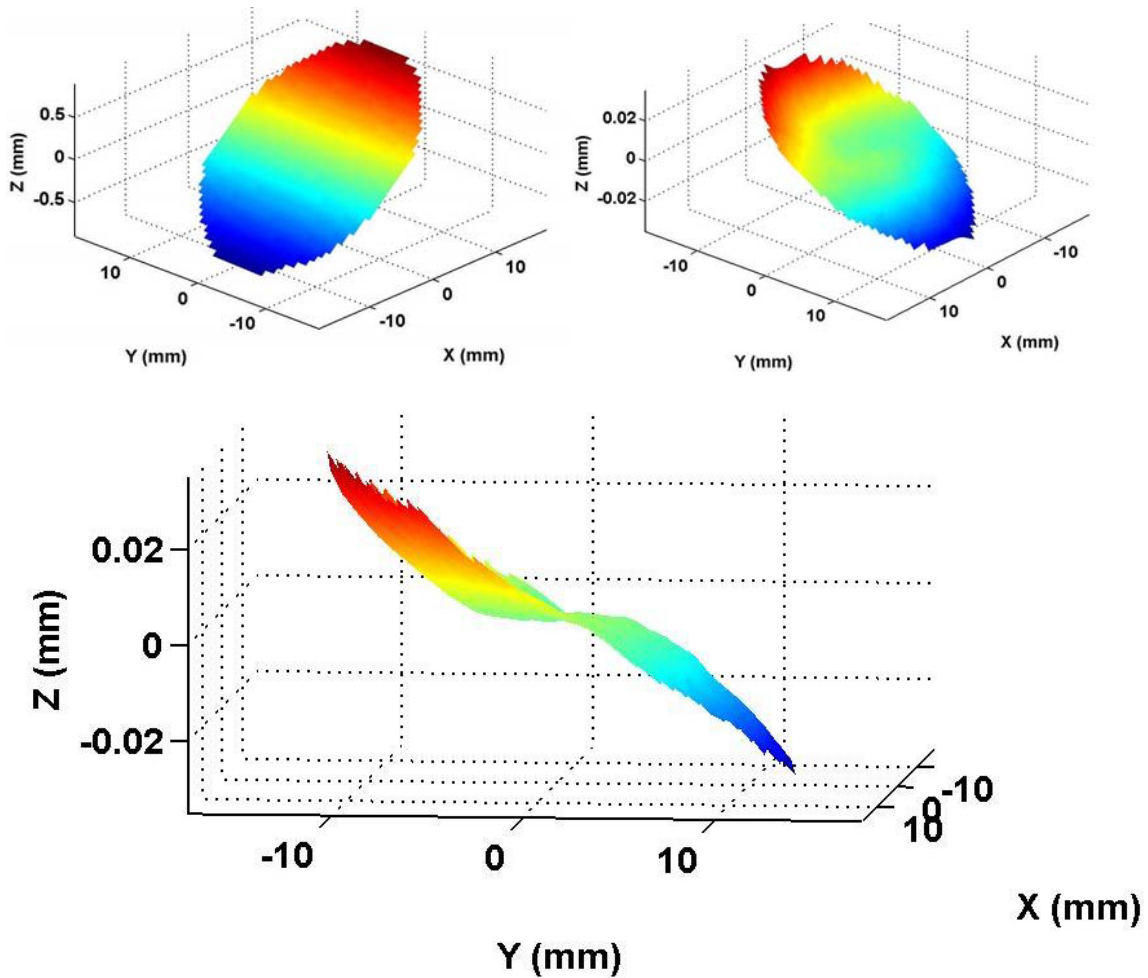


Figure 5-25. (Top) Surface of the damped aluminum tilted flat as measured by the CMM. (Top right) Error in the tilted flat and side view of error (bottom). The error has the same shape as that for the undamped tilted flat and is due to varying phase lag.

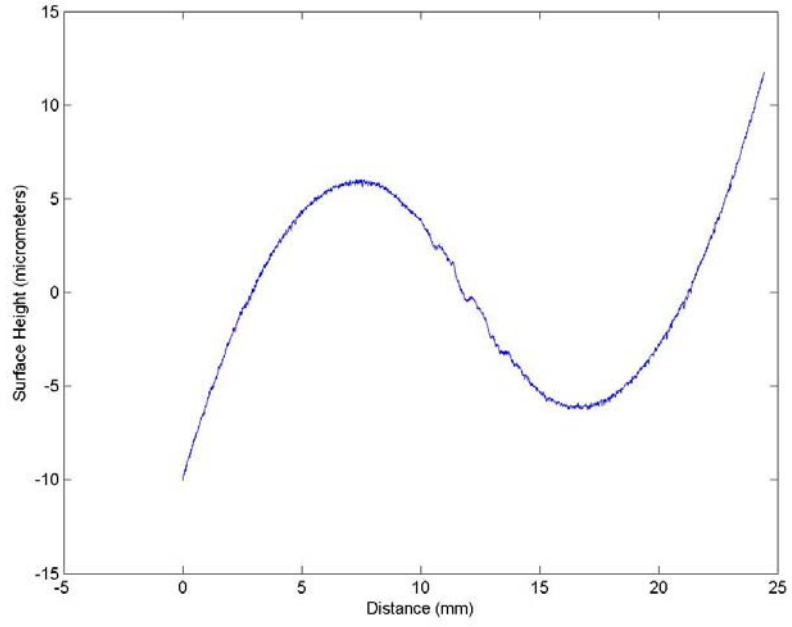


Figure 5-26. Talysurf trace from the low edge to the high edge of the undamped aluminum tilted flat with the slope taken out.

6 Conclusions and Future Work

- The Live-Axis Turning (LAT) system was designed and fabricated to create non-rotationally symmetric optical surfaces. It fits between the large amplitude slow-slide servo and the low amplitude piezoelectric fast tool servo. The features of this design are:
 - The moving component is a 500 gram aluminum honeycomb slide with a triangular cross-section. A diamond tool is mounted to the slide on a lightweight tool post.
 - The slide is guided on all sides by an air bearing housing. A window in the top of the housing allows an optical linear encoder to monitor the slide position and report it to the control system.
 - The system is driven by a brushless permanent magnet linear motor attached to the slide by a stiff, lightweight bracket.
 - A viscous damper was added to the system to examine the affect of damping on system performance.
- A Simulink model was created to simulate the performance of the system. This model was verified experimentally and used to design the system's closed loop controller.
- The control scheme was implemented using a Delta Tau UMAC Turbo controller and the entire system was integrated onto the Nanoform 600 diamond turning machine.

- The LAT system's ability to hold position was observed by machining copper flats. These parts had a surface finish of 14 nm and were flat to $\frac{1}{2}$ wave (321 nm).
- The dynamic capabilities of the system were tested by machining aluminum tilted flats. During cutting, the system followed a 2 mm peak-to-peak sine wave at 5 Hz. The parts had a surface finish of 24 nm (Ra) and a PV flatness of 20 μm .
- Although the value of added physical damping was shown theoretically, machining experiments showed no significant improvement in the performance of the damped system. Amplifier source noise was the main cause of this finding.

Future work for this project includes further refining this design and eventually creating a commercially viable device. Some possible specific system improvements are listed below.

- A less noisy source for the amplifier. The existing source produced a PV total of 525 mV at 10.75 KHZ. This voltage corresponds to nearly 0.5 N of unwanted force and negatively affected surface finish during machining.
- Reading LAT axis position with a laser interferometer and integrating a controller with a quicker update rate would help signal following and fine positioning. This would make the axis more accurate at longer ranges and higher frequencies and greatly reduce the encoder noise that hindered the current system's performance.
- The deconvolution algorithm developed at the PEC [28] could be used to shape inputs to the LAT to minimize the effect of system nonlinearities.

References

1. Bingham, Walker, et al., "A novel automated process for aspheric surfaces," SPIE *International Symposium on Optical Science and Technology - Proceedings*, June 2000.
2. Jones, R.A., "Fabrication of small nonsymmetrical aspheric surfaces," *Applied Optics*, Vol.18 Issue 8 Page 1244 (April 1997)
3. Schaeffer, "Progress in Precision," 2002 ASPE Spring Topical Meeting
4. Franse, J, "Manufacturing techniques for complex shapes with submicron accuracy," *Reports on Progress in Physics*, Vol. 53, No. 8 (August 1990)
5. Precitech, Inc. "Innovations in Technology," *Precitech Newsflash*, V.1.03, Feb 2003. <http://www.precitech.com/pages/nwsflashFEB.htm>
6. United States patent No. 5,467,675. Apparatus and method for forming a workpiece surface into a non-rotationally symmetric shape, November 21, 1995. Thomas A. Dow, Kenneth P. Garrard, George M. Moorefield, II and Lauren W. Taylor.
7. Falter, PJ, "Diamond Turning of Nonrotationally Symmetric Surfaces," Ph.D. Dissertation, North Carolina State University, 1990
8. Jared, B, "The Design and Documentation of a Fast Tool Servomechanism for the Production of Inertial Confinement Fusion Targets," MS Thesis, North Carolina State University, 1996
9. Montesanti, R. C., and Trumper, D.L., "High-Bandwidth Short-Stroke Rotary Fast Tool Servo," 2003 Annual Meeting of the ASPE, Portland, OR, October, 25-30, 2003
10. Trumper, D.L., and Lu, X-D, "Electromagnetically-Driven Ultrafast Tool Servo," 2003 Annual Meeting of the ASPE, Portland, OR, October, 25-30, 2003
11. K. Garrard, A. Sohn, R. G. Ohl, R. Mink, V. J. Chambers."Off-Axis Biconic Mirror Fabrication," *Proceedings from the EUSPEN 2002 Annual Meeting* (2002).
12. Hexcel HexWeb Honeycomb Sandwich Design Technology. www.hexcel.com
13. Young, Warren C. and Budynas, Richard G. Roark's Formulas for Stress and Strain, 7th Edition. McGraw-Hill, 2002.

14. Airex P12-1 Linear motor specifications. www.airex.com
15. Stampfli, H. "Brushless Linear Motors," <http://www.motionsystemdesign.com>
16. Lavenuta, Greg. "Negative Temperature Coefficient Thermistors: Characteristics, Materials, and Configurations," www.designinfo.com/cornerstone/ref/negtemp.html
17. Peters, Randall D. "Damping: Background and Theory." Mercer University, <http://physics.mercer.edu/hpage/damping.htm>
18. Shigley, Joseph E. Mechanical Engineering Design, 6th Edition. McGraw-Hill, 2001.
19. Ogata, Katsuhiko. Modern Control Engineering, 4th Edition. Prentice Hall, 2002.
20. Alerich, Walter N. Electric Motor Control, 4th Edition. Delmar Publishers, Inc, 1998.
21. McIntyre, R. L. Electric Motor Control Fundamentals, 3rd Edition. McGraw-Hill, 1974.
22. Dewitt, David P. and Incropera, Frank P. Introduction to Heat Transfer, 4th Edition. John Wiley & Sons, 2002.
23. Dahleh, Marie Dillon and Thomson, William T. Theory of Vibration with Applications, 5th Edition. Prentice Hall, 1998.
24. Dow, Thomas A. and Sohn, A. "Metrology in Precision Manufacturing – Course Notes."
25. Rao, Singiresu S. Mechanical Vibrations, 3rd Edition. Addison-Wesley, 1995.
26. "Software Reference Manual: Turbo PMAC/PMAC2," August 2004. <http://www.deltatau.com/fmenu/TURBO%20SRM.PDF>
27. Kobayashi, A. Machining of Plastics. Robert E. Krieger Publishing Company, 1981.
28. Panusittikorn, W. "Error Compensation Using Inverse Actuator Dynamics." PhD. Dissertation, North Carolina State University, 2004.
29. Batchelor, G. K. An Introduction to Fluid Dynamics. Cambridge at the University Press, 1967.

30. OE – The SPIE Magazine of Photonics Technologies and Applications. “Eye on Technology: Polishing on the Edge.” March 2001.
<http://oemagazine.com/fromTheMagazine/mar01/eyeontech.html>

Appendix

Appendix A – Honeycomb Deflection Equations

Honeycomb material was used in this project because of its very low weight, high stiffness, and durability. To model a system with components made of aluminum honeycomb, it is first important to understand all properties of this material. It is more difficult to model than normal materials because it is a composite, usually made of 2 thin plates of aluminum separated by a honeycomb material (as shown below in Figure A-1).

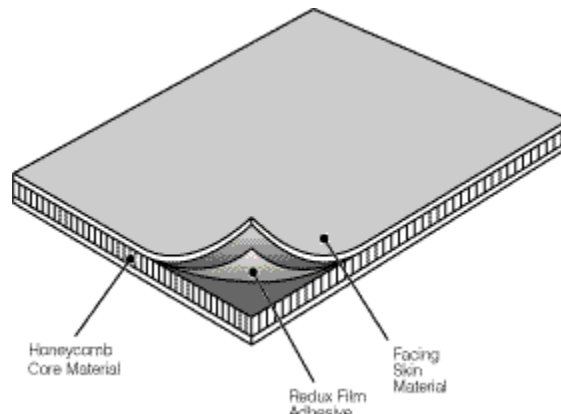


Figure A-0-1. The make-up of a honeycomb composite. In this application, the facing skin material is aluminum.

One of the most important properties of the honeycomb is bending stiffness, which will affect component deformation as well and natural frequency of the system. A way to understand the material's stiffness is to look at the relationship between applied load and total deflection. The total deflection of is the combined effect of bending and shear deflection.

The bending deflection (Figure A-2) depends on the relative tensile and compressive moduli of the skin material, while the shear deflection (Figure A-3) depends on the shear modulus of the core. Therefore the total deflection in a beam is given by equation A-1.

$$\delta_{total} = \delta_{bending} + \delta_{shear} \quad (A-1)$$

The shear term is where a honeycomb beam differs considerably from a solid beam. For sizes where the length is much larger than the height, the shear deflection can essentially be neglected for a solid beam. In a honeycomb beam, however, the shear modulus of the core is so low the shear deflection cannot be ignored.

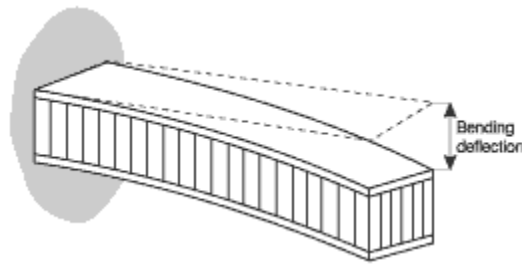


Figure A-0-2. Honeycomb beam deflection due to bending.

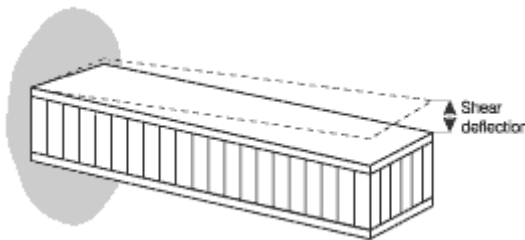


Figure A-0-3. Honeycomb beam deflection due to shear.

Bending Deflection - The bending deflection depends on the beam's cross-section, the loading setup, material properties, and is proportional to the cube of the beam's length.

$$\delta_{bending} = \frac{K_b P l^3}{D} \quad \text{where } D = \frac{E_f t_f (t_f + t_c)^2 b}{2}$$

K_b = Beam – bending deflection coefficient

P = Applied load

l = Beam span

E_f = Modulus of elasticity of facing skin

t_f = Thickness of facing skin

t_c = Thickness of core

b = Beam width

(A – 2)

The deflection due to bending can be found by using Equation A-2. Beam coefficients are given in Table A-1.

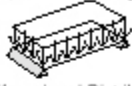
BEAM TYPE	MAXIMUM SHEAR FORCE F	MAXIMUM BENDING MOMENT M	BENDING DEFLECTION COEFFICIENT k_b	SHEAR DEFLECTION COEFFICIENT k_s
$P = q / b$ Simple Support  Uniform Load Distribution	$\frac{P}{2}$	$\frac{Pl}{8}$	$\frac{5}{384}$	$\frac{1}{8}$
$P = q / b$ Both Ends Fixed  Uniform Load Distribution	$\frac{P}{2}$	$\frac{Pl}{12}$	$\frac{1}{384}$	$\frac{1}{8}$
 Central Load Simple Support	$\frac{P}{2}$	$\frac{Pl}{4}$	$\frac{1}{48}$	$\frac{1}{4}$
 Central Load Both Ends Fixed	$\frac{P}{2}$	$\frac{Pl}{8}$	$\frac{1}{192}$	$\frac{1}{4}$
$P = q / b$ One End Fixed (Cantilever)  Uniform Load Distribution	P	$\frac{Pl}{2}$	$\frac{1}{8}$	$\frac{1}{2}$
 Load One End One End Fixed (Cantilever)	P	Pl	$\frac{1}{3}$	1
$P = \frac{q / b}{2}$ One End Fixed (Cantilever)  Triangular Load Distribution	P	$\frac{Pl}{3}$	$\frac{1}{15}$	$\frac{1}{3}$

Table A-1. Summary of beam coefficients.

As seen from the equation, a long beam deflects much more than a short one, and a thick beam will stay much more rigid than a thin one.

Shear Deflection - Shear deflection in a beam depends on the type of loading, geometry of cross-section, and varies linearly with the length. These relationships are shown in Equation A-3.

$$\delta_{shear} = \frac{K_s Pl}{S} \quad \text{where } S = bhG_c$$

K_s = Beam – shear deflection coefficient

P = Applied load

l = Beam length

b = Beam width

h = Distance between facing centers

G_c = Core shear modulus

(3)

The process and values used in this application are shown on the following page.

Aluminum Honeycomb Beam Deflection/Stiffness

Beam length (in.)	L=	6
Beam width (in.)	w=	1.875
Core width (in.)	w _c =	1.875
Face thickness (in.)	t _f =	0.04
Core thickness (in.)	t _c =	0.75
Face material modulus (psi)	E _f =	10000000
Core shear modulus (psi)	G=	44000
Beam bending deflection coefficient	K _b =	0.020833
Beam shear deflection coefficient	K _s =	0.25

Effective Moment of Inertia (in ⁴)	I=	0.023424
--	----	----------

Deflection Calculations

$$\delta_{bending} = K_b \frac{PL^3}{E_f I}$$

$$\delta_{shear} = K_s \frac{PL}{b(t_f + t_c)G}$$

Load (lb) P=	50
--------------	----

Deflection due to bending (in.)	d _{bending} =	0.000961
Deflection due to shear (in.)	d _{shear} =	0.001151
Total Deflection (in.)	d _{total} =	0.002111

Stiffness Calculations

$$\frac{P}{\delta} = \left[K_b \frac{L^3}{E_f I} + K_s \frac{L}{b(t_f + t_c)G} \right]^{-1}$$

Stiffness (lb/in.) P/δ=	23681.96242
-------------------------	-------------

This information can be found in more detail at:

www.hexcel.com/NR/rdonlyres/80127A98-7DF2-4D06-A7B3-7EFF685966D2/0/7586_HexWeb_Sand_Design.pdf

Appendix B – Bearing Stiffness

The following is a copy of the spreadsheet used to analyze the stiffness due to the bearing in the slide length analysis.

Total Bearing Stiffness	1.30E+06 lb/in	Moment of inertia (I)	0.56 in ⁴
Bearing Length (L)	5.5 in	Elastic modulus (E)	1.00E+07 psi
Bearing stiffness per unit length (k _o)	2.36E+05	*take beam of unit width (b _o =1 in)	

$$\beta = \left(\frac{b_o k_o}{4EI} \right)^{1/4} \quad \beta = 0.320504 \text{ in}^{-1}$$

Now explore sensitivity of moment stiffness to bearing length and moment of inertia.

From Roark, 6th ed., pg. 144, moment stiffness if found (for free-free case) to be M_o/θ_a (for a=0)

$$\frac{M_o}{\theta_a} = EI\beta \frac{C_{11}}{C_3 C_{a4} + C_2 C_{a1}}$$

$$C_{11} = \sinh^2 \beta L - \sin^2 \beta L$$

$$C_3 = \sinh \beta L \sin \beta L$$

$$C_{a4} = \cosh \beta(L-a) \sin \beta(L-a) - \sinh \beta(L-a) \cos \beta(L-a)$$

$$C_2 = \cosh \beta L \sin \beta L + \sinh \beta L \cos \beta L$$

$$C_{a1} = \cosh \beta(L-a) \cos \beta(L-a)$$

L (in)	C ₁₁	C ₃	C _{a4}	C ₂	C _{a1}	Moment Stiffness (lb*in/μrad)
4.5	3.0042061	1.98047	1.95895	2.470871	0.286259	1.176
5.5	7.0368048	2.776537	3.48462	2.405284	-0.572405	1.522
7	21.105894	3.644864	6.63172	0.823944	-2.969994	1.744

Appendix C – Linear Motor Theory of Operation

A brushless linear DC motor is used to drive the slide in this application. The theory behind this type of motor will be discussed in this section.

Synchronous motors have two components – a rotor and a stator. The stator is the stationary component and the rotor moves. One of these parts consists of permanent magnets (or fixed electromagnets) while the other is made up of switching electromagnets. The components of a basic rotary motor are shown in Figure C-1.

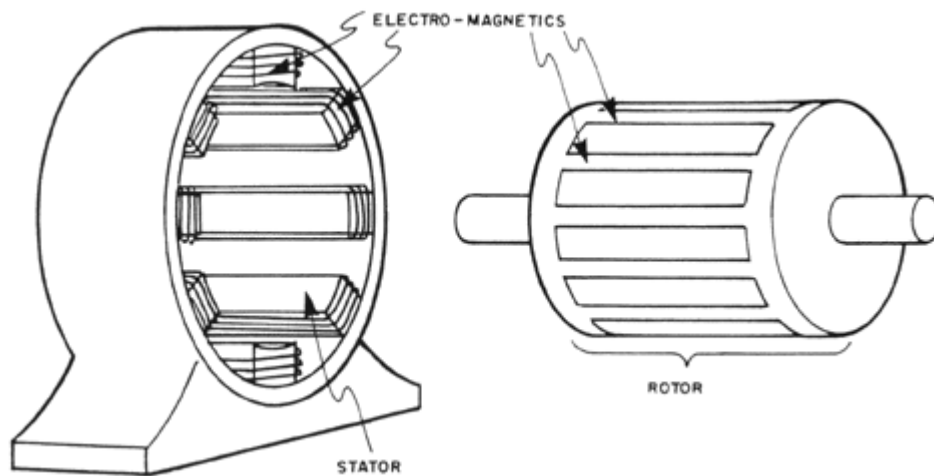


Figure A-0-4. The rotor and stator of a basic rotary motor.

Because unlike magnetic poles attract each other and like poles repel, progressively changing the polarity of the stator poles (in this example) so the magnetic field rotates will result in the rotor “chasing” the field and thus, rotating. This sequence is displayed in Figure A-5. The magnetic field of the stator (outside ring) is rotating clockwise, and the fixed pole rotor (inner bar) is being dragged along, causing clockwise rotation of the shaft (out of the page).

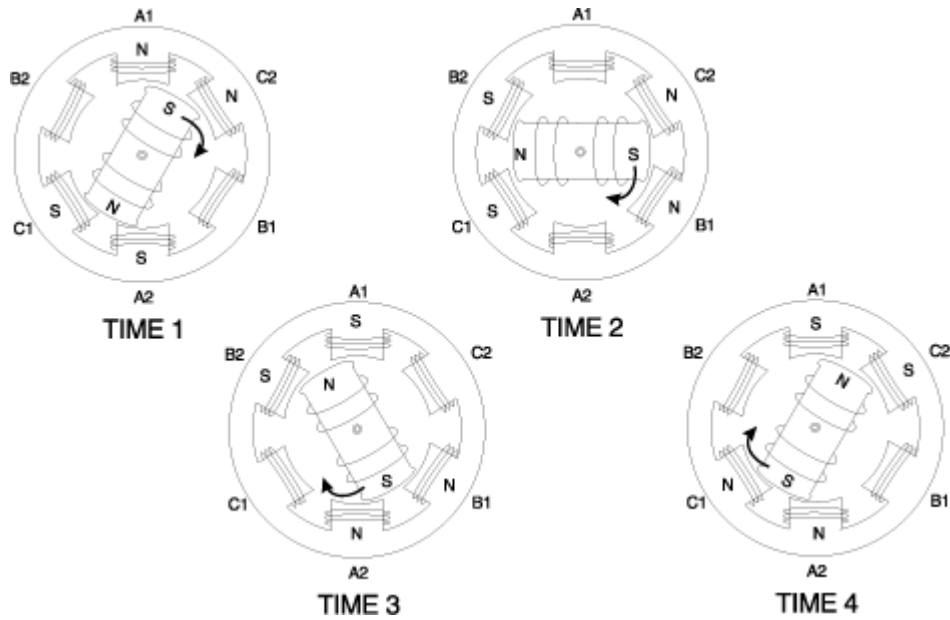


Figure A-0-5. Pole-switching sequence for rotary motor rotation.

One way to produce the rotating magnetic field is to use a three-phase power supply. This entails sending current in three sine waves, 120° apart, to the electromagnets of the stator. An example is shown in Figure A-6.

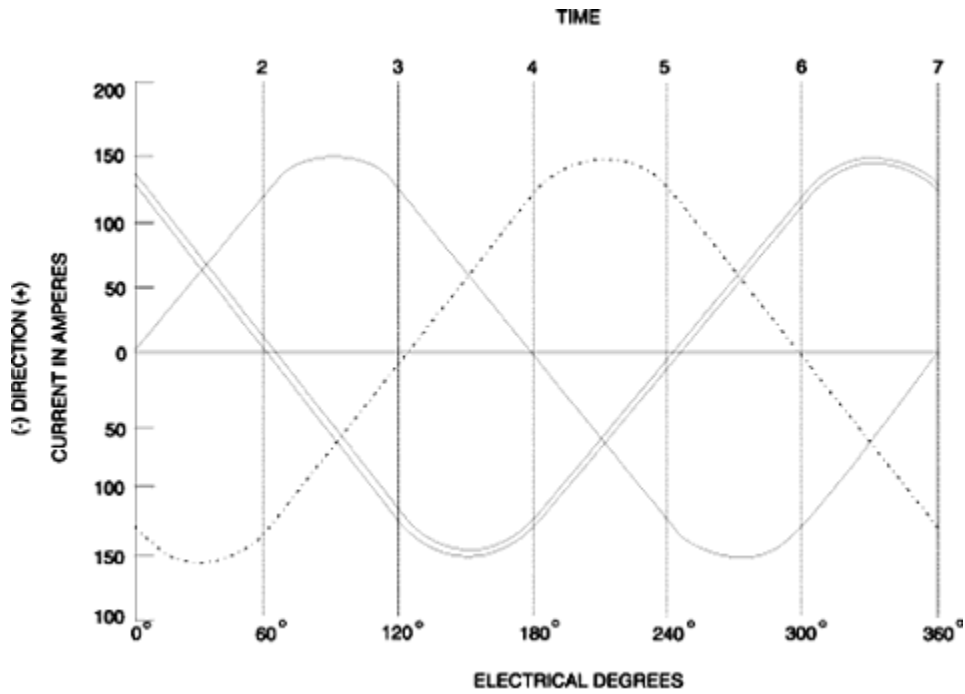


Figure A-0-6. Three phase power. The plot shows Current vs. Time.

A linear motor operates with the same principles. In fact, it's essentially a rotary motor that has been “unrolled.” This principle is shown in Figure A-7

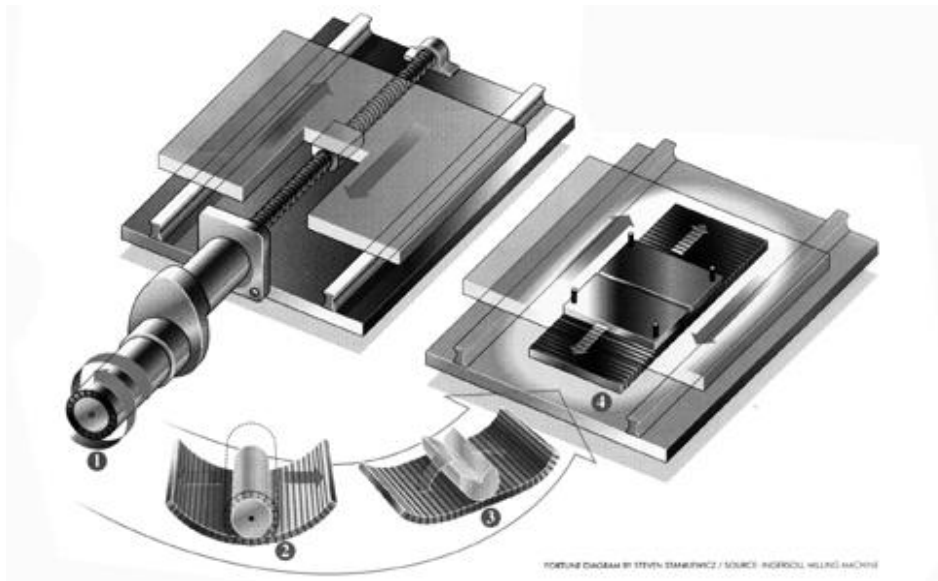


Figure A-7 – A rotary motor unrolled into a linear motor.

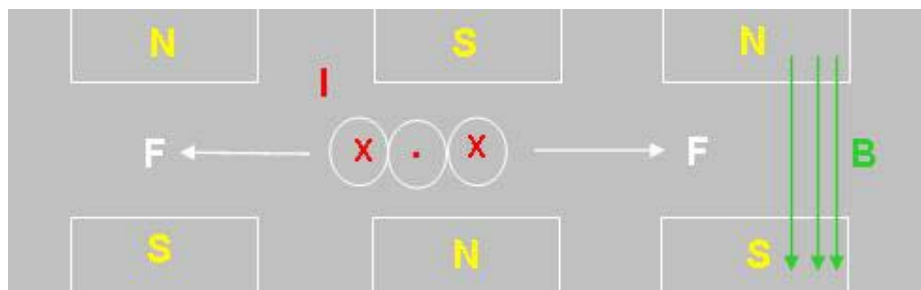
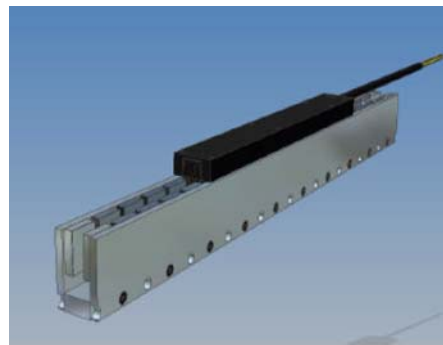


Figure A-0-7. Linear motor 3D view (top). Motor schematic, viewed from above (bottom).

Figure A-8 shows a top view of the actual motor and magnet track used in this application. The blocks marked with “N” and “S” represent the permanent magnets of the track, and the three circles in the center represent the motor coils. In this case, the magnet track is the stator and the motor coil acts as the rotor, or moving component. The symbols inside the coils (circles) represent the direction of current flow, where “X” indicates flow into the page and “.” indicates flow out of the page. When the current interacts with the magnetic field, a force is created. This force, F , is proportional to the amount of current, I , the magnetic field strength, B , and the length of the wire wrappings in the coils, l . By switching the direction of current flow in the coils at precisely the right time (sine wave commutation), the motor can be pushed and pulled down the track. For more information on three-phase power, visit <http://mcu.st.com/contentid-7.html>.

Appendix D – Airex P12 – 1 Linear Motor Specifications

P12 Motor Data

Route 108, Dover, NH 03820

Tel: 603.742.3703 Fax: 603.742.0977 <http://www.airex.com/>

The Smallest Brushless Linear Servo Motor designed for Advanced Motion Applications

Designed for today's most advanced applications, Airex Brushless Linear Servo Motors offer the absolute best in linear motion technology. Airex patented machine winding technology produces motors with exceptional performance, smooth motion, high accuracy, unmatched unit-to-unit repeatability, high acceleration, and stiffness. Used in high precision processing equipment, these motors meet and exceed the rigorous demands required in today's mfg, assembly, test and inspection environments. Applications include multi-tiered stages, semiconductor mfg, inspection systems, micro - machining equipment, optical scanning devices, laser machining, and electrical component testing. The P12 is a standard design in the Solution Series linear motor family. Airex also offers custom designs in ironless rotary and linear configurations.

FEATURES:

- ***CONTINUOUS FORCE UP TO 24 LBS.***
- ***PEAK FORCE UP TO 76 LBS.***
- ***HIGHEST FORCE TO COIL MASS RATIO***
- ***HIGH ACCURACY/REPEATABILITY***
- ***EFFICIENT THERMAL PERFORMANCE***
- ***VELOCITIES > 3 M/SEC ACCELERATIONS > 5 G***
- ***ZERO MAGNETIC PRELOAD***
- ***SINUSOIDAL OR HALL EFFECT COMMUTATION***
- ***POSITIVE OR NEGATIVE COEFFICIENT THERMISTORS***
- ***HIGH PERFORMANCE RARE EARTH MAGNETS***
- ***LOW INDUCTANCE COIL FOR FAST RESPONSE***
- ***NON-CONTACTING ASSEMBLIES***
- ***CONTINUOUS TRACK TO 48 INCHES***
- ***CONFIGURABLE CONNECTIONS/CABLE OPTIONS***
- ***FULLY CUSTOMIZABLE DESIGN***

	UNITS	P12-1	P12-2	P12-3	P12-4
COIL LENGTH	INCHES [MM]	2.4 [61.0]	4.8 [122.0]	7.2 [182.9]	9.6 [243.8]
BRACKET LENGTH *	INCHES [MM]	3.6 [91.4]	6.0 [152.4]	8.4 [213.4]	10.8 [274.3]
COIL WEIGHT	LBS [KG]	0.22 [.10]	0.44 [.20]	0.66 [.30]	0.88 [.40]
MAGNET TRACK WEIGHT	LBS/FT [N/CM]	2.0 [3.0]	2.0 [3.0]	2.0 [3.0]	2.0 [3.0]
MAX. WINDING TEMPERATURE	°C	125	125	125	125
Series Connected Coils					
FORCE CONSTANT	LBS [N]/AMP	2.0 [8.9]	4.0 [17.8]	6.0 [26.7]	8.0 [35.6]
COIL RESISTANCE ** (@25° C. AT MOTOR)	OHMS	1086	21.72	32.58	43.44
PHASE RESISTANCE ** (@25° C. IN DELTA)	OHMS	7.24	14.48	21.72	28.96
COIL RESISTANCE ** (@125° C. AT MOTOR)	OHMS	1637	32.30	48.46	64.61
PHASE RESISTANCE ** (@125° C. IN DELTA)	OHMS	1091	21.54	32.30	43.07
INDUCTANCE @ 1kHz	MH	1.98	3.96	5.94	7.92
CONTINUOUS FORCE	LBS [N]	6 [27]	12 [53]	18 [80]	24 [107]
CONTINUOUS CURRENT ***	AMPS	3.0	3.0	3.0	3.0
CONTINUOUS POWER (@125° C.)	WATTS	98	194	291	388
PEAK FORCE	LBS [N]	19 [84]	38 [169]	57 [253]	76 [338]
PEAK CURRENT ***	AMPS	9.5	9.5	9.5	9.5
PEAK POWER (@125° C.)	WATTS	982	1938	2907	3877
BACK EMF CONSTANT	V/IPS [V/MPS]	0.23 [9.06]	0.47 [18.50]	0.70 [27.56]	0.93 [36.61]
ELECTRICAL TIME CONSTANT **	MSEC	.18	.18	.18	.18
Parallel Connected Coils					
FORCE CONSTANT	LBS [N]/AMP	1.0 [4.45]	2.0 [8.9]	3.0 [13.34]	4.0 [17.79]
COIL RESISTANCE ** (@25° C. AT MOTOR)	OHMS	2.72	5.43	8.15	10.86
PHASE RESISTANCE ** (@25° C. IN DELTA)	OHMS	1.81	3.62	5.43	7.24
COIL RESISTANCE ** (@125° C. AT MOTOR)	OHMS	4.09	8.08	12.11	16.15
PHASE RESISTANCE ** (@125° C. IN DELTA)	OHMS	2.73	5.38	8.08	10.77
INDUCTANCE @ 1kHz	MH	0.50	0.99	1.49	1.98
CONTINUOUS FORCE	LBS [N]	6 [27]	12 [53]	18 [80]	24 [107]
CONTINUOUS CURRENT ***	AMPS	6.0	6.0	6.0	6.0
CONTINUOUS POWER (@125° C.)	WATTS	98	194	291	388
PEAK FORCE	LBS [N]	19 [84]	38 [169]	56 [253]	76 [338]
PEAK CURRENT ***	AMPS	19.0	19.0	19.0	19.0
PEAK POWER (@125° C.)	WATTS	982	1938	2907	3877
BACK EMF CONSTANT	V/IPS [V/MPS]	0.12 [4.53]	0.24 [9.25]	0.35 [13.78]	0.47 [18.31]
ELECTRICAL TIME CONSTANT **	MSEC	.18	.18	.18	.18

LINEAR MOTOR COIL	MOTOR SERIES	# OF POLES	COIL TYPE	INTERNAL CONNECTION	CABLE LENGTH	THERMAL DEVICE
L M C	- P 1 2	- 1	3	S	7 2	N
LMC	P12	1	1 = coil only	S = series	36 = 36 inches	X = none
	P15	2	3 = coil with 120° Hall Effect Device	P = parallel	180 = 180 inches	L = normally closed thermostat (P15 & P20)
	P20	3				F = normally open thermostat (P15 & P20)
		4				N = negative temp. coef. thermistor
		5 (P20 only)				P = positive temp. coef. thermistor
						C = temperature to current thermistor

LINEAR MOTOR TRACK	MOTOR SERIES	TRACK LENGTH	MAGNET	PROFILE
<u>L M D T</u>	- <u>P 1 2</u> -	<u>1 2 . 0</u>	<u>F</u>	<u>S</u>
LMDT	P12	25.2 = 25.2 inch [640.1mm]	F = standard for P12 & P15	S = standard
	P15	P12 & P15 available in 1.20 inch [30.5mm] increments	B = standard for P20 series	
	P20	P20 available in 2.40 inch [61.0mm] increments		

Appendix E – Transformed Area Method for Composites

The transformed area method was used to solve for the composite modulus of the motor coil. An outline of the setup and dimensions is given, and a step-by-step solution is explained. To do the analysis, a Maple Worksheet was used. Commands and answers from this worksheet are pasted directly into this Appendix.

For a simply supported beam,

$$\delta = \frac{WL^3}{48EI}$$

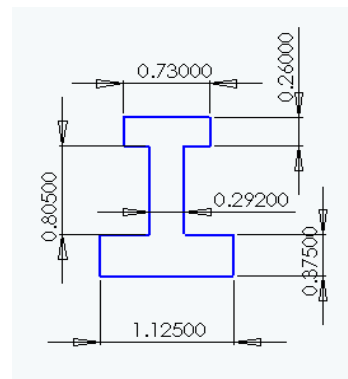
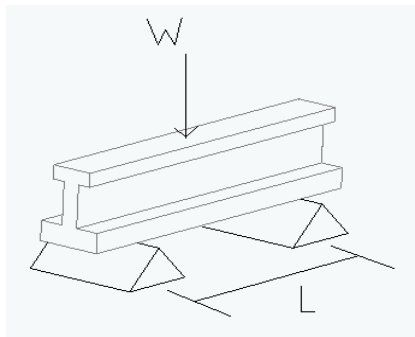
δ = beam deflection (in)

W = applied load (lb)

L = beam length (in)

E = material modulus of elasticity (psi)

I = moment of inertia about centroid of beam (in⁴)



For this setup,

$$L = 4.12 \text{ in.}$$

$$I = 0.18651 \text{ in}^4$$

W (lb)	δ (in)			Stiffness k** (lb/in)
	Test 1	Test2	Average	
5	0.00013	0.00012	0.000125	40000
10	0.0002	0.0002	0.0002	50000
15	0.00025	0.000263	0.000256	58537
20	0.0003	0.000313	0.000306	65306
25	0.00035	0.00035	0.00035	71429
30	0.000475	0.00045	0.000463	64865
35	0.0005	0.000488	0.000494	70886

** k = W/ δ

Average Stiffness: 60146 lb/in

Figure A-8 was used as the reference for this calculation, with the outer "C" shape pieces being aluminum and the inner "I" shape being epoxy/copper composite.

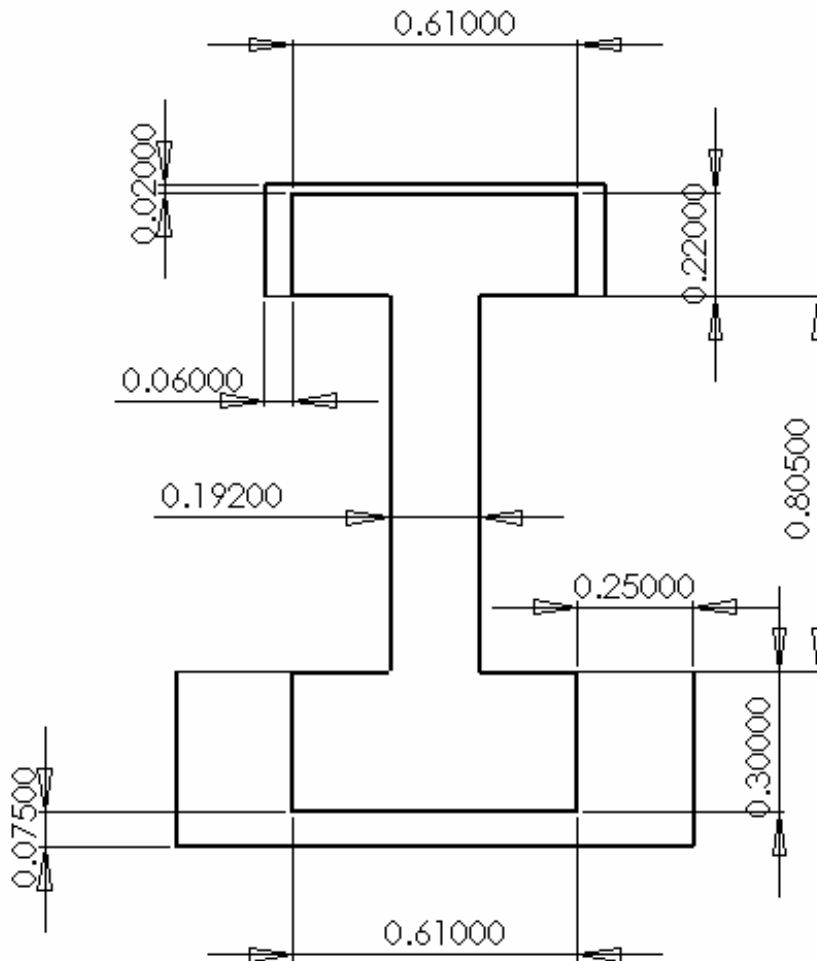


Figure A-0-8. Reference dimension drawing for transformed area method.

To use the transformed area method, it is first necessary to change the epoxy "I" into a different sized piece of steel that results in the same moment of inertia (I_c) of the original sized epoxy "I". This is done by multiplying the width of each piece of the "I" (the web and two flanges) by the ratio n , which is the elastic modulus of the epoxy divided by the

elastic modulus of the aluminum. Since n is unknown (because the modulus of epoxy is being solved for), the ratio n is used symbolically. Therefore, the dimensions of the web of the "I" are now .192*n x .805".

The next step is to find the neutral axis of the new cross-section. The equation for this

axis is given by $y_c = \frac{\sum y_i A_i}{\sum A}$, where A is the area of each piece of the cross-section and y_i is the distance from a reference axis to the centroid of each piece. Summing the areas,

```
>
A:=2*.375*.25+2*.06*.24+.02*.61+.61*.075+.61*.3*n+.192*.805
*n+.61*.22*n;
A := 0.27425 + 0.471760 n
```

Substituting the rest into the equation,

```
>
y[c] := (2*.375*.25*.1875+2*.06*.24*1.3+.02*.61*1.41+.61*.075
*.0375+.61*.3*n*.225+
.192*.805*n*.7775+.61*.22*n*1.29)/A;
y_c :=  $\frac{0.091513875 + 0.3344634000 n}{0.27425 + 0.471760 n}$ 
```

After the neutral axis is found, the moment of inertia (Ic) of the equivalent all aluminum cross-section about this axis can be found. Using the parallel axis theorem,

```
> i [c] := 2*(.25*.375^3/12+.25*.375*(y[c]-
.1875)^2)+2*(.06*.24^3/12+.06*.24*(1.3-y[c])^2)+
(.61*.02^3/12+.02*.61*(1.41-
y[c])^2)+(.61*.075^3/12+.61*.075*(y[c]-.0375)^2)+(.331*.61*
n*.3^3/12+.331*.61*n*.3*(y[c]-
.225)^2)+(.192*.426*n*.805^3/12+.192*.426*n*.805*(.7775-
y[c])^2)
+(.61*.243*n*.22^3/12+.61*.243*.22*n*(1.29-y[c])^2);
```

$$\begin{aligned}
i_c := & 0.002357357604 + 0.18750 \left(\frac{0.091513875 + 0.3344634000 n}{0.27425 + 0.471760 n} - 0.1875 \right)^2 \\
& + 0.0288 \left(1.3 - \frac{0.091513875 + 0.3344634000 n}{0.27425 + 0.471760 n} \right)^2 \\
& + 0.0122 \left(1.41 - \frac{0.091513875 + 0.3344634000 n}{0.27425 + 0.471760 n} \right)^2 \\
& + 0.04575 \left(\frac{0.091513875 + 0.3344634000 n}{0.27425 + 0.471760 n} - 0.0375 \right)^2 + 0.004141462332 n \\
& + 0.060573 n \left(\frac{0.091513875 + 0.3344634000 n}{0.27425 + 0.471760 n} - 0.225 \right)^2 \\
& + 0.065842560 n \left(0.7775 - \frac{0.091513875 + 0.3344634000 n}{0.27425 + 0.471760 n} \right)^2 \\
& + 0.0326106 n \left(1.29 - \frac{0.091513875 + 0.3344634000 n}{0.27425 + 0.471760 n} \right)^2
\end{aligned}$$

Now the equation for deflection of a simply supported beam may be used with the experimentally obtained deflections to solve for the ratio n. This equation is given by

$$\delta = \frac{WL^3}{48EI} + \frac{WL}{4AG}$$

δ = beam deflection

W = applied load (lb)

L = beam length (in)

E = modulus of elasticity (psi)

G = shear modulus (psi)

A = cross sectional area (in²)

I = moment of inertia about centroid of beam (in⁴)

However, the right side must first be multiplied by n to compensate for the material change. Solving for n,

```
>
n:=fsolve(60146=n/(4.12^3/(48*10e6*i[c])+4.12/(4*A*3.77e6)),n);
```

$n := 0.1886636916$

Therefore,

> **E[epoxy] := n * E[Al] ;**

$$E_{epoxy} := 0.1886636916 E_{Al}$$

> **E[epoxy] := n * 10e6 ;**

$$E_{epoxy} := 0.1886636916 \cdot 10^7$$

Appendix F – Magnet Track Relief Analysis

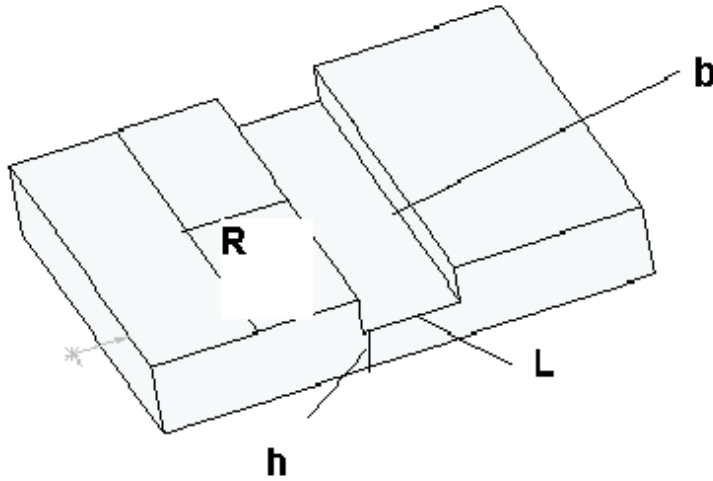
A summary of a wide variety of tests for different brackets and coil make-ups is shown in Table A-2. It is important to remember that these tests were conducted with the slide fixed at its midpoint (i.e., a 3.5” slide) to simulate the bearing stiffness, which is much higher than the structural stiffness. Also, the “Old Configuration” refers to the first design where the rear plate of the slide is flat and the motor hangs roughly 1” off the back of the slide. The “New Configuration” involves the new rear plate and the relieved section at the back of the slide. Four observations from the Table are given below.

- 1.) The new configuration raises both the vertical and horizontal bending natural frequencies while slightly lowering the moving mass of the system. The new configuration also adds stiffness under bending loads.
- 2.) Contrary to original thought, making the gussets “L-shaped” does not significantly raise the natural frequency of the system.
- 3.) Adding a small aluminum piece onto the top flange of the motor in the model slightly raises the vertical natural frequency but has little affect on the other measured values.
- 4.) While making all bracket components 1/8” thick does increase the natural frequency of the system slightly, it is not enough to justify the added weight.

Bracket Description	Moving mass (lb)**	Natural Frequency (Hz)		Deflection Under 100 lb. (in.)
		Horizontal	Vertical	
Old Configuration**				
1/16" walls, 1/8" mounting plate, holes for lightweighting	1.01	727	906	0.0183
1/16" walls, 1/8" mounting plate	1.06	858	1074	0.0142
1/8" walls, 1/8" mounting plate	1.31	910	1075	0.01015
New Configuration				
1/16" walls, 1/8" mounting plate, holes for lightweighting	0.973	956	1010	0.007
1/16" walls, 1/8" mounting plate	1.022	982	1040	0.006
1/16" walls, 1/8" mounting plate, holes for lightweighting, and L-shaped gussetts	0.98	960	1007	0.0068
New Configuration, added aluminum to top motor flange				
1/16" walls, 1/8" mounting plate, holes for lightweighting	0.971	1070	1017	0.007
1/16" walls, 1/8" mounting plate	1.022	1104	1048	0.006
1/16" walls, 1/8" mounting plate, holes for lightweighting, and L-shaped gussetts	0.98	1075	1017	0.0068

Table A-2. Magnet track relied and bracket testing summary.

Appendix G – Flexure Plate Calculations



*Assume max force generated by micro-height adjuster is 340 lb (1500 N)

**Choose steel as material (12" X 8")

***Need total range of 200 μm (7.874 mil)

P= 340 lb For a cantilever beam with end moment
 b= 8 in.
 E= 3.00E+07 psi

L= 2 in.
 h= 0.375 in.

$$y = \frac{ML^2}{2EI}$$

y = deflection (in.)
M = moment (lb-in)
E = modulus of elasticity (psi)
I = moment of inertia (in⁴)
L = beam length (in.)

$$\theta = \frac{ML}{EI}$$

θ = rotation angle at end of beam (rad)

Moment of Inertia I (in ⁴)	Moment arm R (in)	Moment (lb-in)	Defl. at end of "beam" (mil)
0.03515625	3.125	1062.5	2.01
Angle at end of "beam" (rad)	Dist. To Tool Tip (in)	Defl. Due to Offset (mil)	Total Tool Movement (mil)
0.00201	5.00	10.07407407	12.09

Appendix H – Amplifier Configuration Guide

1. In the Elmo Composer program, start a “New Application.”
2. Choose a communication type (RS 232).
3. Select motor type, continuous current, and maximum speed (Linear brushless, 3.18 A, 10.12 m/s, respectively).
4. Specify values for the Magnetic Pitch (Distance of one **electrical** cycle), cycles per meter and multiplication factor (the product of the two being the counts per meter). The numbers used were 30.48 mm, 50,000 cycles/m and 4, respectively (giving 200,000 cts/m, which is 5 μ m resolution).
5. Specify the application current and mechanical limits. These limits may also be set by the UMAC controller.
6. Perform Auto-tune on the amplifiers current loop. It will run through a few iterations and store acceptable gain parameters for its internal current loop.
7. Establish commutation – The amplifier will do this automatically. The process will start with the motor moving forward until it locks onto a magnetic pole. From there, it must have enough travel space to move from the first magnetic pole to the next (this distance is the Magnetic Pitch specified in Step 4, 30.48 mm in this application). If space is limited, swapping the coil wiring could help the motor find a pole quicker. If enough space is available, verify travel in the positive direction and the commutation setup is complete.

8. In the Elmo Composer Smart Terminal, set the Amp/Volt scale factor. This specifies the amount of current that goes out for every input volt. It is optimal to have the maximum input voltage represent the maximum continuous current output. For example, the Cello amplifier has a maximum current of 3 Amps, and the UMAC has a maximum output voltage of 10 V, so the A/V scale factor was set to 0.3 Amps/Volt.

The amplifier is now configured for the current loop mode of operation.

Appendix I – Motion Programs and PMAC Code

Open Loop Testing Program

```
&1

open prog 25
clear

abs

I15=1           //sets sin argument units to radians

I5111 =15000    //sets counter to value * 442 microsecs
p805=0.5

while ( I5111 > 0 )

    I229=500*sin(20*2*3.14157*(15000-I5111)*.000442) //Ix29 is bias for motor x

endwhile

i229=0

close
```

Swept Sine Wave Program (Closed Loop)

```
//Swept sine wave
// *Inputs are p850-p854

&1

close

open prog 25

clear
spline1
abs

I15=1           //sets sin argument units to radians

p850=0          //Desired starting frequency (Hz)
```

```

p851=0.5 //Desired ending frequency (Hz)
p852=30 //Desired sweep time (sec, max=3500)
p853=0.5 //Desired amplitude (mm)

P854=p53 //Sets p854 to the axis position (=p53
//for nanoform, =p81 for ultraform)

p855=(p851-p850)/(p852*2259) //Necessary frequency rate of increase
// (Hz/servo cycle)

I5111=p852*2259 //Sets counter to the equivalent desired
// sweep time (2259 servo cycles/sec)

while (I5111 > 0)

    p856=p852*2259-I5111 //elapsed time (counts)
    p857=p850+(p856)*p855 //sets the frequency
    p858=p853*sin(2*3.14157*p857*p856/2259) //calculates sine value
    Z(p854+p858) //moves axis

endwhile

close

```

Programs for position-based cutting of a tilted flat

The following programs are used to cut a tilted flat based on the position of the spindle and x-axis. The first program (26) runs first, and the second program (27) is triggered in the middle of the first one. Program 26 controls the position of the x and z axes, while Program 27 controls the LAT axis position.

```

//Tiltedflat.pmc
&1
close

open prog 26
clear

```

```

linear
abs

p875=1
p876=1           //number of passes
p877=0
p878=.05        //depth of cut
while (p876>0)
p877=p877-p878
p870=0
z5x-30f5
dly0
p870=1
z(p877) f5
x0 f1
dly0
p870=0
z5
x-30 f5
p876=p876-1
endwhile
p875=0
close

//Tiltedw.pmc
&2
close

open prog 27
clear
spline1
abs

i15=0           //set operation to degrees
p860=2          //sine wave max amplitude at p861
p861=25        //part radius
p862=.5        //tool radius
tm5            //set federate to max
p875=1
p870=0
w0
while (p875=1)
while (p870=0)
w0

```

```

endwhile

while (p870=1)
    p871=360*(((m462+m464)/(i408*32*p44))%1) //spindle position
    p872=(m162+m164)/(i108*32*p41) //x-axis position
    p863=atan((p860/p861)*cos(p871)) //surface angle
    w((p860*p872/p861)*cos(p871)+p862*abs(sin(p863)+cos(p863)-1))
endwhile
endwhile
w0
close

```

Kinematics Routine

Forward kinematics program

```

// Before any execution of the forward-kinematic program, the PMAC will
place
// the present commanded motor positions for each Motor xx in the
coordinate
// system into global variable Pxx. These are floating-point values,
with
// units of counts. The program can then use these variables as the
"inputs"
// to the calculations.
//
// After the execution of the forward-kinematic program, the PMAC will
take
// the values in Q1-Q9 for the coordinated system in the user's
engineering units,
// and copy these into the 9 axis target position registers for the
coordinate system.

// Q3 C axis
// Q6 W axis
// Q7 x axis
// Q9 z axis

I15=0 // Trig calculations in radians

&l open forward
clear

Q6=P2/6400 // LAT position
Q7=P1/809076.8 // x axis position
Q9=P3/809076.8 // z axis position
Q3=P4/1515520 // spindle position

Close

```

Inverse kinematics program

```
// Before any execution of the inverse-kinematic program, the PMAC will
place the present axis target psotiiions for each axis // in the
coordinate system into variables in the range Q1-Q9 for the coordinate
system. These are floating-point values, in // engineering units. The
program can then use these variables as the "inputs" to the
calculations.
```

```
// After any execution of the inverse-kinematic program, the PMAC will
read the values in those variables Pxx (P1-P32) that // correspond to
Motors xx in the coordinate system with axis-definition statements of
#xx->I. These are floating-point // values, and the PMAC expects to
find them in raw units of "counts". PMAC will automatically copy these
values into the // target position registers for these motors, where
they are used for the fine interpolation of these motors.
```

```
&1

#2->I          // Motor 2 assigned to inverse kinematic axis in CS1

I15=0         //trig arguments in degrees

Q90=2         // LAT sine wave maximum amplitude (mm)
Q91=25        // part radius (mm)
Q92=1         // tool radius (mm)

&1 open inverse
clear

if (p870=1)   // controlled by xz motion program, runs LAT only
during pass

    Q93=360*(Q3%1) // spindle position in deg
    Q94=atan((Q90/Q91)*cos(Q93)) // surface angle

    P6=((Q90*Q7/Q91)*cos(Q93)+Q92*abs(sin(Q94)+cos(Q94)-
1))*96*32*6400 // LAT command in "raw" cts
endif

close
```

Program for time-based cutting of a tilted flat

The following is the MATLAB code needed to generate incremental PMAC commands to cut a tilted flat given specified input parameters. The output of the program is commands for the spindle, x, z, and LAT axes. These commands are then pasted into a motion program and used for cutting a tilted flat. Since the motion program itself is entirely too long to be given, only the MATLAB code used to generate the commands is shown (% denotes a comment in MATLAB).

```
% Calculate PMAC motion program Incremental commands for a tilted flat cut.
% This assumes the motion program a starting position of -(part + tool + 1)
% [C,X,W] = LATcut(part,tool,amp,feed,freq,move)
% Input
% part    part radius (mm)
% tool    tool radius (mm)
% amp     sine wave maximum amplitude (mm)
% feed    feed rate (mm/sec)
% freq    sine wave frequency (Hz)
% move    move time for the spindle (msec)
% Output
% C       vector of incremental spindle commands
% X       vector of incremental X axis commands
% W       vector of incremental LAT axis commands
```

```
function[C,X,W] = LATcut_test(part,tool,amp,feed,freq,move)
```

```
if nargin < 5, freq = 5; end
if nargin < 6, move = 10; end
```

```
% determine starting point for x axis
```

```
x_start = -(part + tool + 1);
```

```
% adjust starting point to ensure an even multiple of the step size
```

```
x_grad = feed/1000*move; % mm/move
steps = mod(abs(x_start),x_grad);
```

```

if (steps ~= 0)
    x_start = -(abs(x_start) + (x_grad - steps));
end

x_pos = linspace(x_start,0,(0-x_start)/x_grad + 1);
x_com = diff(x_pos);

% determine spindle commands

pts_per_rev = ((1/freq)*1000)/move;
c_grad = 1/pts_per_rev;

c_pos = linspace(0,length(x_com)*c_grad,length(x_com) + 1);
c_com = ones(length(x_com),1)*c_grad;

% determine LAT commands

theta = c_pos*2*pi;
LAT_nom = amp*cos(theta);

idx = min(find(abs(x_pos) <= part))
scalefactor = ones(length(x_pos),1);
scalefactor(idx:end) = abs(x_pos(idx:end))/part*amp;

surface_angle = atan(2*(amp/(2*part))*LAT_nom);
toolcomp = abs(tool.*sin(surface_angle).*tan(surface_angle)-
tool+tool.*cos(surface_angle));
LAT_pos = LAT_nom.*scalefactor - toolcomp;
LAT_com = diff(LAT_pos);

% Plot the tool path/position in proper orientation and rotated flat
% x = x_pos.*cos(theta);
% y = x_pos.*sin(theta);
% z = LAT_pos;
%
% x = x(idx:end);
% y = y(idx:end);
% z = z(idx:end);
%
% D = [x y z];
%
% Const = ones(size(x));
%
% Coef = [x y Const]\z;
% xcoef = Coef(1);

```

```
% ycoef = Coef(2);
% ccoef = Coef(3);
% z1 = xcoef*x + ycoef*y + ccoef;
% z0 = z - z1;
% F = [x y z0];
%
% surf3(D);
% figure;
% surf3(F);

% Return the incremental commands in vector form

C=c_com;
X=x_com;
W=LAT_com;
```

Appendix J – Thermistor Manufacturer Specs



MATERIAL TYPE: GE9.7A

AVAILABLE PRODUCTS: GE, MELF

Data for material type : GE9.7A

Temp Range (°C)	Ratio	Beta
0 to 50	9.21	3920
0 to 70	13.95	3939
25 to 50	2.80	3962
25 to 85	9.42	3992
25 to 100	14.90	4007
25 to 125	29.77	4023
37.8 to 104.4	9.85	4023

To calculate Rt/R25 at temperatures other than those listed in the table, use the following equation:

$$Rt/R25 = \exp\{A + B/T + C/T^2 + D/T^3\}$$

where T = temperature in K

where K = °C + 273.15

Temp Range (°C)	A	B	C	D
-50 to 0	-1.6165371 x 10 ⁰¹	5.9362293 x 10 ⁰⁹	-4.0817384 x 10 ⁰⁵	2.2340382 x 10 ⁰⁷
0 to 50	-1.5702076 x 10 ⁰¹	5.7388897 x 10 ⁰⁹	-4.0470744 x 10 ⁰⁵	2.6675244 x 10 ⁰⁷
50 to 100	-1.5663130 x 10 ⁰¹	5.8288379 x 10 ⁰⁹	-4.6657347 x 10 ⁰⁵	3.5960053 x 10 ⁰⁷
100 to 150	-1.4266732 x 10 ⁰¹	4.6187186 x 10 ⁰⁹	-1.4613199 x 10 ⁰⁵	1.3079043 x 10 ⁰⁷
150 to 200	-1.4550747 x 10 ⁰¹	4.9366426 x 10 ⁰⁹	-2.6255040 x 10 ⁰⁵	2.6087099 x 10 ⁰⁷
200 to 250	-1.4179190 x 10 ⁰¹	4.5332228 x 10 ⁰⁹	-1.3010052 x 10 ⁰⁵	1.4375374 x 10 ⁰⁷

To calculate the actual thermistor temperature as a function of the thermistor resistance, use the following equation:

$$1/T = a + b(\ln Rt/R25) + c(\ln Rt/R25)^2 + d(\ln Rt/R25)^3$$

Rt/R25 range	a	b	c	d
70.12 to 3.296	3.3551634 x 10 ⁻⁰³	2.5279858 x 10 ⁻⁰⁴	3.1357674 x 10 ⁻⁰⁶	-6.3869192 x 10 ⁻⁰⁸
3.296 to 0.3577	3.3540171 x 10 ⁻⁰³	2.5481996 x 10 ⁻⁰⁴	2.2498019 x 10 ⁻⁰⁶	-7.3403319 x 10 ⁻⁰⁸
0.3577 to 0.06712	3.3553474 x 10 ⁻⁰³	2.5572896 x 10 ⁻⁰⁴	1.8559626 x 10 ⁻⁰⁶	-9.0217663 x 10 ⁻⁰⁸
0.06712 to 0.01820	3.3414054 x 10 ⁻⁰³	2.4597295 x 10 ⁻⁰⁴	2.8798952 x 10 ⁻⁰⁷	-4.1229589 x 10 ⁻⁰⁸
0.01820 to 0.00645	3.3454862 x 10 ⁻⁰³	2.4717648 x 10 ⁻⁰⁴	1.9792859 x 10 ⁻⁰⁷	-7.5230688 x 10 ⁻⁰⁸
0.006450 to 0.002770	3.3292757 x 10 ⁻⁰³	2.4151501 x 10 ⁻⁰⁴	-1.2953699 x 10 ⁻⁰⁷	-4.3947028 x 10 ⁻⁰⁸

†The deviation resulting from the tolerance on the material constant, Beta. The deviation must be added to the resistance tolerance of the part as specified at 25°C.

Temperature (°C)	Rt/R25 nominal	Temp Coef (%/°C)	β Deviation † (±%)
-50	70.120000	7.28	8.9021801
-45	49.070000	7.01	8.1762247
-40	34.790000	6.75	7.4139024
-35	24.980000	6.51	6.6722521
-30	18.150000	6.28	5.9519946
-25	13.290000	6.07	5.2515254
-20	9.894000	5.86	4.5699908
-15	7.415000	5.67	3.9062679
-10	5.610000	5.49	3.2597878
5	4.282000	5.32	2.6297022
0	3.296000	5.16	2.0152938
5	2.557000	4.99	1.5746264
10	2.000000	4.84	1.1599916
15	1.576000	4.69	0.7519946
20	1.251000	4.55	0.3676955
25	1.000000	4.42	0
30	0.804500	4.29	0.3520485
35	0.651900	4.17	0.689336
40	0.590400	4.05	1.109884
45	0.494400	3.94	1.3226656
50	0.397700	3.81	1.6205602
55	0.296500	3.70	1.9930747
60	0.247000	3.60	2.227961
65	0.206800	3.51	2.5069246
70	0.173900	3.42	2.7688805
75	0.146900	3.33	3.0160591
80	0.124600	3.25	3.250412
85	0.106100	3.17	3.4768896
90	0.090800	3.09	3.6787806
95	0.077900	3.02	3.874746
100	0.067120	2.95	4.0599929
105	0.059000	2.87	4.1527077
110	0.050950	2.80	4.2475295
115	0.043850	2.73	4.3437222
120	0.038920	2.67	4.4411935
125	0.033990	2.60	4.5398341
130	0.029540	2.54	4.6395467
135	0.026080	2.48	4.7402407
140	0.023080	2.42	4.8418906
145	0.020480	2.36	4.9442364
150	0.018200	2.31	5.0472829
155	0.016240	2.26	5.1511996
160	0.014520	2.21	5.2560204
165	0.013020	2.16	5.3605828
170	0.011700	2.11	5.4660285
175	0.010540	2.07	5.5718024
180	0.009510	2.03	5.6781153
185	0.008610	1.98	5.7847917
190	0.007800	1.94	5.8915928
195	0.007090	1.90	5.9989934
200	0.006450	1.87	6.1069991
205	0.005880	1.83	6.2134539
210	0.005370	1.79	6.3210402
215	0.004920	1.75	6.4287182
220	0.004508	1.72	6.5364565
225	0.004140	1.69	6.6442259
230	0.003808	1.65	6.7519966
235	0.003509	1.62	6.8597442
240	0.003238	1.59	6.9674432
245	0.002993	1.56	7.0750705
250	0.002770	1.53	7.1826942

Appendix K – Motor Temperature Calculations

The following calculations were used to estimate the amount of heat generated by the linear motor in the LAT system during 2 mm operation at 20 Hz.

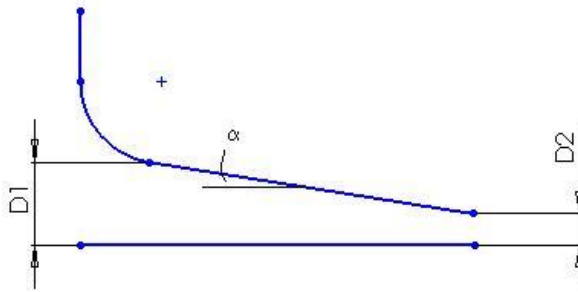
$$\begin{aligned} F &= mA\omega^2 \\ &= (.65kg)(.002m)(2 * \pi * 20Hz) \\ &= 20.5 N \end{aligned}$$

The maximum force needed by the motor is 20.5 N. For a motor constant of 8.9 N/A, this translates into 2.3 A of current. The total coil resistance as given by the manufacturer's specs is 10.91 Ohms. The equation for power (in terms of RMS current and Resistance) is:

$$\begin{aligned} P &= I_{RMS}^2 R \\ &= (.707 * 2.3A)^2 * 10.91\Omega \\ &= 28.8W \end{aligned}$$

The power generated by the motor is 28.8 W. Per the motor specs, the motor heats 1.6 degrees for every Watt of power. This indicates a temperature increase of 46 ° C, which will keep it well below the critical temperature of 125 ° C.

Appendix L – Damping Force Calculations



$$\frac{F}{u} = \frac{2\mu}{\alpha} \left[3 \left(\frac{d_1 - d_2}{d_1 + d_2} \right) - 2 \log \frac{d_1}{d_2} \right]$$

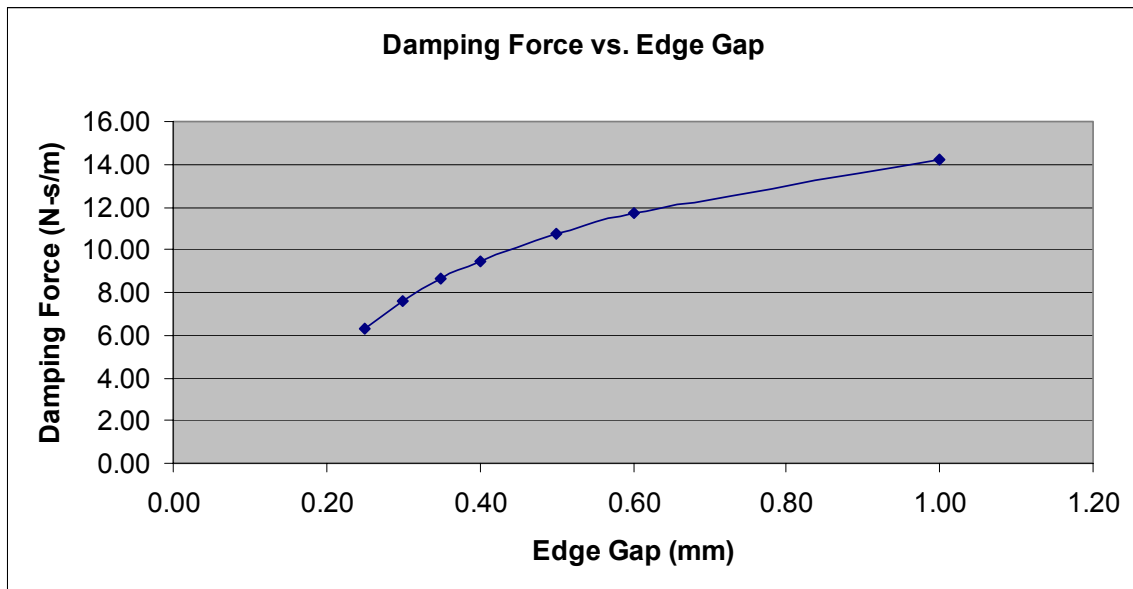
$\mu = \text{viscosity (Pa-s)}$

$d_1 = \text{gap at center (m)}$

$d_2 = \text{gap at edge (m)}$

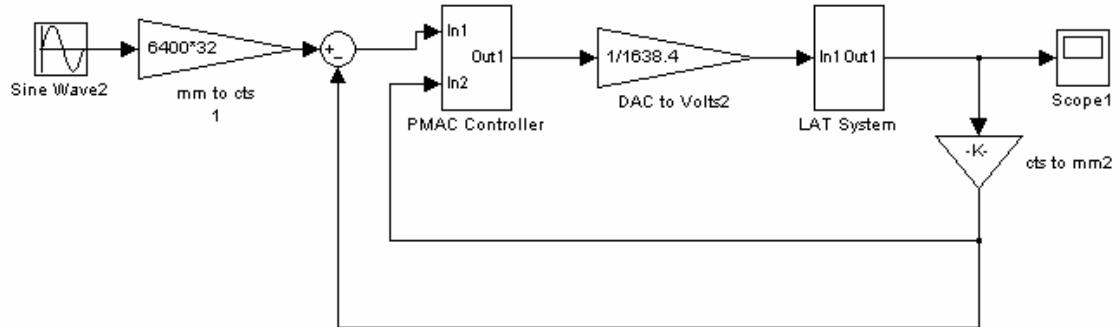
$\alpha = \text{angle between surfaces (rad)}$

visc	Pa-s	2.5	2.5	2.5	2.5	2.5	2.5	2.5
d2	m	1.75E-04	1.75E-04	1.75E-04	1.75E-04	1.75E-04	1.75E-04	1.75E-04
d1	m	2.50E-04	3.00E-04	3.50E-04	4.00E-04	5.00E-04	6.00E-04	1.00E-03
R	m	1.75E-03	1.75E-03	1.75E-03	1.75E-03	1.75E-03	1.75E-03	1.75E-03
x	m	0.0005123	0.000661438	0.000782624	0.000887412	0.001066536	0.001219631	0.001699265
alpha	rad	0.146385	0.188982237	0.223606798	0.253546276	0.3047247	0.348466026	0.485504156
T/U	N-s/m	-6.28E+00	-7.63E+00	-8.64E+00	-9.45E+00	-1.08E+01	-1.18E+01	-1.42E+01

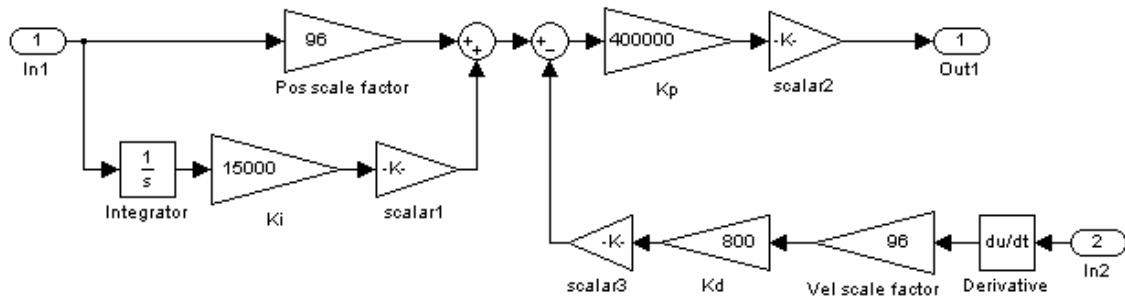


Appendix M – Simulink Model of PMAC Controller

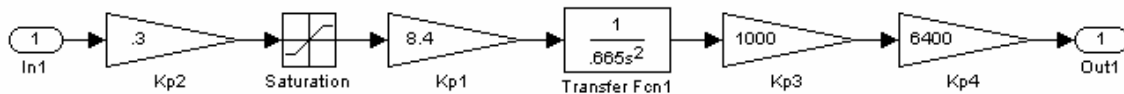
Entire system from input to output:



PMAC Controller subsystem:



LAT Subsystem (undamped):



Appendix N – Tool Radius Compensation

```
> a:=2;
d:=25.4;
r:=1;
w1:=a*cos(theta);
```

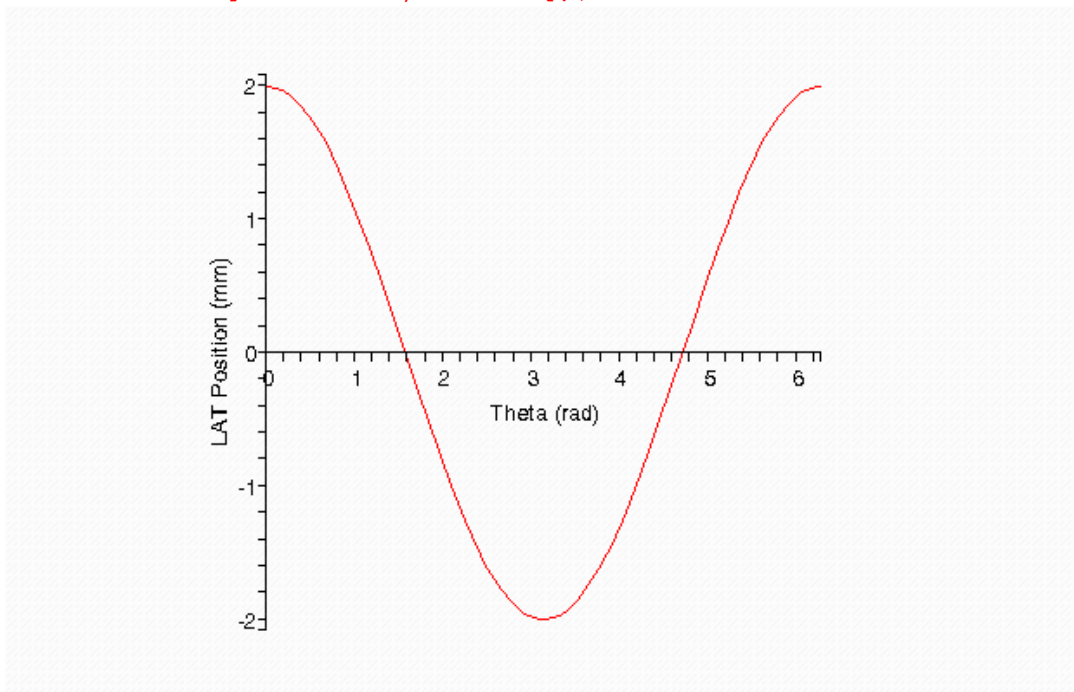
```
a := 2
```

```
d := 25.4
```

```
r := 1
```

```
w1 := 2 cos(θ)
```

```
> plot(w1, theta=0..2*Pi, labels=["Theta (rad)","LAT Position (mm)"],
labeldirections=[horizontal,vertical]);
```



```
> g:=arctan(2*(a/d)*cos(theta));
delta:=abs(r*sin(g)*tan(g)-r+r*cos(g));
g := arctan(0.1574803150 cos(θ))
```

$$\delta := \left| \frac{0.02480004961 \cos^2(\theta)}{\sqrt{1 + 0.02480004961 \cos^2(\theta)}} - 1 + \frac{1}{\sqrt{1 + 0.02480004961 \cos^2(\theta)}} \right|$$

```
> plot(delta,theta=0..2*Pi, labels=["Theta (rad)","Tool Radius
Compensation (mm)"],labeldirections=[horizontal,vertical]);
```

